Efficiency Measurements of a Single Stage Turbine in a Short Duration Facility

by

Jason J. Jacobs

B.S. Aeronautical & Astronautical Engineering
Purdue University, 1996

Submitted to the Department of Aeronautics and Astronautics
in partial fulfillment of the requirements for the degree of

Master of Science in Aeronautics and Astronautics

at the

MASSACHUSETTS INSTITUTE OF TECHNOLOGY

June 1998

Author .....
Department of Aeronautics and Astronautics
20 May 1998

Certified by .....
Dr. Gerald R. Guenette
Principal Research Engineer
Department of Aeronautics and Astronautics, Gas Turbine Laboratory
Thesis Supervisor

Accepted by .....
Jaime Peraire
Associate Professor
Chairman, Department Graduate Committee

Efficiency Measurements of a Single Stage Turbine in a Short Duration Facility

by

Jason J. Jacobs

Submitted to the Department of Aeronautics and Astronautics
on 20 May 1998, in partial fulfillment of the
requirements for the degree of
Master of Science in Aeronautics and Astronautics

Abstract

This document focuses on the MIT Blowdown Turbine short duration test facility and its use in experimentally measuring the adiabatic efficiency of a fully-rotating scaled turbine stage. Efficiency is measured independently by two separate approaches differing in their calculation of actual turbine work. The aerodynamic approach calculates turbine work from upstream and downstream total temperature and pressure and the mechanical approach, from turbine torque, speed, and mass flow.

Absolute and relative measurement uncertainties are estimated for each approach to determine by which method adiabatic efficiency may be measured most accurately and most repeatably in the short duration test facility. Efficiency predictions assuming ideal and calorically perfect gas behavior are compared to real gas efficiency predictions to judge the significance of real gas effects and assess the validity of these assumptions in this situation. Required transient corrections to efficiency accounting for heat transfer, rotor acceleration, tunnel mass storage, and other effects are explored. Turbine off-design performance is characterized by comparing efficiency predictions at off-design operating conditions. Finally, adiabatic efficiency is empirically estimated using well known analyses allowing estimation of efficiency measurement biases.

Thesis Supervisor: Dr. Gerald R. Guenette
Title: Principal Research Engineer
Department of Aeronautics and Astronautics, Gas Turbine Laboratory

Acknowledgments

I would like to take this opportunity to thank the many people who have contributed to my success at MIT.

First I would like to thank Professor Alan H. Epstein for advising my MIT academic career. Great thanks to Professor Edward M. Greitzer and Dr. Choon S. Tan who assisted in my search as I struggled to find funding. Once I did find funding in the Blowdown Turbine, Dr. Gerald R. Guenette became largely responsible for the success of my research work as he contributed to nearly every aspect of it.

Special thanks go to my fellow research students in the Blowdown Turbine, Rory Keogh, Yi Cai, Leo Grepin, and Chris Spadaccini, who were always willing to lend encouragement and assistance as necessary.

I would like to thank James Letendre for tightening and loosening all of the bolts. Thanks to Mariano Hellwig for repairing the tiny little wires even as I continued to break them. Thanks to Viktor Dubrowski who was always ready to work overtime to finish the job. And thanks to Tom Ryan and Bill Ames for their invaluable assistance.

My Master's degree at MIT was made possible by funding from ABB, Inc. I would like to thank all the people at ABB who were involved in bringing this research project to the Gas Turbine Lab.

This degree fulfills a goal set long ago under the influence of Mr. Gary Fancher. As a long time friend, Mr. Fancher has taken an active role in my academic preparation. I sincerely appreciate the direction that he has provided.

Finally, I am forever indebted to my wife, Karalyn, who has put on hold everything so that I might have the opportunity to earn this degree. Without her love and support, it would not have been possible. And I would like to thank the rest of my family whose encouragement has brought me thus far.

Contents

List of Figures

List of Tables

Chapter 1

Introduction

1.1 Motivation

The gas turbine engine has seen its performance and efficiency increase drastically since its initial development in the early 1930s. Countless technological advances have contributed to this trend, but many can be traced to improved turbine designs. Responsible for these improvements is a fundamentally better understanding of the fluid mechanic and thermodynamic aspects of turbine flow. In keeping with this tradition, knowledge of these key areas must continue to advance. The exponential growth of computational power in recent years is lending new insight into these subjects, however, experimental data for calibration and verification is still very much in need. But, with large turbine steady-state rig tests costing millions of dollars, experimental characterization of new turbine designs is dependant upon adequate alternatives.

In recent years, researchers at the Gas Turbine Lab at MIT have worked to develop a transient experimental facility which will rigorously simulate the aerodynamic and heat transfer performance of a fully rotating scaled turbine stage and allow highly accurate and detailed flow measurements, all at relatively very low cost. This facility, known as the Blowdown Turbine, and its use in experimentally determining adiabatic efficiency of a scaled turbine stage are the focus of this work.

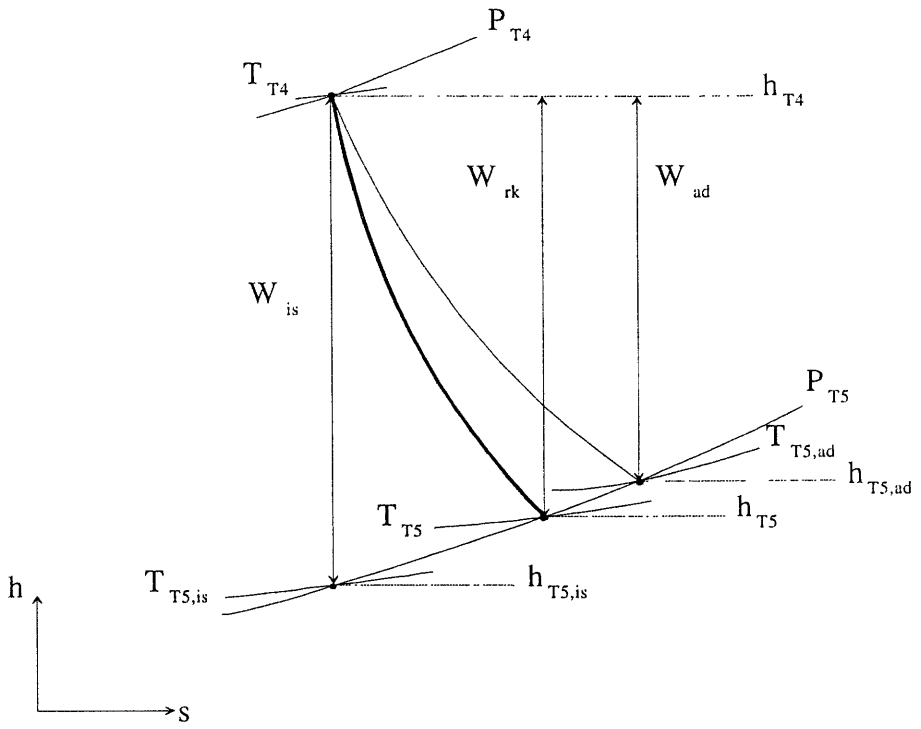

Figure 1-1: Enthalpy-Entropy Diagram Showing Turbine Expansion Processes

1.2 Objectives and Approach

Figure 1-1 shows turbine expansion processes on an enthalpy-entropy, or h-s diagram. The work extracted by the turbine during adiabatic operation is labeled W_{ad}. The ideal, or isentropic work, is labeled W_{is}. Turbine adiabatic efficiency is defined as the ratio of these quantities, each expressed as a change in total enthalpy:

$$\eta_{ad} = \frac{W_{ad}}{W_{is}} \tag{1.1}$$

$$W_{ad} = h_{T4} - h_{T5,ad} \tag{1.2}$$

$$W_{is} = h_{T4} - h_{T5,is} \tag{1.3}$$

Subscripts four and five represent upstream and downstream quantities respectively. The primary objective of this work is to determine this quantity with uncertainty less than 0.50%. This is optimistic, even from steady-state data. Two approaches are taken to arrive at this goal and they differ in their calculation of actual turbine work. The first, or aerodynamic approach, determines actual turbine work from upstream and downstream temperature and pressure measurements. The second, or mechanical approach, utilizes turbine torque, speed, and mass flow for actual turbine work calculation. Other important objectives of this study are to determine by which method turbine adiabatic efficiency may be measured most accurately and most repeatably in the short duration test facility, and, quantify efficiency measurement uncertainties in each approach.

With knowledge of total and static temperature and pressure upstream and downstream, actual turbine adiabatic work may be calculated directly[1] as in Equation 1.2 using real gas property tables; ideal work is found similarly. To assess the significance of real gas effects, simplified gas models may then be employed for work evaluation. Assuming the flow through the turbine to be ideal, work may be expressed only in total temperature and pressure ratio and specific heat. Following an expression derived by Shapiro, Equations 1.2 and 1.3 become [1]:

$$W_{ad,ig} = C_{P4} \cdot T_{T4} - C_{P5} \cdot T_{T5} - (C_{P4} - C_{P5}) \cdot \frac{T_4 + T_5}{2} \tag{1.4}$$

$$W_{is,ig} = C_{P4} \cdot T_{T4} - C_{P5} \cdot T_{T4} \cdot \pi_t^{\frac{R}{\bar{C}_P}} - (C_{P4} - C_{P5,is}) \cdot \frac{T_4 + T_{5,is}}{2} \tag{1.5}$$

where

$$\bar{C}_P = \frac{C_{P4} + C_{P5}}{2} \tag{1.6}$$

Further assuming calorically perfect gas behavior, variation in specific heat is neglected and adiabatic and isentropic work assume a familiar form:

[1]This involves a heat transfer correction due to non-adiabatic effects discussed in Section 4.5.

$$W_{ad,cpg} = \bar{C}_P \cdot (T_{T4} - T_{T5}) \tag{1.7}$$

$$W_{is,cpg} = \bar{C}_P \cdot \left(T_{T4} - T_{T4} \cdot \pi_t^{\frac{R}{\bar{C}_P}} \right) \tag{1.8}$$

Another focus of this work will be to explore these assumptions and their validity in this situation by comparing efficiency calculations assuming ideal and calorically perfect gas behavior with real gas efficiency calculations.

Mechanically, turbine work may be calculated from measurements of turbine torque, speed, and mass flow as follows[2]:

$$W_{ad,brk} = \frac{\mathcal{T} \cdot \omega}{\dot{m}_t} \tag{1.9}$$

Efficiency may then be calculated using real gas ideal work, Equation 1.3, or by assuming ideal or calorically perfect gas behavior, Equation 1.5 or 1.8. These calculations will also allow assessment of the validity of the ideal and calorically perfect gas assumptions.

Another significant objective of this study is to assess the effect of tip clearance on turbine adiabatic efficiency. Larger tip clearance leads to additional secondary flow, well known to degrade turbomachinery performance and efficiency. This relationship will be studied by duplicating experiments for two different tip clearances. Providing adequate efficiency measurement resolution, the effect of increased tip clearance on turbine adiabatic efficiency will be quantified.

In short, turbine experimental data will be acquired from the Blowdown Turbine short duration test facility. Estimates of flow field measurement uncertainties and resulting efficiency measurement uncertainties will be presented. Turbine adiabatic efficiency will be calculated, both from an aerodynamic and mechanical approach with the ultimate goal of efficiency uncertainty less than 0.50%. Necessary corrections accounting for heat transfer

[2]This involves a number of corrections accounting for rotor acceleration, tunnel mass storage, and heat transfer effects discussed in Sections 5.3.2, 5.3.3, and 5.4.

effects and transient test conditions will be explored. The significance of real gas effects will be determined by comparing efficiency predictions assuming ideal and calorically perfect gas behavior to real gas calculations. Finally, the effect of increased secondary flow on turbine adiabatic efficiency, specifically due to larger tip clearance, will be quantified by comparing efficiency predictions from duplicate experiments at different tip clearances.

1.3 Chapter Summary and Thesis Outline

This opening chapter has introduced the need for a reliable, low cost experimental facility for turbine characterization. It has also outlined the objectives and approach taken during this study intended to experimentally determine turbine adiabatic efficiency with uncertainty less than 0.50%. The remainder of this work will be organized as follows.

Chapter 2 is devoted to the Blowdown Turbine experimental facility. Chapter 3 will outline test operating conditions and present an analysis of the experimental data. Chapters 4 and 5 explore adiabatic efficiency measurement from an aerodynamic and mechanical approach respectively. Chapter 6 characterizes turbine off-design performance in terms of adiabatic efficiency. Efficiency is also estimated empirically and compared to aerodynamic and mechanical measurements. Finally, Chapter 7 presents the conclusions of this study and discusses future work planned in the Blowdown Turbine.

Chapter 2

Blowdown Turbine Experimental Facility

2.1 Introduction

The MIT Blowdown Turbine experimental facility is a short duration blowdown-driven wind tunnel supporting a fully rotating turbine stage. Originally designed around a 0.75 *scale* Rolls-Royce experimental high pressure turbine stage, it now houses a 0.25 *scale* ABB GT24 first low pressure turbine stage. The facility has the capability of rigorously simulating the aerodynamic and heat transfer performance of the turbine stage during an approximate 500 ms test window. The idea behind the short duration experiment lies in the realization that the time scales of the flow phenomena of interest are very small; they can be on the order of blade passing frequency (inverse). Therefore, quasi-steady-state measurements can be made in a fraction of a second capturing several hundred flow time scales while consuming a fraction of the energy required for the same measurements in a steady-state environment.

This chapter describes the Blowdown Turbine experimental facility and its operation. A description of the test rig configuration and internal flow path is followed by typical preparations required for a blowdown experiment. Scaling of the experimental operating point to achieve full scale turbine similarity is presented. Flow measurement capabilities

and instrumentation are then described. Finally, data acquisition equipment is discussed.

2.2 Facility Configuration

The Blowdown Turbine experimental facility, shown in Figure 2-1, consists of four primary components: the supply tank, the fast-acting valve, the test section, and the dump tank. What follows is brief description of these facility components. A detailed discussion on the design of the facility can be found in Reference [2].

The supply tank is a large cylindrical tank rated to 150 $psia$. The supply tank is wrapped in a metal jacket which circulates heat transfer oil around the tank exterior to heat the tank to the desired test temperature. A stirring fan is mounted in the rear of the tank to ensure a uniform test gas mixture.

The supply tank is separated from the test section by a fast-acting, axially traversing, plug valve. This valve is designed to fully open and introduce disturbance-free flow into the test section in approximately 50 ms. When closed, the valve seals the supply tank pressure, up to 7 atm, from the test section, and when open, forms a smooth annular flow path contraction. The valve dynamics are controlled by the expansion of supply tank gas into damping chambers around the valve. This process produces a pressure differential across the valve whose magnitude and direction depend on the valve position. In its closed position the valve is accelerated open. As it nears its fully open position the valve is decelerated to rest. The initial valve movement is provided by a compressed argon lecture bottle.

The test section, shown in Figures 2-2 and 2-3, houses the forward frame, the rotor assembly, and the eddy current brake torque meter (not shown). The forward frame mates to the fast-acting valve upstream and holds the stationary nozzle guide vanes downstream. The forward frame is followed by the rotor assembly which consists of the rotor discs and blades and a large cylindrical drum (not shown). This drum acts as a conductor and inserts into the eddy current brake. When spinning in the magnetic field produced by the brake magnets, a current is induced in the drum. This current, through resistive heating of the drum, dissipates the power produced by the turbine. Additionally, this current, in

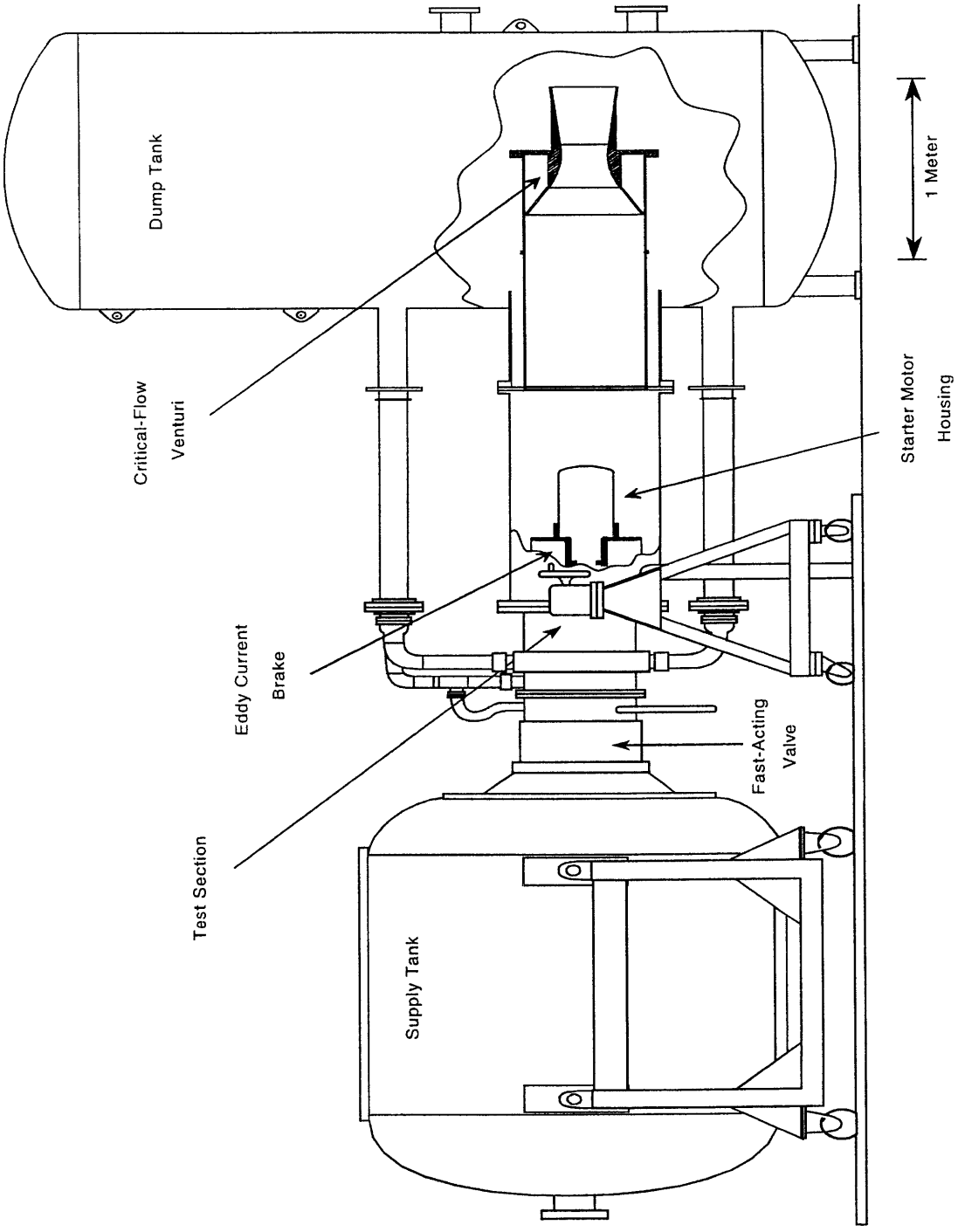

Figure 2-1: Blowdown Turbine Experimental Facility

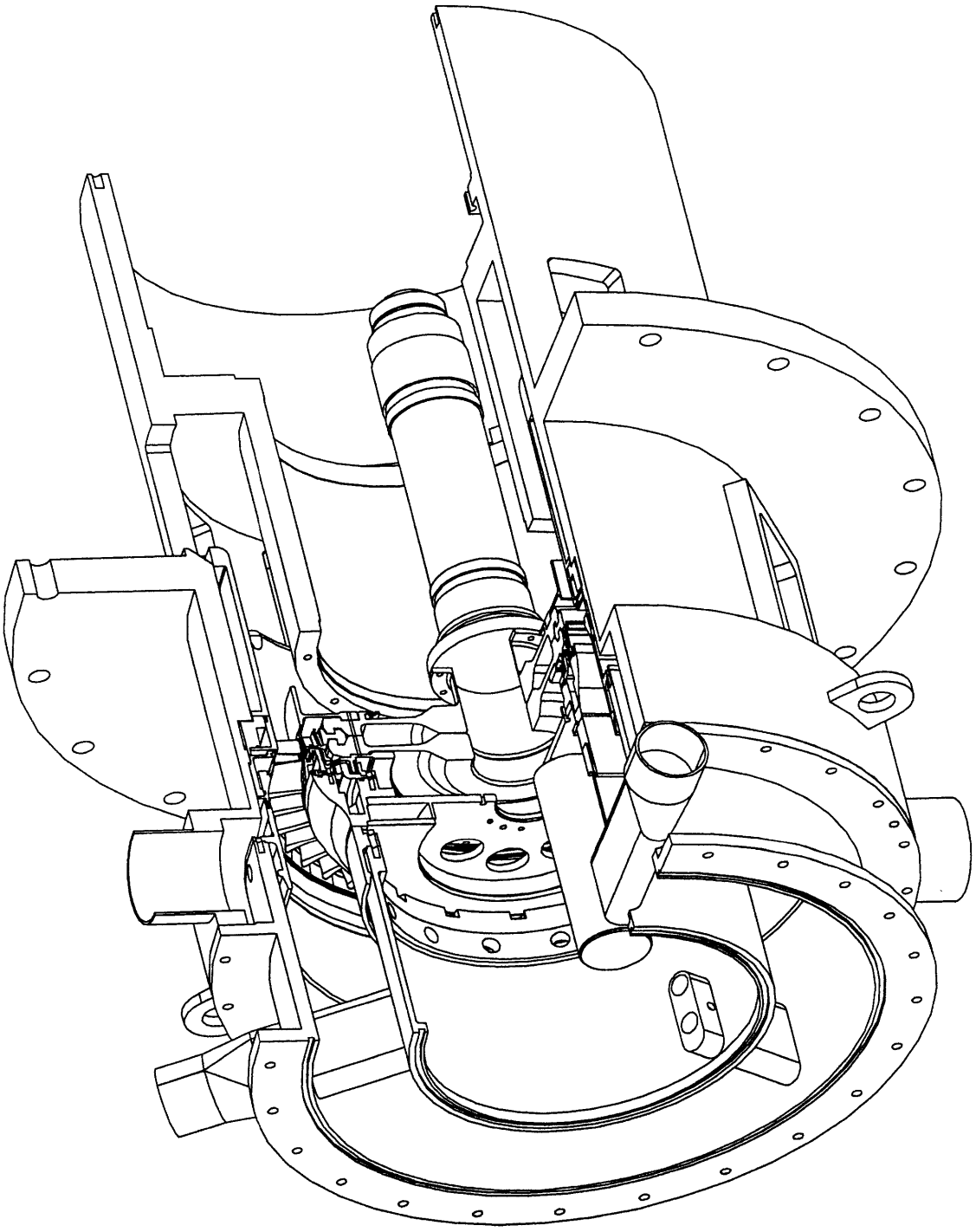

Figure 2-2: Test Section Cutaway

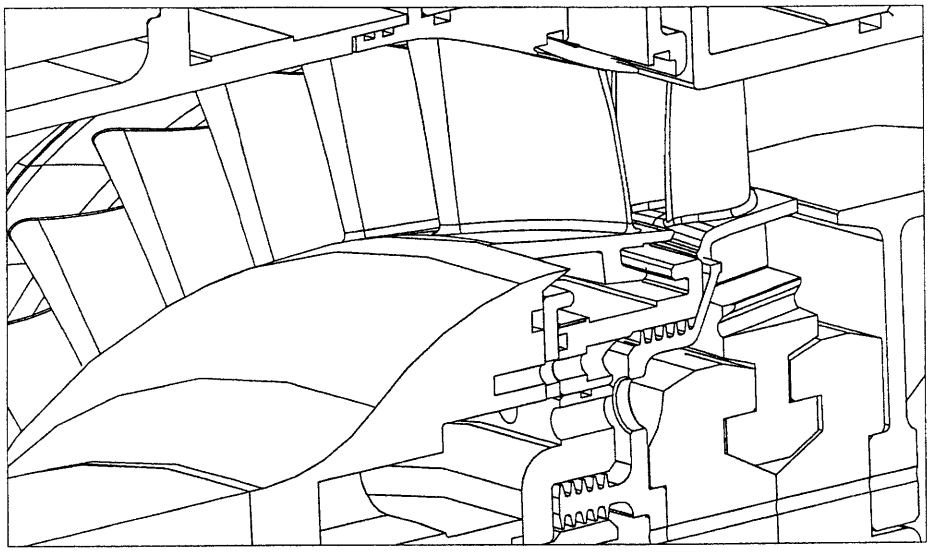

Figure 2-3: Turbine Blades and Vanes

the presence of the magnetic field, opposes the rotation of the drum providing a braking torque. This torque can be adjusted via brake excitation allowing control of turbine speed. By mounting the brake assembly on bearings and reacting the braking torque through load cells, a measurement of turbine torque is available.

Figure 2-4 shows a cross-sectional view of the test section flow path. Upstream of the stage, a boundary layer bleed passage provides clean flow into the turbine. Downstream of the rotor, the flow is exhausted into the dump tank through the downstream throttle plate area. During a portion of the experiment this area is choked, thus, it is adjusted according to test conditions to achieve the desired pressure ratio across the turbine stage. Also shown in Figure 2-4 are upstream and downstream total temperature and pressure measurement locations. Instrumentation is discussed in Section 2.5.

A recent modification to the facility was the addition of the critical-flow venturi, shown in Figure 2-1, to measure facility mass flow. The venturi, which is simply a smooth, geometrically well defined nozzle, was designed and built by Flow Systems, Inc. of Boulder Colorado and calibrated by Colorado EESI traceable to the National Institute for Standards and Technology. During the venturi design process, a model of the facility dynamics

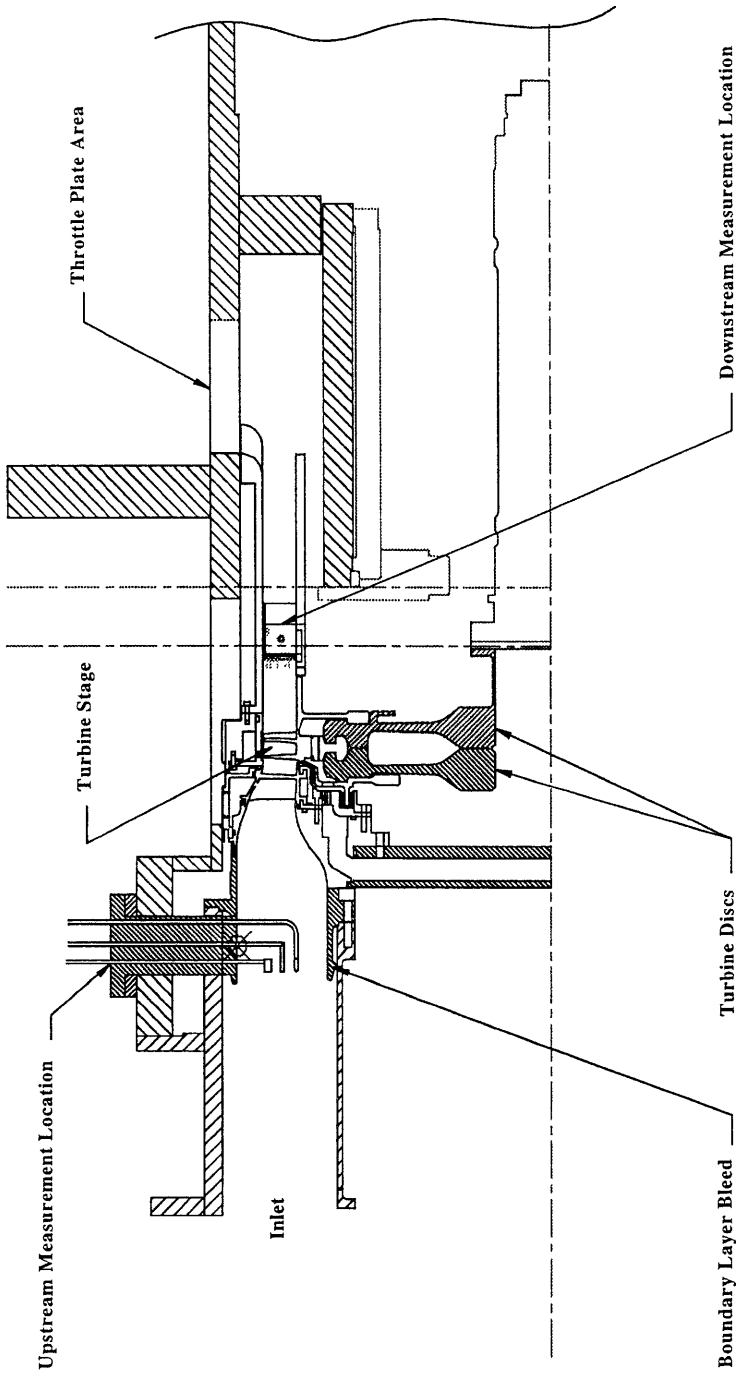

Figure 2-4: Test Section Flow Path

was used to assess the effect of an additional choke point downstream of the throttle plate. This model predicted an additional volume was necessary between the throttle exhaust and the venturi to avoid interference and extend test time. This is achieved by separating the test section and dump tank by a 66 in long diffuser. A full discussion on the design and installation of the critical-flow venturi including an analysis of its operation can be found in Reference [3].

2.3 Run-Time Preparations

Preparations for a blowdown experiment begin by determining the desired operating point to achieve full-scale turbine similarity. This analysis is presented in the next section, so here it is accepted that this operating point consists of the upstream total temperature and pressure, or initial supply tank temperature and pressure, test gas composition, mechanical speed, throttle plate area, and brake excitation. The experiment then proceeds as follows.

The entire facility is evacuated and the supply tank is heated to the desired upstream temperature. After thermal equilibrium is reached, the fast-acting valve is sealed and the supply tank is filled to the desired upstream pressure. At this postfill state, all differential pressure transducers are calibrated by exposing their back face first to vacuum then to atmosphere. This provides a scale for each transducer which is necessary in reducing test data. The brake excitation is then set and the rotor, still in vacuum, is accelerated to just above the desired mechanical speed by the starter motor. When the starter motor is powered off, the rotor slowly begins to decelerate due to bearing friction. When the decelerating rotor reaches the desired mechanical speed, triggering occurs causing the valve to open and the data acquisition systems to begin taking data. The window of useful data typically spans $300 - 800$ ms. The initial 300 ms is spent opening the valve and establishing a steady flow through the test section. Depending on test conditions, the non-dimensional similarity parameters, discussed in the next section, may remain constant through 800 ms. Once the rotor has stopped, the calibration sequence described above is repeated. This allows assessment of transducer drift during the experiment. Further discussions on calibration

procedures and data acquisition can be found in Sections 2.5.5 and 2.6 respectively.

2.4 Scaling of Operating Point

Validity of scaled wind tunnel experiments depends on similarity between the experiment and the flow being simulated. When cast in dimensionless form, the governing equations of momentum and energy transfer produce non-dimensional parameters which determine the flow field. Thus, similarity between experiment and reality requires only that these non-dimensional parameters be reproduced. It is shown that for a turbine stage, corrected mass flow and total temperature ratio depend only on four non-dimensional parameters [2]:

$$\left[\frac{\dot{m}_t\sqrt{R\,T_{T4}}}{P_{T4}\,L_{ref}^2}, \tau_t\right] = f\left(\pi_t, \frac{N\,L_{ref}}{\sqrt{R\,T_{T4}}}, \frac{\dot{m}_t}{\mu\,L_{ref}}, \gamma\right) \tag{2.1}$$

total pressure ratio, corrected speed, Reynolds number, and specific heat ratio. These are the parameters which imply similarity for the Blowdown Turbine experiments. It is left to show how Blowdown Turbine operating conditions are set to match these parameters. As mentioned in the previous section, an operating point consists of the upstream total temperature and pressure, test gas composition, mechanical speed, throttle plate area, and brake excitation. For all experiments described here, the test gas is pure CO_2.

First, the initial upstream total temperature and pressure, or supply tank temperature and pressure, are set to simultaneously match Reynolds number and specific heat ratio. As presented in Equation 2.1, Reynolds number may be written in terms of mass flow:

$$R_e = \frac{\dot{m}_t}{\mu\,L_{ref}} \tag{2.2}$$

Corrected flow, a known quantity equal to the stage design corrected flow, may also be expressed in terms of mass flow:

$$W_c = \frac{\dot{m}_t\sqrt{R\,T_{T4}}}{P_{T4}\,L_{ref}^2} \tag{2.3}$$

Combining these equations gives:

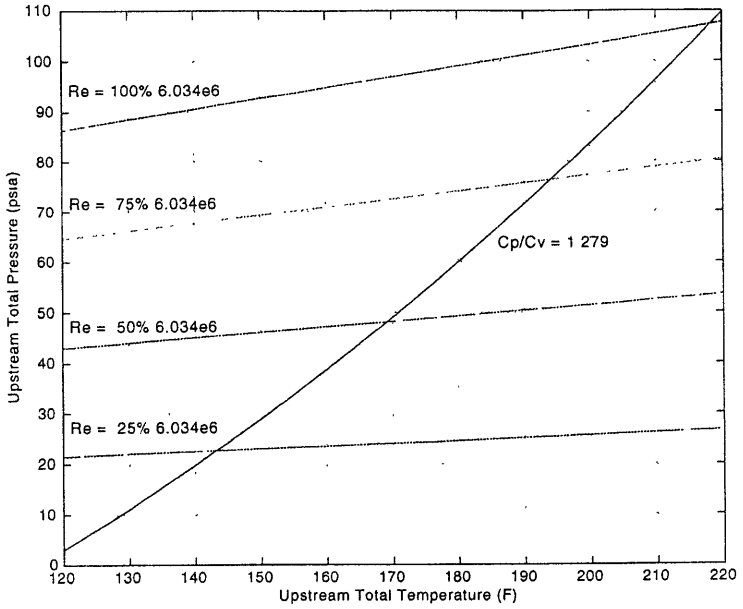

Figure 2-5: Total Temperature and Pressure for Simultaneous Matching of Reynolds Number and Specific Heat Ratio for CO_2

$$P_{T4} = \frac{\mu\sqrt{R\,T_{T4}}}{L_{ref}} \cdot \frac{R_e}{W_c} \tag{2.4}$$

This is a relationship between total temperature and pressure and Reynolds number given corrected flow. With this relationship, the iteration of inlet total temperature and pressure can proceed as follows. A total temperature is assumed and the pressure required for Reynolds number simulation is calculated as above. At this temperature and pressure, the specific heat ratio is determined from gas property tables and compared to the desired value and total temperature is adjusted accordingly. This continues until the specific heat ratio converges. This process is demonstrated graphically in Figure 2-5 where lines of constant Reynolds number and specific heat ratio are plotted on the total temperature and pressure plane.

Once the inlet temperature and pressure are known, the mechanical speed is set to match the desired corrected speed as follows:

$$N_{mech} = \frac{\sqrt{\gamma\, R\, T_{T4}}}{L_{ref}} \cdot N_{cor} \tag{2.5}$$

This comes directly from the definition of corrected speed.

The target total pressure ratio is always known and is equal to the stage design pressure ratio. This is adjusted by varying the downstream throttle plate area. To estimate the required area, mass flow is written in terms of Mach number and stagnation quantities:

$$\dot{m}_t = \sqrt{\gamma_5}\, M_{th} \left[1 + \frac{\gamma_5 - 1}{2} M_{th}^2\right]^{-\left[\frac{\gamma_5+1}{2(\gamma_5-1)}\right]} \cdot \frac{P_{T5}\, C_D\, A_{th}}{\sqrt{R\, T_{T5}}} \tag{2.6}$$

This provides a relationship between known mass flow and required throttle plate area because all other quantities are known. Because the throttle is choked, $M_{th} = 1$. P_{T5}, the total pressure at the throttle plate, or equivalently, the downstream total pressure, is calculated from the upstream total pressure and desired pressure ratio. T_{T5} requires an assumed adiabatic stage efficiency, η_t, and takes the form:

$$T_{T5} = T_{T4} \cdot \tau_t = T_{T4} \left[1 - \eta_t \left(1 - \pi_t^{\frac{\bar{\gamma}-1}{\bar{\gamma}}}\right)\right] \tag{2.7}$$

for an average value of specific heat ratio, $\bar{\gamma}$. R and γ_5 are known gas properties and discharge coefficient, C_D, is well calibrated from many previous runs. This procedure allows a simple, but approximate, calculation of the required downstream throttle plate area to achieve the desired pressure ratio.

Finally, the eddy current brake excitation must be set to absorb the power produced by the turbine. Ideally, this setting will hold corrected speed constant through the test window. The calculation of this excitation is based on a model of the brake developed during its design. More information on this subject can be found in Reference [2]. Table 2.1 summarizes typical Blowdown Turbine operating conditions.

Table 2.1: Typical Blowdown Turbine Operating Conditions

Parameter	Value
Working Fluid	CO_2
Specific Heat Ratio	1.279
Mean Metal Temperature	300 K (81°F)
Hub Radius	0.226 m
Reynolds Number	$6.034e^6$
Inlet Total Pressure	7 atm (105 $psia$)
Exit Total Pressure	3.47 atm (52 $psia$)
Inlet Total Temperature	375 K (215°F)
Exit Total Temperature	325 K (126°F)
Prandtl Number	0.742
Design Rotor Speed	5954 rpm
Design Mass Flow	23.3 kg/s
Power Output	1.08 MW
Test Time	$\approx$ 500 ms

2.5 Instrumentation

2.5.1 Introduction

The nature of the short duration experiment casts a strict requirement on the time response of instrumentation used to sample its flow field. Performance calculations using flow measurements also require a high level of instrumentation accuracy. Fortunately, scaling, as discussed in Section 2.4, allows a rather benign experimental environment condusive to flow measurement. And of course, low development cost is always a requirement. These considerations have recently led the Blowdown Turbine project to develop new total temperature and pressure instrumentation with the goal of accurately characterizing turbine performance. The design of this new instrumentation is detailed in Reference [4]. Also presented is an analysis of the overall uncertainty in total temperature and pressure measurements. Here, the results of this effort will simply by outlined. Following this is a brief explanation of other instrumentation used in the Blowdown Turbine, all of which is summarized in Table 2.2. Finally, the standard differential pressure transducer calibration

procedure is discussed followed by an explanation of the downstream translator, a device used to circumferentially survey the downstream flow field.

2.5.2 Total Temperature Instrumentation

Over the past 10 years, many total temperature probes have been designed with the above criteria in mind. With each new design, time response and instrument accuracy generally improved. The most recent design, however, focused on the heat transfer processes that heat the thermocouple wire to its indicated temperature. This analysis led to a design with much lower heat losses and a quicker time response than previously achieved as smaller diameter thermocouple wire was employed. Attention was also paid to the probe head design in order to reduce probe sensitivity to flow angle. This is important downstream of the rotor where wake measurements are made.

The results of this effort are shown in Figures 2-6 and 2-7, both taken from Reference [4]. This probe is located downstream of the turbine on the translator, described in Section 2.5.6, along with an identical probe with four heads. A stationary six head version is mounted upstream of the turbine. The mean uncertainty in total temperature measurement over the three probes is estimated to be approximately 0.13 K [4]. These probes are identified as TTR101,1-6, TTR103,1-5, and TTR104,1-4 in Table 2.2.

2.5.3 Total Pressure Instrumentation

Total pressure probes are not subject to the heat losses that made the design of highly accurate total temperature probes so difficult. The primary concerns in the design of total pressure probes are fast time response and flow angle insensitivity.

To achieve the desired time response, piezoresistive strain gauge type pressure transducers were employed. These transducers are very sensitive to pressure change and provide fast time response. The disadvantage of using this type of transducer is their tendency to exhibit non-linearity and hysteresis. This is the reason for the exhaustive calibration procedure described in Section 2.5.5. To allow a larger range of inlet flow angle to the probe

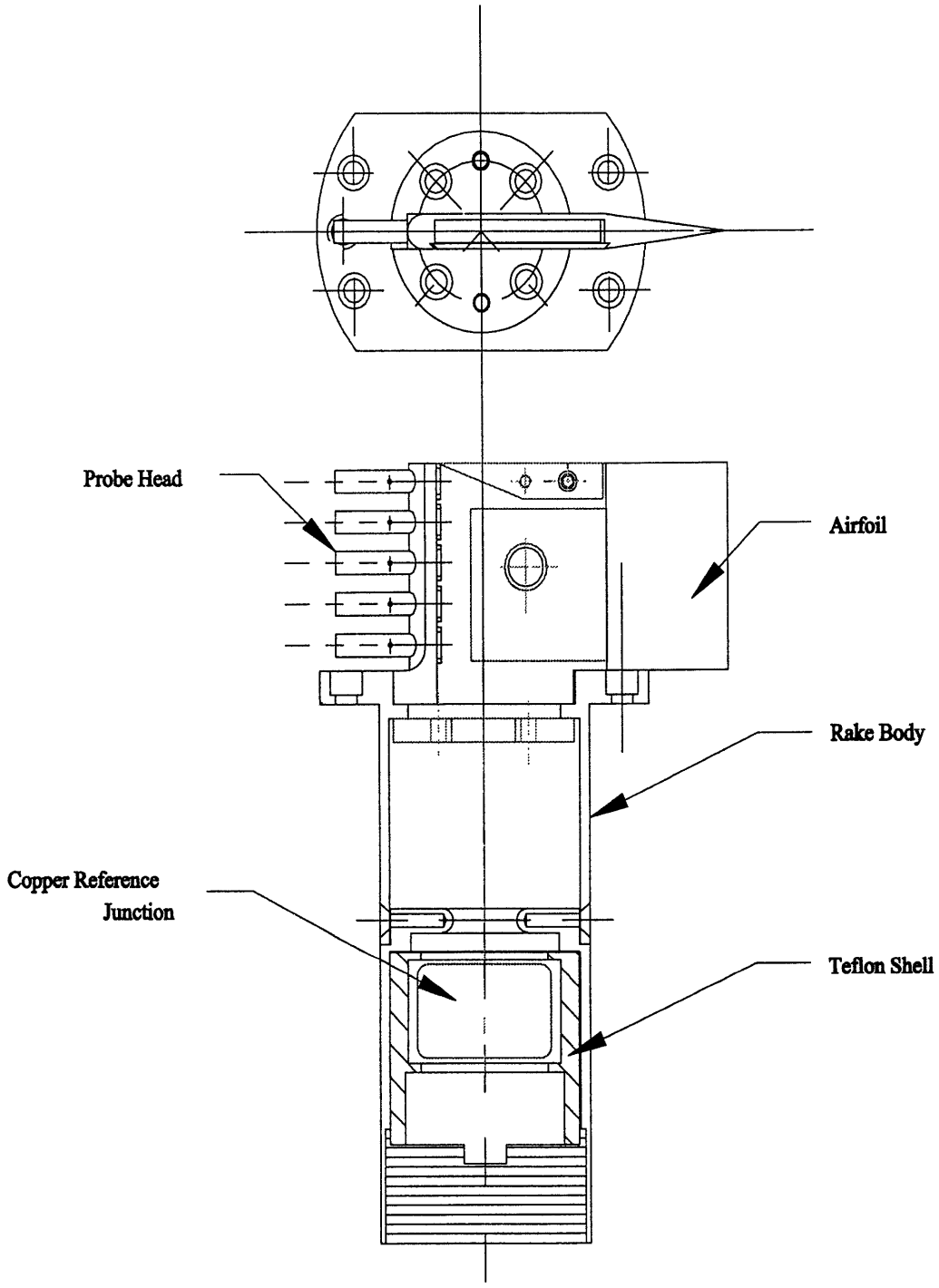

Figure 2-6: Downstream Total Temperature Probe (Full Scale)

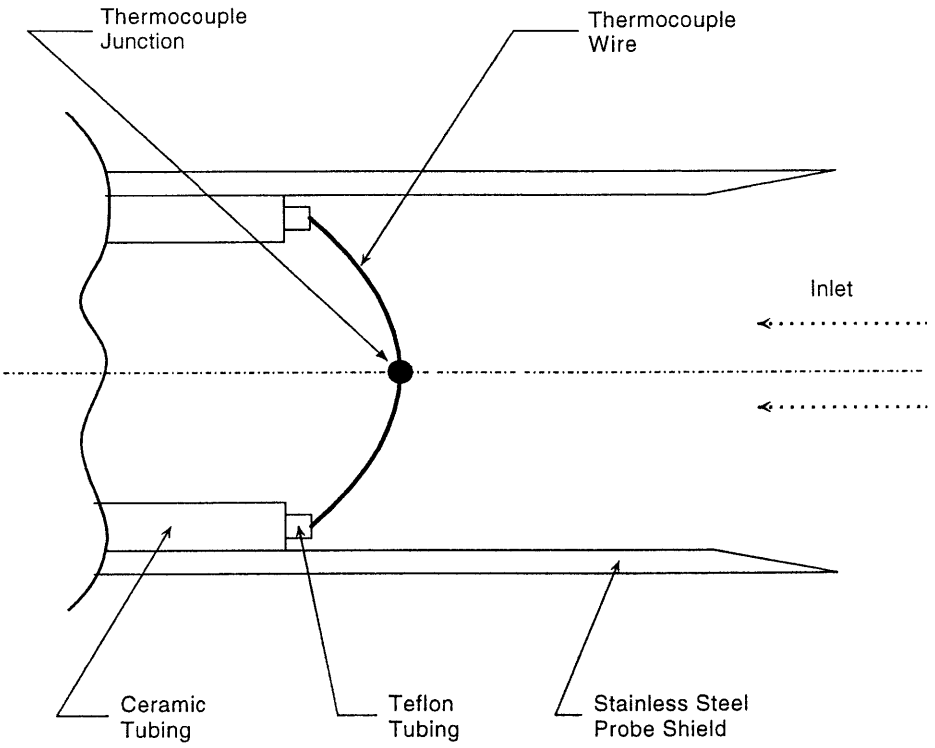

Figure 2-7: Downstream Total Temperature Probe Head (Not to Scale)

head, reducing its flow angle sensitivity, a 15° beveled impact head was chosen. Acceptable flow angles are estimated to be ±27.5°. The pressure transducers, 100 *psig* XCQ-063-100's, are mounted inside the probe body below the heads. Transducer reference backpressure is provided by an external vacuum pump via Tygon tubing.

The final result is externally identical to the total temperature probe shown in Figure 2-6 but consisting of eight heads. It appears in Table 2.2 as PT45R,1-8. A single total pressure probe head of this type, PT2YR3 in Table 2.2, is used upstream. The estimated average uncertainty in total pressure measurement from these nine heads is 0.254% of the true total pressure [4].

2.5.4 Other Instrumentation

Sections 2.5.2 and 2.5.3 describe the new total temperature and pressure instrumentation developed by the Blowdown Turbine to make highly accurate measurements of the flow field. In addition, there are many other measurements necessary to characterize turbine performance. These are described below.

Facility reference instrumentation provides known conditions for use in calibration procedures. Here, time response is traded for absolute accuracy and stability as all tunnel temperature and pressure measurements are based on these references. Pressure references are available in the supply tank and test section via slower, but more accurate capacitive type pressure transducers. Located in the supply tank is a Sensotec Super TJE 150 *psia* transducer labeled PREF150 in Table 2.2; PREF050, a Sensotec TJE 50 *psia* transducer, is located in the upstream test section. Upstream dynamic pressure probes are referenced to PREF001, a Setra 228 1 *psid* capacitive type pressure transducer. Temperature references are available from TREF10, an upstream temperature reference junction, and from the newly acquired Omega TRCIII ice point calibration cell. Efforts are now being made to convert all temperature references to the ice point to simplify temperature data reduction.

Turbine speed is monitored by a digital encoder. The eddy current brake excitation and current are recorded as is the translator position by its own digital encoder. The eddy current brake load cell data, for use in determining turbine torque, is monitored along with shaft and bearing vibration. In addition to the total temperature and pressure probes previously described, there exist various other such measurement devices throughout the tunnel, all summarized in Table 2.2.

2.5.5 Transducer Calibration

The standard calibration procedure is responsible for the calibration of all differential pressure transducers. It is performed immediately after the supply tank is filled and at the conclusion of each experiment. Calibration data just before and after each experiment allows transducer drift and nonlinearity to be quantified. Figure 2-8 shows an actual calibration

Table 2.2: Blowdown Turbine Instrumentation

Run Name	Type[1]	Location	DAQ System[2]
PREF150[3]	Absolute Pressure	Supply Tank	3
PREF050[3]	Absolute Pressure	Upstream	3
PREF001[3]	Differential Pressure	Upstream	3
TREF10[3]	Temperature	Upstream	3
FTACH	Digital Speed	Shaft	1,2,3
ATACH	Analog Speed	Shaft	1,2,3
VTOT	Excitation	Eddy Current Brake	3
ITOT	Current	Eddy Current Brake	3
IBRK	Current	Eddy Current Brake	2,3
DSTPOS	Digital Encoder	Translator	3
ECBF,1-2	Load Cell	Eddy Current Brake	1,2,3
FBRING	Shaft/Bearing Vibration	Forward Bearing	3
RBRING	Shaft/Bearing Vibration	Rear Bearing	3
PT0,A-B	Differential Pressure	Supply Tank	3
PNOZ	Differential Pressure	Venturi Nozzle	1,2,3
PDMP	Differential Pressure	Dump Tank	3
PT2,A-C	Differential Pressure	Upstream	3
TT2,A-C	Temperature	Upstream	3
PP2,A-C	Differential Pressure	Upstream	3
PT2YR3	Differential Pressure	Upstream	3
PT45R,1-8	Differential Pressure	Translator	3
P45HUB	Differential Pressure	Translator	3
P45A	Differential Pressure	Downstream	3
TTMFM1	Temperature	Diffuser Section	1,3
TTNOZ,1-2	Temperature	Venturi Nozzle	1,3
TTR101,1-6	Temperature	Upstream	2
TTR103,1-5	Temperature	Translator	2
TTR104,1-4	Temperature	Translator	2

trace from transducer PT2YR3 during experiment 011. This figure and the calibration sequence are described below.

First, all transducers are provided a vacuum backpressure reference by an external

[1]All temperatures and pressures are total except P45HUB and P45A.
[2]*DAQ System* is defined in Table 2.3.
[3]Facility reference used for calibration purposes.

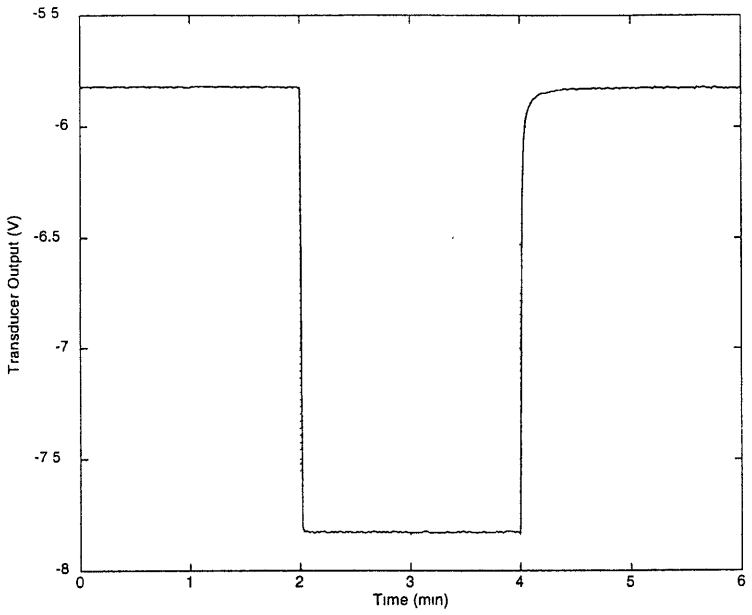

Figure 2-8: PT2YR3 Differential Pressure Transducer Calibration Trace

vacuum pump. For a postfill calibration, this produces a zero pressure differential across all transducers in the tunnel portion of the facility and a pressure differential equal to the initial supply tank pressure for all supply tank transducers. Data is taken at this condition for approximately 2 min as shown by the first portion of the calibration trace shown in Figure 2-8. At this point, the backpressure reference is exposed to atmosphere. This decreases the pressure differential across all transducers by the current local atmospheric pressure. Again, data is taken for 2 min as shown by the second portion of Figure 2-8. The last section of Figure 2-8 shows transducer reference pressure returning to vacuum where it remains during the blowdown experiment.

This calibration data provides a voltage change for each differential pressure transducer corresponding to exactly the local atmospheric pressure allowing calculation of transducer scale. Transducer zeros are normally taken to be the average output during an experiment prior to the opening of the fast-acting valve. With transducer scale and zero data, voltages taken during the blowdown experiment are converted to units of pressure using the linear

calibration relation:

$$P_{atm} = (P_{volts} - Zero) \cdot Scale \tag{2.8}$$

2.5.6 Downstream Translator

The flow entering the nozzle guide vanes from the fast-acting valve is essentially circumferentially symmetric. This allows stationary upstream measurements to be representative of the entire circumferential flow field. Downstream, however, the presence of the nozzle guide vanes is apparent by circumferential nonuniformities caused by their wakes. In this region, stationary flow field measurements are biased by their circumferential location; the temperature and pressure inside and outside of a wake are not the same. This presents a complication in downstream flow field measurements especially in a short-duration experiment. The Blowdown Turbine solution to this problem is the downstream translator.

The translator is a large cylindrical drum mounted downstream of the rotor. It contains three 41-pin Bendix electrical connection canisters separated by 20°. Each canister is capable of carrying either of the total temperature or pressure probes described in Sections 2.5.2 and 2.5.3. Located 40° ahead of the first canister is a static pressure tap, labeled P45HUB in Table 2.2.

The translator is free to rotate approximately 350°, restricted by a spring loaded hard stop. The hard stop is designed to prevent the translator from spinning freely and destroying the canister wiring. During an experiment, the translator is driven by a Baldor ME-4090-BLBCE servomotor delivering approximately 3 $in-lb$ of torque through an equivalent 13.5:1 gear ratio. This motor is controlled by a Galil DMC-400-10 card and powered by a Copley MB6-10 amplifier. In addition to the hard stop, an aluminum shear pin is installed on the shaft coupling exiting the servomotor to prevent translator runaway.

Figure 2-9 shows the typical translator motion during a blowdown experiment. The translator rotates at a constant angular velocity of approximately 0.25 rps throughout the test window. The motion is programmed so that all instrumentation remains between 0°

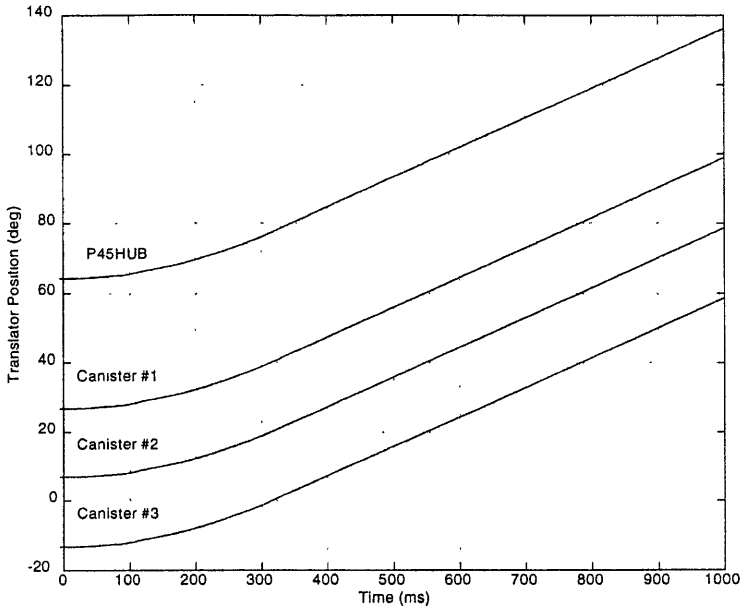

Figure 2-9: Typical Downstream Translator Programmed Motion

and 120° during this time. These correspond to upstream wind tunnel strut locations, behind which flow field measurements are contaminated.

2.6 Data Acquisition

The short duration nature of the blowdown experiment not only places special requirements on instrumentation, but on data acquisition (DAQ) as well. The DAQ systems must monitor all instrumented channels at a sampling rate sufficient to capture all time scales of interest for the duration of the experiment. For aerodynamic performance measurements, which is the focus of this work, 5 kHz is sufficient to resolve the necessary time scales. Although to accurately monitor turbine speed, the 200 kHz high-speed system is often utilized. The DAQ envelope typically spans $2-4$ s to record useful data and monitor tunnel "spin-down." The precise clocking sequence can be modified to capture the desired window. In addition, posttest calibration, discussed in Section 2.5.5, lends further insight into the posttest tunnel

Table 2.3: Blowdown Turbine Data Acquisition

Specification	Dell OMNIPLEX 590	Dell 486D/50	Dell 466/T
System	1	2	3
Speed	High	Low	Low
Operating System	DOS	DOS	Win95
DAQ Platform	DOS-Based[4]	DOS-Based[4]	LabVIEW
DAQ Board	Adtek AD-830	Analogic HSDAS-16	NI MIO-64E3
Board Resolution	12-bit	16-bit	12-bit
Board Channels	8	16	64
Number Of Boards	4	4	1
Total Channels	32	64	64
Typical Sampling Rate	200 kHz	2.5 kHz	5 kHz

state.

The current DAQ system consists of three computers. Two low-speed systems, each of which is capable of monitoring up to 64 channels, sample at 2.5 kHz and 5 kHz. The high-speed system monitors eight channel at up to 200 kHz. Table 2.3 summarizes the Blowdown Turbine DAQ equipment.

2.7 Chapter Summary

This chapter has discussed the MIT Blowdown Turbine short duration experimental facility used to acquire turbine data for calculation of adiabatic efficiency. It has covered run-time preparations including determination of blowdown operating conditions to achieve full-scale turbine similarity. The design of new total temperature and pressure instrumentation for highly accurate flow field measurements was briefly discussed along with other instrumentation used to characterize turbine performance. This was followed by descriptions of the standard differential pressure transducer calibration procedure and the downstream translator, a device for circumferentially surveying the downstream flow field. This chapter concludes with information on Blowdown Turbine data acquisition.

[4]Inhouse DOS-Based Fortran Routines

Chapter 3

Analysis of Experimental Data

3.1 Introduction

Numerous blowdown experiments were conducted during this work to simulate different full-scale engine operating points. In addition, all operating points were repeated for two tip clearances to quantify the effect of larger tip clearance, resulting in increased secondary flow, on turbine adiabatic efficiency. This chapter will first present the full-scale engine operating points tested along with the corresponding blowdown test conditions required for experimental similarity. Standard calculations utilized in verifying experimental similarity will then be explained. Finally, close attention to test data will reveal many unique properties of turbomachinery flow and of the transient, short duration experimental technique used for this work. Data from experiment 032 will be used to illustrate these properties.

3.2 Experimental Test Conditions

Table 3.1 summarizes the full-scale engine operating points simulated during this work. This test matrix will provide data at higher and lower than design stage pressure ratio and corrected speed. A one-half Reynolds number simulation is also included. Additionally, all operating points will be repeated at two tip clearances.

Through the process of scaling of the full-scale engine operating point, discussed in

Table 3.1: Full-Scale Engine Operating Points Simulated

Experiment	π_t	R_e	N_{cor}	Tip Clearance
1	π_t	R_e	N_{cor}	$0.5\,\delta$
2	${\pi_t}^+$	R_e	N_{cor}	$0.5\,\delta$
3	${\pi_t}^-$	R_e	N_{cor}	$0.5\,\delta$
4	π_t	R_e	${N_{cor}}^+$	$0.5\,\delta$
5	π_t	R_e	${N_{cor}}^-$	$0.5\,\delta$
6	π_t	$0.5\,R_e$	N_{cor}	$0.5\,\delta$
7	π_t	R_e	N_{cor}	δ
8	${\pi_t}^+$	R_e	N_{cor}	δ
9	${\pi_t}^-$	R_e	N_{cor}	δ
10	π_t	R_e	${N_{cor}}^+$	δ
11	π_t	R_e	${N_{cor}}^-$	δ
12	π_t	$0.5\,R_e$	N_{cor}	δ

Section 2.4, the operating points summarized in Table 3.1 are translated into blowdown experimental test conditions, summarized in Table 3.2. These are the conditions at which the experiments are conducted to achieve full-scale turbine similarity. The second set of six experiments duplicates the first set at larger tip clearance. This clearance is achieved by installing the proper diameter ablatable rub strip surrounding the rotor blades.

3.3 Similarity Verification Calculations

Every blowdown experiment produces approximately 1 *million* data points. What follows is a discussion on how this data is used in calculations intended to characterize turbine performance and verify that test conditions are met, a necessary condition for experimental similarity. All calculations described in this section are provided in Appendix A for each experiment conducted.

One of the first priorities at the conclusion of an experiment is verification of pressure ratio. Many total pressure measurements are made both upstream and downstream, as shown in Table 2.2, and these measurements must be processed to determine the true total pressure at these locations before calculating pressure ratio. Upstream, this measurement

Table 3.2: Blowdown Turbine Experimental Test Conditions

Experiment	Name	$P_{T4}\,(psia)$	$T_{T4}\,(F)$	$N_{mech}\,(RPS)$	$V_{brk}\,(V)$	$A_{th}\,(in^2)$
1	024	104.5	217	82.7	210.8	40.25
2	027	104.5	217	82.7	224.6	47.25
3	032	104.5	217	82.7	190.5	33.25
4	029	104.5	217	87.4	198.3	40.25
5	028	104.5	217	79.1	211.6	40.25
6	021	47.0	180	85.0	132.0	40.25
7	034	104.5	217	82.7	205.0	40.25
8	035	104.5	217	82.7	216.8	47.25
9	033	104.5	217	82.7	190.5	33.25
10	037	104.5	217	87.4	198.3	40.25
11	036	104.5	217	79.1	211.6	40.25
12	041	47.3	175	80.3	135.1	40.25

is available at three circumferential locations between supply tank struts. Typically these measurements are identical, thus, they may simply be averaged. Downstream, this measurement is made at only one circumferential location, but at a series of radial locations. Here, the radial velocity profile dictates the center heads be weighted more heavily than the outside heads in determining a mass-averaged total pressure. For the purpose of this analysis, this velocity profile is assumed near full so that each head may be weighted equally; pressure ratio is then calculated as follows:

$$\pi_t = \frac{P_{T5,radial\,avg}}{P_{T4,circ\,avg}} \tag{3.1}$$

Similarly, mass-averaged upstream and downstream total temperatures are determined and used in calculating temperature ratio:

$$\tau_t = \frac{T_{T5,radial\,avg}}{T_{T4,circ\,avg}} \tag{3.2}$$

Again, subscripts four and five represent upstream and downstream conditions respectively.

Reynolds number, another non-dimensional similarity parameter, is also verified proceeding an experiment. As written in Equation 2.2, Reynolds number is proportional to

turbine mass flow, calculated from critical-flow venturi calibration data, and inversely proportional to dynamic viscosity, a gas property determined from property tables. Specific heat ratio, another non-dimensional similarity parameter verified at the conclusion of each experiment, is found directly from property tables.

Corrected speed must also be verified. In terms of percent of its design value, corrected speed is written as:

$$N_{cor,\%des} = \frac{100}{N_{cor,des}} \cdot \frac{L_{ref}\, N_{mech}}{\sqrt{\gamma_4\, R\, T_{T4}}} \tag{3.3}$$

Speed is controlled by the eddy current brake. As described in Section 2.2, the eddy current brake provides a braking torque which is reacted through two load cells fastened to the test section. Data from these load cells enables calculation of turbine torque through the established calibration:

$$\mathcal{T}\,[\mathcal{N} \cdot m] = 683.67 \cdot (ECBF1 - ECBF2) - \mathcal{T}_0 \tag{3.4}$$

Turbine torque and speed are then used to calculate turbine power[1]:

$$\mathcal{P}\,[\mathcal{W}] = \mathcal{T} \cdot \omega \tag{3.5}$$

As discussed in Section 2.4, experimental similarity requires that the non-dimensional similarity parameters be reproduced. These parameters were determined to be pressure ratio, corrected speed, specific heat ratio, and Reynolds number, all of which are plotted versus time for each experiment in Appendix A. The period of time when these parameters are constant and equal to full-scale turbine design values is the time when similarity is achieved. This window varies from test to test as seen, however, it generally spans approximately $300 - 800\ ms$. This is also the time when efficiency predictions, discussed in the next two chapters, will be representative of the full-scale turbine.

This concludes the discussion on standard calculations used in characterizing turbine

[1]This neglects rotor acceleration accounted for in Section 5.3.2.

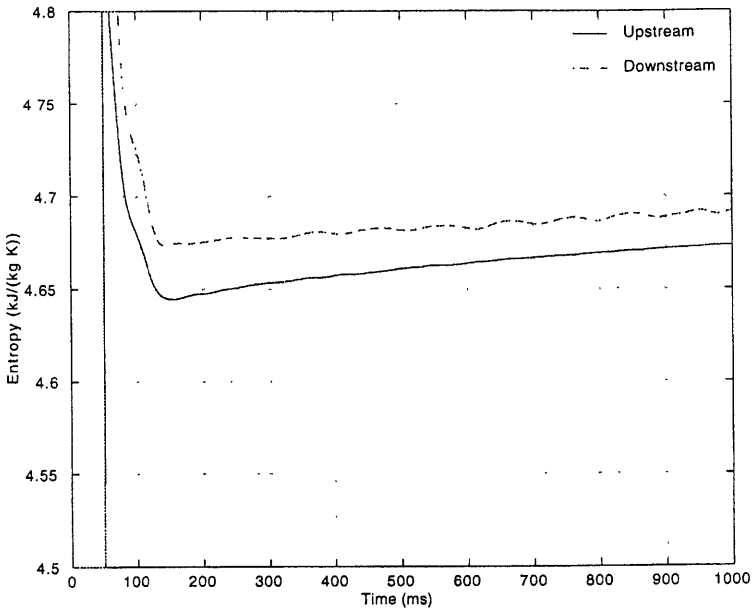

Figure 3-1: Experiment 032 Upstream and Downstream Entropy

performance and verifying experimental similarity. Next, through these calculations and raw experimental data, unique properties of turbomachinery flow and of the blowdown experimental technique used for this work will be demonstrated.

3.4 Verification of Isentropic Valve Expansion

In setting blowdown test conditions to achieve full-scale turbine similarity, the required upstream total pressure, calculated along with upstream total temperature to simultaneously match Reynolds number and specific heat ratio as described in Section 2.4, is implemented in the supply tank. This assumes the flow, in expanding from the supply tank into the upstream test section, maintains constant total pressure so that the initial total pressure upstream of the turbine is equal to that value necessary for similarity. In short, the valve expansion must be isentropic and this must be verified before analysis can proceed.

Figure 3-1 shows upstream and downstream entropy versus time during experiment

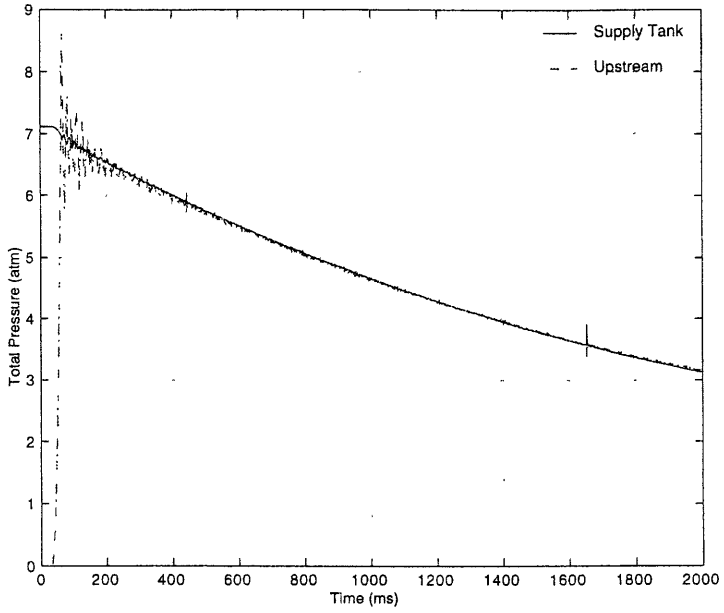

Figure 3-2: Experiment 032 Supply Tank and Average Upstream Total Pressure

032. For the valve expansion process to be isentropic, supply tank entropy should be constant in time and equal to upstream entropy. High-speed supply tank temperature is not available preventing calculation of supply tank entropy, however, it can be seen in Figure 3-1 that upstream entropy remains constant to within approximately 1% of its absolute value. Perhaps a more meaningful comparison of valve expansion entropy generation is against the entropy generation across the turbine stage. Again referring to Figure 3-1, the increase in upstream entropy between $0 - 1000\ ms$, the time in which similarity may be reasonably assumed, is on the same order as the entropy generation across the turbine stage. What does this say about the valve expansion process? Certainly, the turbine expansion is not isentropic. Is this to say the valve expansion process is similarly non-isentropic?

Again, the purpose of verifying the valve expansion process to be isentropic is to ensure that the total pressure required for full-scale turbine similarity is enforced upstream of the turbine, not simply in the supply tank. Figure 3-2 shows the measured total pressure in the supply tank and directly upstream of the turbine for experiment 032. The pressure traces

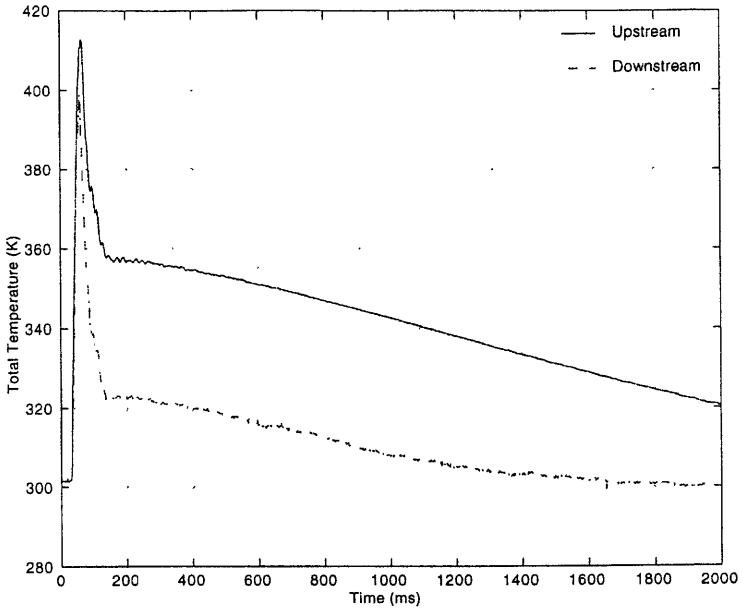

Figure 3-3: Experiment 032 Average Upstream and Downstream Total Temperature

are indistinguishable. Clearly, upstream total pressure is consistent with the value required for similarity. The is sufficient to verify the valve expansion process to be near isentropic and that upstream total pressure is being properly enforced.

3.5 Compressional Heating

The first obvious characteristic of all blowdown temperature traces is the large spike around 50 ms. This is the effect of what is known as compressional heating. This process is a natural characteristic of the transient tunnel start-up process and came to be understood through dynamic models of the blowdown facility put together during its development. Here, it is explained in terms of the thermodynamics of the fast-acting valve expansion process.

Figure 3-3 shows the upstream and downstream total temperature during experiment 032, initial supply tank temperature 220 $°F$ or 378 K. As seen here, the upstream total temperature, shortly after opening of the fast-acting valve, exceeds the initial supply tank

total temperature. According to the first law of thermodynamics written for a calorically perfect gas,

$$\bar{C}_P \cdot \delta T_T = \delta w - \delta q \tag{3.6}$$

total temperature can change only as a result of work or heat transfer. This says the flow entering the upstream test section experiences one or both. However, this flow simply undergoes an isentropic expansion, as shown in the previous section, to a very low Mach number[2], and seemingly, to the same total temperature.

It turns out, the expansion of gas into a large volume contributes work to and increases the total temperature of the gas inside. Reynolds calls this process "Charging of a high-pressure tank" [6]. It is modeled as a valve supplying a steady one-dimensional inflow to a large adiabatic tank. Further assuming calorically perfect gas behavior and perfect mixing and neglecting kinetic energy inside the tank, the first law of thermodynamics applied to the tank from time zero to time t takes the form [6]:

$$\Delta U_t = \dot{m}_v \, h_v \, t \tag{3.7}$$

where subscript t indicates a condition inside the tank and subscript v, at the valve. This says the internal energy inside the tank increases with the inflow of enthalpy. Applying conservation of mass yields [6]:

$$\dot{m}_v \, h_v \, t = \left(m_t\left(0\right) + \dot{m}_v \, t\right) \, u_t\left(t\right) - m_t\left(0\right) \, u_t\left(0\right) \tag{3.8}$$

Now, perfect gas behavior is assumed to express enthalpy and internal energy in terms of temperature [6]:

$$\dot{m}_v \, \bar{C}_P \, T_v \, t = \left(m_t\left(0\right) + \dot{m}_v \, t\right) \, \bar{C}_V \, T_t\left(t\right) - m_t\left(0\right) \, \bar{C}_V \, T_t\left(0\right) \tag{3.9}$$

[2]Measured upstream dynamic pressure is typically 0.5% of the measured upstream total pressure [5].

This is an expression for the temperature inside the tank as a function of inlet conditions and time.

In applying this model to the blowdown facility, zero initial mass is assumed as the test section begins the experiment evacuated; in other words $\dot{m}_t(0) = 0$. Equation 3.9 then becomes

$$T_t = \gamma \cdot T_v \tag{3.10}$$

This says immediately after the fast-acting valve opens, the (total) temperature in the upstream test section becomes the supply tank total temperature multiplied by specific heat ratio, a number always larger than unity. This increase in total temperature is due to flow work applied to the gas in the upstream test section by the gas expanding from the supply tank.

This process is known as compressional heating in the Blowdown Turbine and produces the temperature spikes shown in Figure 3-3. Just as quickly as it occurs, the volume of hot gas is convected downstream and temperature decreases along the downwind portion of these temperature spikes. In short, these spikes are simply the impulse response of the total temperature instrumentation. Since its prediction, compression heating has been recognized as a novelty and an indication of the fast time response of the instrumentation used to measure it.

3.6 Nozzle Wake Measurements

In discussing the translator in Section 2.5.6 it was explained that flow field circumferential nonuniformities will be created downstream due to nozzle wake shedding. This is the reason why the downstream translator is necessary. Flow field measurements in this region will vary depending on the circumferential position that they are taken. The translator allows a circumferential survey capturing several of the 44 nozzle wakes during the time when similarity is achieved, depending on the rotational speed. Typically the translator operates

at near 0.25 RPS to maintain all instrumentation between wind tunnel support struts. This allows measurements over approximately 5.5 $wakes$ between $300 - 800$ ms, a probe wake passing frequency of 11 Hz.

Figure 3-4 shows a downstream total temperature trace taken during experiment 032 from probe TTR104-4. A single low frequency component of amplitude near 3 K is clearly visible in the region of $100 - 1000$ ms. Figure 3-5 is the FT, or Fourier Transform, of this temperature signal displaying the actual frequency content. As expected, this low frequency component is very near 11 Hz, the frequency at which the temperature probe is traversing the nozzle wakes.

This circumferential nonuniformity might be expected to appear in total pressure measurements as well. In fact it does. Figure 3-6 shows downstream total pressure sensor PT45R8 during the same experiment, 032. A very similar low frequency component is observed of magnitude near 0.20 atm or 2.94 $psia$. From the frequency content calculation, shown in Figure 3-7, this component is again determined to be near 11 Hz.

This data shows sinusoidal downstream circumferential nonuniformities in total temperature and pressure of magnitudes near 3 K and 3 $psia$. These nonuniformities are shown to be at the frequency at which the measurement probes are traversing the nozzle wakes. This clearly indicates measurement of nozzle cooling. The flow directly downstream of each nozzle, within its wake, experiences more heat transfer than the flow outside of this region reducing its temperature and pressure. This data reaffirms the need for translating downstream flow field measurements provided by the downstream translator.

3.7 Radial Temperature Profiles

As shown in Figure 2-5, the initial supply tank temperature required for full Reynolds number simulation at the design specific heat ratio is near 375 K, or 215 $^{\circ}F$. This is very low by full-scale turbine standards but significantly higher than ambient, the temperature at which the test section begins. This temperature difference will form a thermal boundary layer in the test section once flow is established through the turbine. The radial distribution of

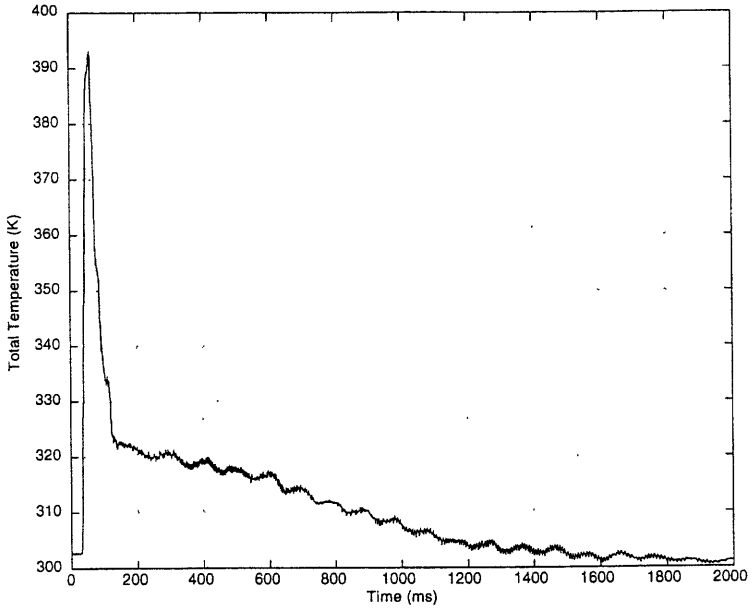

Figure 3-4: Experiment 032 Downstream Total Temperature (TTR104-4)

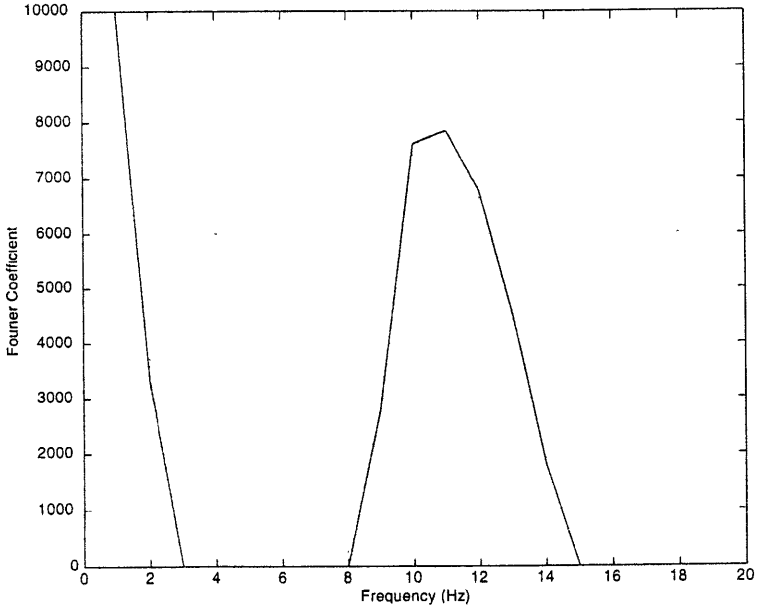

Figure 3-5: Experiment 032 Downstream Total Temperature FT (TTR104-4)

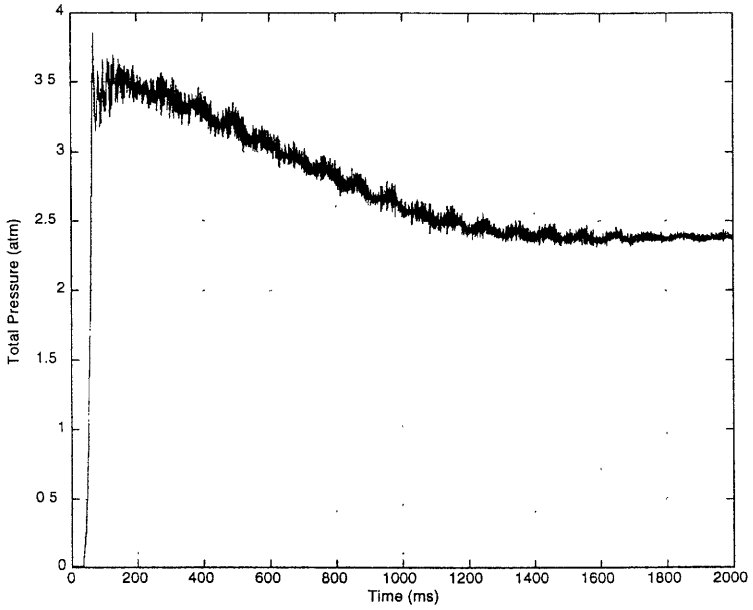

Figure 3-6: Experiment 032 Downstream Total Pressure (PT45R8)

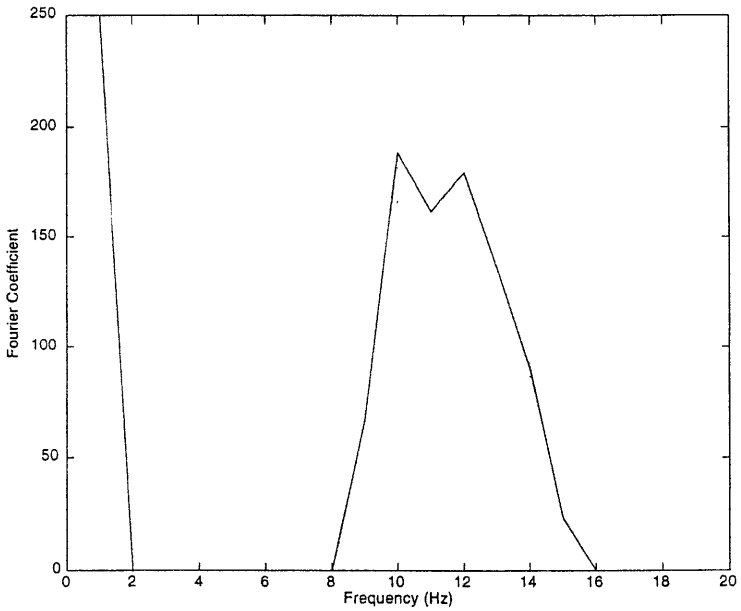

Figure 3-7: Experiment 032 Downstream Total Pressure FT (PT45R8)

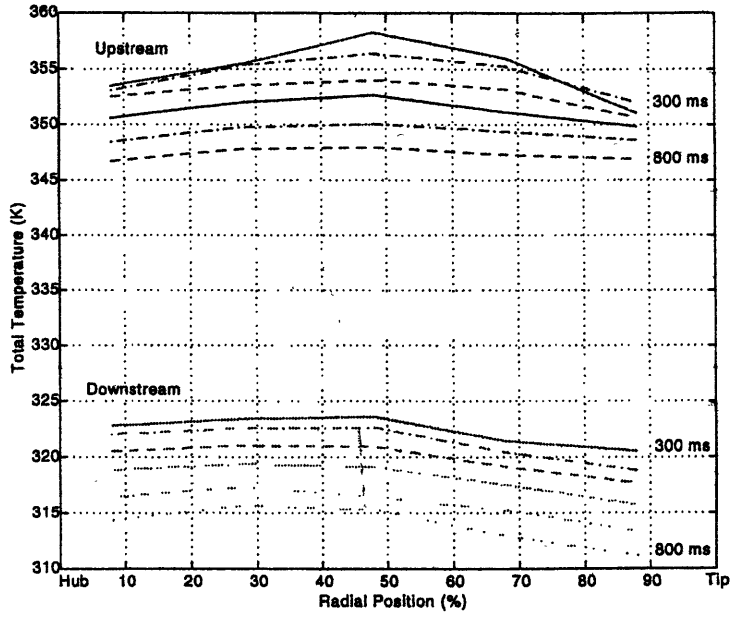

Figure 3-8: Experiment 032 Total Temperature Radial Profiles

total temperature probes, labeled TTR101,1-6, TTR103,1-5, and TTR104,1-4 in Table 2.2, is specifically designed to measure this flow feature.

Figure 3-8 shows upstream and downstream radial total temperature profiles observed during experiment 032. Each curve represents the profile at a different point in time: 300, 400, 500, 600, 700, and 800 ms profiles are shown. From this data, a thermal boundary layer of time-varying magnitude is evident. Early in the experiment, the meanline gas temperature is near the initial supply tank temperature and the turbine metal temperature is near ambient producing a radial temperature variation of order 5 K. As the experiment continues, the supply tank temperature decreases isentropically with supply tank pressure and the turbine metal temperature increases due to heat transfer. These effects decrease the magnitude of the thermal boundary layer in time. By 800 ms, the upstream total temperature profile is nearly flat. It is important to note that the supply tank temperature decreases much more than the turbine metal temperature increases. This increase in metal temperature is due to heat transfer and is small due to the short duration of the experiment.

Its exact magnitude, however, will be explored in Section 4.5 as it is required to correct aerodynamic efficiency predictions.

3.8 Chapter Summary

This chapter began by introducing the full-scale turbine operating points simulated during this work and the corresponding blowdown operating conditions required for similarity. A discussion on calculations intended to characterize turbine performance and verify matching of non-dimensional similarity parameters followed. Finally, unique properties of turbomachinery flow and of the short duration experimental technique used were observed through analysis of these calculations and of the experimental data. These properties included isentropic valve expansion, compressional heating, nozzle wake measurements, and radial temperature profiles.

Chapter 4

Aerodynamic Measurement of Adiabatic Efficiency

4.1 Introduction

This chapter will discuss turbine adiabatic efficiency measurement using the aerodynamic approach described in Section 1.2. It begins with a pre-test efficiency uncertainty analysis. This analysis is intended to estimate the level of uncertainty expected in the calculation of efficiency before the calculation takes place. This analysis will also uncover a distinction between absolute accuracy and relative precision, an important one when comparing results from back-to-back experiments. Following the uncertainty analysis, real, ideal, and perfect gas models will be explained in terms of enthalpy calculation. The goal of this discussion will be to qualify assumptions made in these models and determine how they will affect efficiency predictions. A discussion on efficiency calculation will follow. This will include the process of evaluating flow properties required for efficiency calculations as well as these calculations for experiment 024, a baseline full-scale turbine design point simulation. This chapter concludes with a discussion on transient heat transfer correction and a post-test efficiency uncertainty analysis focusing of aerodynamic efficiency prediction repeatability.

4.2 Pre-Test Efficiency Uncertainty Analysis

Prior to any experiment, a pre-test uncertainty analysis is beneficial in determining how measurement uncertainties propagate through subsequent calculations. This will provide information on the consistency, or precision of calculations, as well as their accuracy, or bias. This analysis, based on techniques developed in Reference [7], will estimate uncertainties in the inference of efficiency based on measurement uncertainties determined from calibration data. For algebraic convenience, this analysis will assume calorically perfect gas behavior so that efficiency may be written in terms of Equations 1.7 and 1.8 as follows:

$$\eta_{ad,cpg} = \frac{1 - \tau_t}{1 - \pi_t^{\frac{R_{CO_2}}{\bar{C}_P}}} \tag{4.1}$$

The first component of uncertainty is random error. This error affects measurement precision and is seen through repeated measurement of the same condition. Factors contributing to random error include instrument noise, ambient conditions, data acquisition errors, usually resulting from finite resolution, and human errors. Mathematically, random error is related to the standard deviation of a set of measurements. The statistic S, known as the precision index, approximates the standard deviation and is used to quantify random, or precision error. The adiabatic efficiency precision index is expressed in terms of a Taylor series expansion of Equation 4.1 as follows:

$$S_{\eta_{ad,cpg}} = \sqrt{\left(\frac{\partial \eta_{ad,cpg}}{\partial \tau_t} \cdot S_{\tau_t}\right)^2 + \left(\frac{\partial \eta_{ad,cpg}}{\partial \pi_t} \cdot S_{\pi_t}\right)^2 + \left(\frac{\partial \eta_{ad,cpg}}{\partial \bar{C}_P} \cdot S_{\bar{C}_P}\right)^2} \tag{4.2}$$

where uncertainty in gas constant, R_{CO_2}, has been neglected. This expression is non-dimensionalized by introducing influence coefficients. Each measurement contributing to the calculation of efficiency has associated with it an influence coefficient. This non-dimensional coefficient represents the change in efficiency resulting from a change in that measurement. Neglecting its sign, the influence coefficient is defined as:

$$C_* = \left| \frac{\partial \eta_{ad,cpg}}{\partial *} \cdot \frac{*}{\eta_{ad,cpg}} \right| \tag{4.3}$$

By direct differentiation of Equation 4.1, the influence coefficients associated with efficiency are determined to be:

$$C_{\tau_t} = \frac{\tau_t}{\left(1 - \pi_t^{\frac{R_{CO_2}}{\bar{C}_P}}\right)} \cdot \frac{1}{\eta_{ad,cpg}} \tag{4.4}$$

$$C_{\pi_t} = \frac{(1-\tau_t)\,\pi_t^{\frac{R_{CO_2}}{\bar{C}_P}}}{\left(1 - \pi_t^{\frac{R_{CO_2}}{\bar{C}_P}}\right)^2} \cdot \frac{\left(\frac{R_{CO_2}}{\bar{C}_P}\right)}{\eta_{ad,cpg}} \tag{4.5}$$

$$C_{\bar{C}_P} = \frac{(1-\tau_t)\,\pi_t^{\frac{R_{CO_2}}{\bar{C}_P}}}{\left(1 - \pi_t^{\frac{R_{CO_2}}{\bar{C}_P}}\right)^2} \cdot \frac{\left(\frac{R_{CO_2}}{\bar{C}_P}\right) ln\,(\pi_t)}{\eta_{ad,cpg}} \tag{4.6}$$

With these definitions, Equation 4.2 may be written as:

$$\frac{S_{\eta_{ad,cpg}}}{\eta_{ad,cpg}} = \sqrt{\left(C_{\tau_t} \cdot \frac{S_{\tau_t}}{\tau_t}\right)^2 + \left(C_{\pi_t} \cdot \frac{S_{\pi_t}}{\pi_t}\right)^2 + \left(C_{\bar{C}_P} \cdot \frac{S_{\bar{C}_P}}{\bar{C}_P}\right)^2} \tag{4.7}$$

The second component of uncertainty is bias, a fixed error affecting measurement accuracy. Non-zero bias is almost always unavoidable and often due to instrumentation design and/or implementation. This error may only be determined by comparing a measured condition to its exact value. Because this exact value is not usually known, a reasonable limit is sought to bound this error. Just as precision index, bias is expressed in terms of influence coefficients:

$$\frac{B_{\eta_{ad,cpg}}}{\eta_{ad,cpg}} = \sqrt{\left(C_{\tau_t} \cdot \frac{B_{\tau_t}}{\tau_t}\right)^2 + \left(C_{\pi_t} \cdot \frac{B_{\pi_t}}{\pi_t}\right)^2 + \left(C_{\bar{C}_P} \cdot \frac{B_{\bar{C}_P}}{\bar{C}_P}\right)^2} \tag{4.8}$$

Precision and bias may be combined to calculate overall uncertainty. The specific calculation depends on the interpretation of uncertainty. The standard interpretation suggests

Table 4.1: Pre-Test Efficiency Uncertainty Analysis Summary

Measurement	Nominal	C_*	$S_*/*$	$B_*/*$	t_{95}	$U_{95,abs}$	$U_{95,rel}$
τ_t	0.867	6.51	0.04%	0.03%	2.00	0.09%	0.07%
π_t	0.480	1.25	0.07%	0.25%	2.00	0.29%	0.14%
$\bar{C}_P \left(\frac{J}{kg \cdot K}\right)$	867.138	0.92	-	0.20%	2.00	0.20%	-
$\eta_{ad,cpg}$	90%	-	0.27%	0.40%	2.00	0.61%	0.49%

that the error in a particular measurement or calculation will not exceed the calculated value of uncertainty. This statement is made with a given level of confidence, t_{xx}, typically 95% or 99%. Assuming a confidence level, 95% in this case, the value of t_{95} will depend on the number of degrees of freedom, or number of measurements used to calculate the precision index S. Infinitely many degrees of freedom yields a t_{95} of 1.96, and 30, a value of 2.04. Following an analysis by Keogh [3], a value of 2.00 is chosen for t_{95} and uncertainty is expressed as:

$$U_{95} = \sqrt{(t_{95} \cdot S)^2 + B^2} \tag{4.9}$$

Table 4.1 summarizes the pre-test efficiency uncertainty analysis. Included are nominal values of measurements contributing to efficiency, their influence coefficients, precision indices, biases, and levels of uncertainty. The nominal values listed are inferred from full-scale turbine design point calculations and initial experiments prior to those examined in this work. Precision indices and biases for temperature and pressure ratio are calculated from calibration data [4]. A constant bias of 0.20% is assumed for the specific heat of CO_2 as suggested by Friend [8].

As seen from this analysis, the estimated absolute uncertainty in turbine aerodynamic adiabatic efficiency is approximately 0.61%. The most critical measurement in terms of uncertainty is seen to be total temperature. Because of the large total temperature ratio influence coefficient, errors in total temperature measurement will be magnified much more so than errors in total pressure measurement. This is not to say that the total pressure

measurement is trivial, however, as measurement techniques and transducer behavior is not considered in this analysis.

Another important conclusion of this analysis is the distinction between absolute accuracy and relative precision. As explained previously, bias is a fixed error affecting measurement or calculation accuracy. By comparing back-to-back measurements, fixed bias cancels and relative uncertainty is controlled by the measurement or calculation precision index. From Table 4.1, the precision index of efficiency is approximately

$$S_{\eta_{ad,cpg}} = \frac{S_{\eta_{ad,cpg}}}{\eta_{ad,cpg}} \cdot \eta_{ad,cpg} = 0.24\% \tag{4.10}$$

From Equation 4.9, this gives a relative uncertainty level of approximately 0.49%. This means that although any one efficiency measurement is not expected to have absolute uncertainty less than 0.50%, by comparing back-to-back experiments, the change in efficiency should have relative uncertainty within this limit.

4.3 Real Versus Ideal Gas Models for Enthalpy Evaluation

As explained in Section 1.2, turbine adiabatic efficiency measures the percentage of ideal work extracted by the turbine during adiabatic operation; it is expressed as the ratio of adiabatic and ideal work. From the first law of thermodynamics assuming no heat transfer[1]:

$$\delta w = \delta h_T + \cancel{\delta q} \tag{4.11}$$

work is given by the change in total enthalpy. In general, this change in total enthalpy may be expressed as [9]:

$$h_{T4} - h_{T5} = \int_{T_5}^{T_4} C_P(T)\, dT + \int_{P_5}^{P_4} \left[v - T\left(\frac{\partial v}{\partial T}\right)_P \right] dP + \frac{{V_4}^2 - {V_5}^2}{2} \tag{4.12}$$

[1] A correction for transient heat transfer effects will be discussed in Section 4.5.

This is the expression which must be evaluated in determining work. Different gas models, real, ideal, and calorically perfect, differ in their approximation of this expression. What follows is a discussion on these approximations.

The real gas model used in this work takes the form of property tables generated by NIST 14 [10]. This code is a compilation of experimental data on gas properties developed by the National Institute of Standards and Technology. This data allows total enthalpy to be evaluated directly from total temperature and pressure.

The next lower level of complexity is the ideal gas model. This model neglects property variation due to changes in pressure. In many cases, especially at low pressure and high temperature, pressure dependence is weak and this assumption is very reasonable. In terms of Equation 4.12, this permits neglect of the second integral. Total enthalpy change may then be expressed in terms of specific heat and total temperature:

$$h_{T4} - h_{T5} = \int_{T_{T5}}^{T_{T4}} C_P(T)\, dT_T \tag{4.13}$$

Note, however, that specific heat is a function of static temperature, thus, its variation between states four and five must be known to evaluate this integral. This turns out to be a complication not avoided by ideal gas assumptions and the integral must be approximated in some way.

In order to approximate this integral, assumptions about the variation of specific heat with temperature are typically made. Ideal gas Equations 1.4 and 1.5 make use of expressions from Shapiro [1]. Although he does not include the full derivation, he does cite one assumption of this variety:

$$\int_{T_{T5}}^{T_{T4}} C_P(T)\, dT_T \approx \frac{C_{P4} + C_{P5}}{2} \cdot (T_{T4} - T_{T5}) \tag{4.14}$$

This calculation only requires knowledge of specific heat at the initial and final static temperatures, not its variation over the entire temperature range. This is reasonable over a moderate temperature range as pointed out by Shapiro. Perfect gas Equations 1.7 and 1.8 make exclusive use of this assumption. This results in cancellation of specific heat from

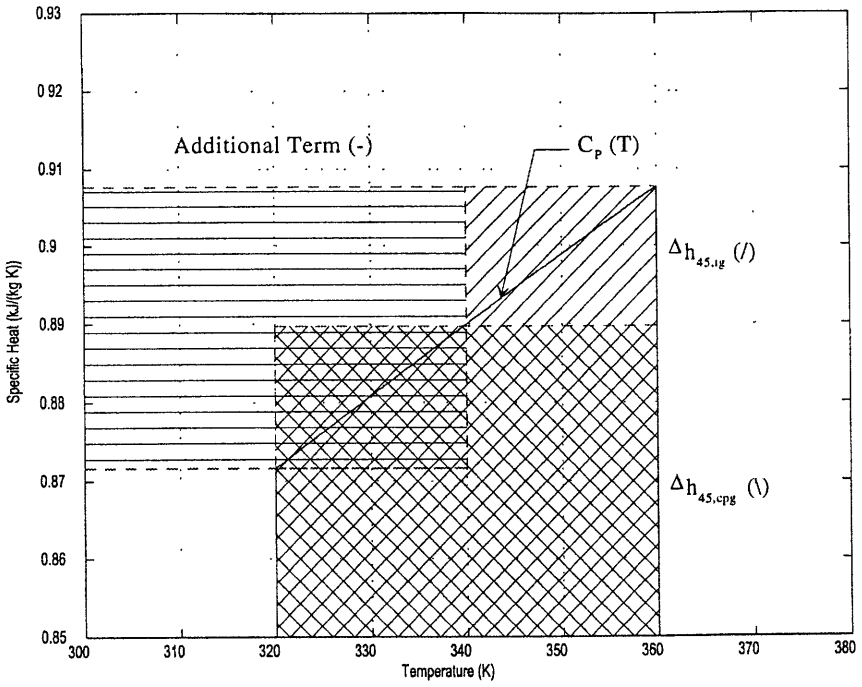

Figure 4-1: Integration of Specific Heat for Enthalpy Evaluation

the numerator and denominator and efficiency may be expressed only in terms of total temperature and pressure ratio and specific heat.

Figure 4-1 graphically represents the integration of Equation 4.13 assuming ideal and calorically perfect gas behavior. Shown is the actual variation of specific heat of CO_2 at constant atmospheric pressure over a range of temperatures typical of the Blowdown Turbine. This variation is calculated using NIST 14. Integration of this quantity assuming ideal gas behavior is represented by Equation 1.4 based on Shapiro's derivation. The first two terms in this equation produce the sum of all hatched regions in Figure 4-1[2]. The last term subtracts the horizontally hatched region labeled *Additional Term*. This leaves the forward hatched region labeled $\Delta h_{45,ig}$ as the ideal gas approximation of the integral in Equation 4.13. Assuming calorically perfect gas behavior and referring to Equation 1.7, however, specific heat is held constant and the integral in Equation 4.13 is approximated

[2]Realize that the integrals (hatched regions) extend down and over to the T and C_P axes.

by the backward hatched region in Figure 4-1 labeled $\Delta h_{45,cpg}$.

As seen from Figure 4-1, over the typical range of Blowdown Turbine operating temperatures and at constant atmospheric pressure, specific heat is very close to linear with temperature and varies approximately 5%. If the relationship was exactly linear, the ideal and calorically perfect gas integrations of specific heat would be identical. As is, they should be very similar. This means efficiency predictions from both models should also be very similar assuming pressure variation does not significantly affect these results. This will be seen in the next section where efficiency calculations take stage.

4.4 Efficiency Calculation

Section 1.2 provides the framework for calculating efficiency using real gas properties and by assuming ideal and calorically perfect gas behavior. In all cases, gas properties including total enthalpy and specific heat are required. These properties are contained in tables versus static temperature and pressure generated using NIST 14 [10]. This section discusses the process used to determine the required flow properties and their use in aerodynamic efficiency calculations. The results from all experiments are presented in Appendix B.

Figure 4-2 shows, on an enthalpy-entropy diagram, where flow properties are evaluated. Quantities known from experimental data are shown in **bold** face and those evaluated, in normal face. Upstream total enthalpy, required to calculate efficiency, and upstream entropy, required to iterate for downstream isentropic total temperature (enthalpy), are interpolated directly from the property tables using upstream total conditions. Upstream dynamic pressure is typically 0.5% of measured upstream total pressure meaning the upstream Mach number is very low and total and static conditions are essentially interchangeable [5]. For this reason, upstream specific heat, for use in calculating efficiency assuming ideal and calorically perfect gas behavior, is also interpolated directly from total conditions. Downstream, the Mach number is significantly higher, however, and this approximation is not valid.

Once all upstream conditions are known, downstream total enthalpy and entropy are

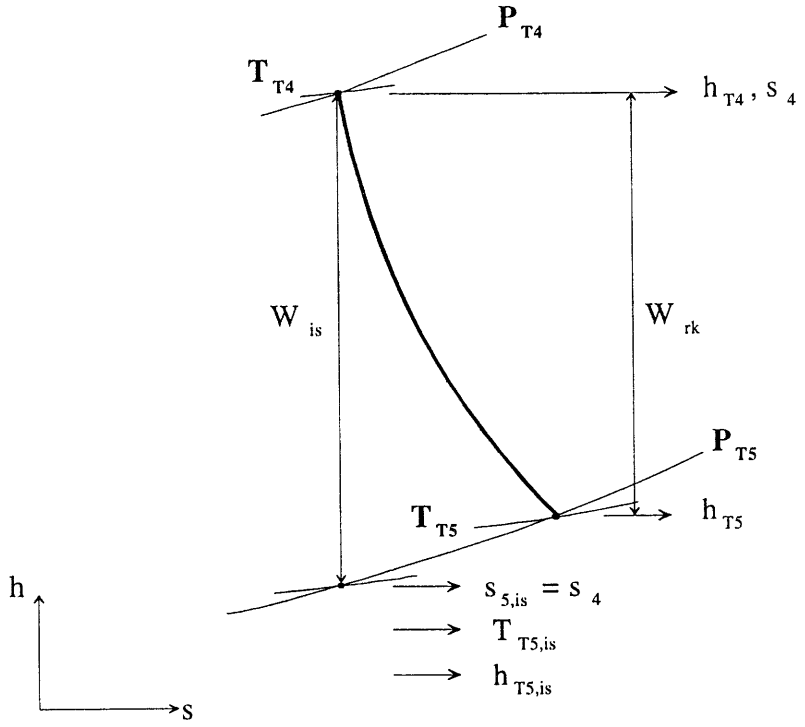

Figure 4-2: Enthalpy-Entropy Diagram Showing Evaluation of Gas Properties for Efficiency Calculations

interpolated similarly. Interpolation of specific heat, however, requires static temperature and pressure as the Mach number in this region is significantly higher than upstream. Static pressure is known and static temperature is iterated using the following expression:

$$T_5{}^* = \frac{T_{T5}}{\frac{P_{T5}}{P_5}^{\frac{R_{CO_2}}{C_{P5}{}^*}}} \tag{4.15}$$

where * indicates iteration.

With all upstream and downstream conditions known, only the ideal expansion total enthalpy is required for efficiency calculations. This enthalpy is interpolated using the downstream isentropic total temperature, or that temperature which produces an entropy equal to the upstream value.

Once all conditions are known, efficiency may be calculated as described in Section 1.2.

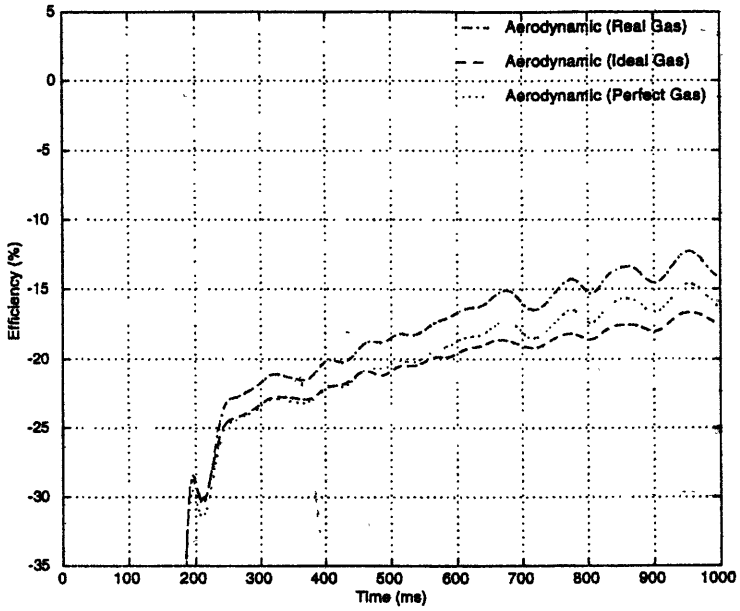

Figure 4-3: Experiment 024 Aerodynamic Rake Efficiency

Figure 4-3 shows these calculations for experiment 024, a simulation of the full-scale turbine design point at minimum tip clearance. Here, efficiency is referenced to the Craig and Cox empirical efficiency estimate at the smaller rotor tip clearance presented in Section 6.3.2. This presentation of efficiency is intended to conceal proprietary information. Numerous characteristics of this figure deserve special attention and these are where focus now shifts.

First, the efficiency predictions are very similar both in shape and magnitude. The real gas calculation, presumed to be most accurate, is consistently $2 - 3\%$ greater than the ideal gas calculation. The perfect gas calculation lies mid-way between the real and ideal gas calculations. This trend is not expected. In neglecting property variations due to pressure change, the ideal gas prediction should deviate somewhat from the real gas calculation. Further neglecting changes in specific heat, the perfect gas prediction should deviate even further. The reversal of ideal and perfect gas predictions, however, departs from this reasoning. This trend, which is reasonably consistent between experiments, is not understood.

Second, the efficiency predictions are not constant in the region of similarity. As seen in Appendix A, Reynolds number is never constant and equal to design, however, its variation is small in terms of significantly affecting performance calculations. The trend in corrected speed is similar. It is generally constant and equal to design up to 1000 ms within $5-7\%$. The remaining non-dimensional similarity parameters are relatively constant in the region of $300-1000$ ms. This suggests similarity may be reasonably assumed up to 1000 ms into the experiment. As seen in Figure 4-3, efficiency predictions increase up to near 800 ms; it is only between $800-1000$ ms that they are moderately constant. This is, however, an encouraging feature of the aerodynamic efficiency measurement as it demonstrates measurement resolution. During the experiment, upstream total temperature and pressure decrease as the supply tank empties causing the simulated operating point to "travel" slightly in time. This, in turn, causes drift in expected efficiency. On the other hand, this presents a problem in assigning a single value of efficiency for each experiment. Because similarity is feasible up to 1000 ms, however, it is not thought irrational to concentrate on this latter period of time. Therefore, single value aerodynamic efficiencies presented in the remainder of this work will reflect this period of efficiency prediction.

Another obvious characteristic of the efficiency predictions in Figure 4-3 is the low frequency content of magnitude $2-3\%$. This is reminiscent of Section 3.6 where nozzle wake measurements were discussed. A quick calculation verifies that this frequency is very near the frequency observed in the downstream total temperature and pressure traces presented in Section 3.6. Furthermore, the magnitude of these variations in percent is very near the magnitude of the total temperature variations in degrees Kelvin. These total temperature and pressure sinusoidal variations simply filter down through enthalpy calculations and appear in efficiency. If they were overlaid, it would be seen that they are 180° out of phase. Inside a nozzle wake, temperature is reduced due to heat transfer to the nozzle. In terms of efficiency, this is seen as a lower temperature ratio for the same pressure ratio, or, a greater work extraction. This produces efficiency peaks over total temperature troughs. This further complicates assigning a single value of efficiency for a given experiment. The solution will be to average this sinusoidal variation.

The final observation to be made from Figure 4-3 is the label, "Experiment 024 Aerodynamic *Rake* Efficiency." *Rake* refers to the efficiency based on measured total temperature and pressure. It is not the adiabatic efficiency because of the transient nature of the experiment. The test is of sufficiently short duration that the turbine stage does not reach thermal equilibrium. A correction for the heat transfer must therefore be applied to estimate *adiabatic* efficiency. This correction is the topic of the next section.

4.5 Heat Transfer Correction

Referring back to Figure 1-1, turbine adiabatic work is labeled W_{ad}. This work is required in calculating turbine adiabatic efficiency from Equation 1.1. This is not the work calculated from blowdown experimental data as described in the previous section however. This calculation, labeled W_{rk} in Figure 1-1, includes heat transferred from the flow to the turbine as can be seen by rearranging the first law of thermodynamics as stated in Equation 4.11:

$$\delta h_T = \delta w - \delta q \tag{4.16}$$

In the previous section it was assumed that there was no heat transfer so that work could be expressed as a change in total enthalpy. Because of the transient nature of the blowdown experiment, however, heat is transferred from the flow to the turbine. By Equation 4.16, written as a statement of *flow* energy, δq is negative and turbine work is less than the change in total enthalpy. Rake efficiency predictions uncorrected for heat transfer will thus overestimate actual turbine performance. The purpose of this section is to quantify the required heat transfer correction to rake efficiency.

According to Shang, the difference between the adiabatic and measured exit total enthalpies is generally not equal to the heat transferred from the flow to the turbine [11]. This is a result of the path dependent heat transfer process. To relate these enthalpies and heat transfer quantity it is assumed that the heat transfer takes place at an equivalent temperature T^* and the entropy generated is reversible. Then, according to Cai [4]:

$$h_{T5,ad} - h_{T5} = Q\left(\frac{T_5}{T^*}\right), Q \geq 0 \tag{4.17}$$

Adiabatic efficiency is then related to rake efficiency and heat transfer by the expression:

$$\eta_{ad} = \eta_{rk} - \frac{Q}{h_{T4} - h_{T5,is}}\left(\frac{T_5}{T^*}\right) = \eta_{rk} + \Delta\eta_{rk,ht} \tag{4.18}$$

also from Cai [4]. The temperature T^* is unknown. In reality, heat is transferred from the flow to the turbine at different temperatures throughout the facility. In calculating the resulting entropy generation, however, it is convenient to assume an equivalent temperature. For the purpose of this analysis, T^* will be assumed to equal the average of the inlet total and exit static temperatures at 400 ms. This is the earliest time at which both aerodynamic and mechanical efficiency predictions are valid and according to Guenette, these are the most narrow bounds able to be assigned to this equivalent temperature [12]. This provides a procedure for correcting aerodynamic rake efficiency measurements given the value of $\Delta\eta_{rk,ht}$. The task is now to determine this value.

Many methods have been proposed to estimate the heat transfer during a blowdown experiment. As explained by Guenette, measurements of turbine work by aerodynamic and mechanical approaches may be compared and heat transfer inferred [12]. This is possible because mechanical measurements of turbine work are influenced much less by heat transfer than are aerodynamic measurements[3]. This heat transfer may also be determined by numerical computation. A one-dimensional compressible flow analysis utilizing Reynolds' analogy or a two-dimensional flow analysis with heat transfer may be employed [12]. Alternatively, this heat transfer may be determined experimentally by direct measurement [12]. The approach taken here, however, is to compare rake efficiency measurements between experiments simulating the same full-scale turbine operating point, but at different inlet temperatures. This will allow direct determination of $\Delta\eta_{rk,ht}$ for a given inlet temperature.

Table 4.2 summarizes the experiments compared in determining the rake efficiency cor-

[3]This will be shown in Section 5.4.

Table 4.2: Experiments Compared to Determine Rake Efficiency Heat Transfer Correction

Experiment	034	038	039
π_t	95.8%	96.0%	96.0%
N_{cor}	103.2%	101.7%	105.4%
R_e	107.7%	104.7%	106.1%
γ_4	99.9%	100.8%	100.3%
P_{T4} $(psia)$	104.5	94.7	100.4
T_{T4} $(^\circ F)$	220	175	200

rection for heat transfer. Experiments 034, 038, and 039 all simulate near full-scale turbine Reynolds number, corrected speed, and pressure ratio, each at a different inlet total temperature[4]. The same full-scale turbine operating point is simulated in each case, thus, adiabatic efficiency should remain constant. Because the inlet temperature varies, however, different levels of heat transfer occur causing different levels of rake efficiency overprediction by Equation 4.18. The lowest temperature experiment, 038, should predict the lowest rake efficiency followed by 039 and 034. The result of this comparison should be $\Delta\eta_{rk,ht}$ versus inlet total temperature.

Figure 4-4 shows the difference between adiabatic and predicted rake efficiencies for these experiments; this is exactly $\Delta\eta_{rk,ht}$. As expected, all experiments overpredict adiabatic efficiency as $\Delta\eta_{rk,ht}$ is less than zero for each experiment. In addition, the lowest inlet temperature experiment, 038, predicts the lowest rake efficiency, requiring the smallest correction, and as inlet temperature increases, so does the predicted rake efficiency and required absolute correction. Because these experiments simulate the same full-scale turbine operating point as shown in Table 4.2, this change in rake efficiency with inlet temperature is entirely due to increasing levels of heat transfer. This assumes, of course, the error associated with the repeatability of rake efficiency prediction is much less than the shown change in rake efficiency due to heat transfer. This is in fact the case. Unfortunately, the heat transfer correction determined from a change in efficiency will have its precision

[4]Design specific heat ratio can not be simultaneously simulated at temperatures other than that calculated in Section 2.4, however, the resulting deviation is very small as seen in Table 4.2.

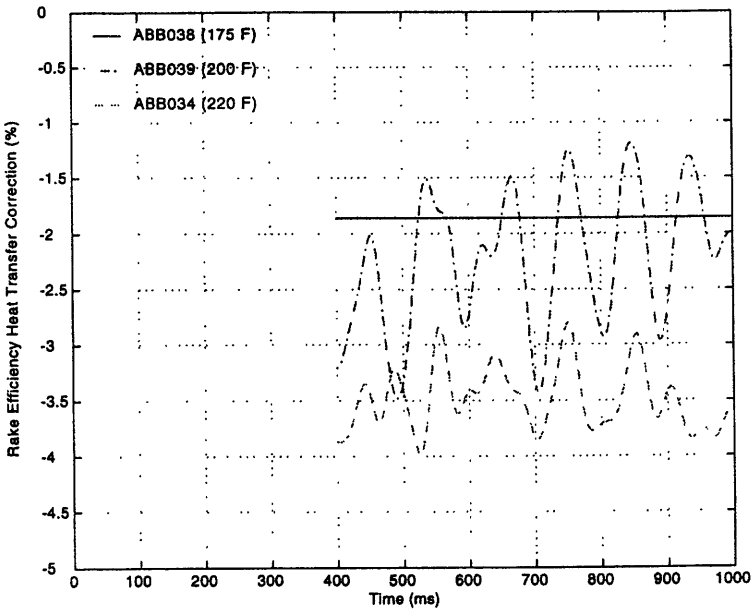

Figure 4-4: Rake Efficiency Correction for Heat Transfer

index magnified due to the limited repeatability of each efficiency prediction. The resulting uncertainty in this correction as well as in aerodynamic adiabatic efficiency will be discussed in the next section.

How is adiabatic efficiency determined allowing determination of these corrections? Keogh, in a pre-test analysis of mechanical adiabatic efficiency measurement, estimates the magnitude of the heat transfer at an inlet temperature of $170°F$ to be approximately 2.00% of the ideal total enthalpy drop across the turbine stage [3]. Assuming this heat transfer takes place at a temperature T^* as previously explained, this corresponds to a value of $\Delta\eta_{rk,ht,170°F}$ of approximately -1.86%. Because the conditions for this estimate are very near the inlet conditions of experiment 038, it is assumed as a control experiment that 038 overpredicts adiabatic efficiency by exactly 1.86%. Relative changes in rake efficiency between experiments 038 and 039 and experiments 038 and 034 are then determined by subtracting their rake efficiency predictions. Experiment 039, conducted at an inlet temperature of $200°F$, thus overpredicts adiabatic efficiency by approximately 2.23%

Table 4.3: Aerodynamic Rake Efficiency Heat Transfer Correction Summary

Experiment	034	038	039
$T_{T4}\,(^\circ F)$	220	175	200
$T^*\,(^\circ F)$	134	104	120
$\frac{Q}{h_{T4}-h_{T5,is}}$	3.75%	2.00%	2.40%
$\Delta\eta_{rk,ht}$	−3.49%	−1.86%	−2.23%

and experiment 034, at an inlet temperature of $220^\circ F$, by approximately 3.49%. Table 4.3 summarizes the aerodynamic rake efficiency heat transfer corrections.

4.6 Post-Test Efficiency Uncertainty Analysis

According to the pre-test uncertainty analysis presented in Section 4.2, the absolute uncertainty in aerodynamic adiabatic efficiency prediction is estimated to be 0.61% from instrument calibration data. The repeatability of this prediction is estimated to be approximately 0.49%. Because bias errors remain unknown, the estimated absolute uncertainty can not be verified from experimental data. The actual repeatability of this prediction may be determined, however, and compared to the pre-test estimate. That is the purpose of this section.

Experiments 025 and 026 are near exact duplicates meant to test the repeatability of efficiency measurement. Table 4.4 summarizes these experiments and their aerodynamic rake efficiency predictions, precision indices, and repeatabilities. Also included are these statistics for the heat transfer correction determined in the previous section as well as for aerodynamic adiabatic efficiency.

For a small number of samples, two in this case, the precision index is defined as follows [7]:

$$S = \frac{\bar{R}}{d_2{}^*} \tag{4.19}$$

where $\bar{R}$ represents the average data scatter and $d_2{}^*$ accounts for the number of sample

Table 4.4: Post-Test Efficiency Uncertainty Analysis Summary

	025	026	C_*	$S_*/*$	t_{95}	$U_{95,rel}$
π_t	95.6%	95.8%	-	-	-	-
N_{cor}	102.8%	102.0%	-	-	-	-
R_e	106.7%	110.7%	-	-	-	-
γ_4	99.9%	100.8%	-	-	-	-
$\eta_{rk,rg}$	−13.12%	−13.53%	-	0.38%	2.00	0.65%
$\eta_{rk,ig}$	−16.80%	−17.12%	-	0.31%	2.00	0.60%
$\eta_{rk,cpg}$	−15.32%	−15.71%	1.04	0.37%	2.00	0.61%
$\Delta\eta_{rk,ht,220°F}$	−3.49%	−3.49%	0.04	29.05%	2.00	2.03%
$\eta_{ad,cpg}$	−18.77%	−19.16%	-	1.34%	2.00	2.12%

degrees of freedom. A value of 1.28 is used for d_2^* in this case [7]. This data shows that aerodynamic rake efficiency may be measured with repeatability between 0.60% and 0.65% depending on the gas model employed.

Table 4.4 also summarizes the uncertainty in correcting rake efficiency predictions for heat transfer. As explained in the previous section, the required heat transfer correction is determined by comparing experiments simulating the same full-scale turbine operating point, but at different inlet temperatures. By this method, the precision index of the resulting heat transfer correction is magnified due to the limited repeatability of each efficiency prediction used to calculate it. The result is a 2.03% relative uncertainty in the estimated 3.49% heat transfer correction. And when this correction is applied to perfect gas rake efficiency prediction[5], the relative uncertainty in adiabatic efficiency becomes 2.12%. There is also a heat transfer correction bias associated with the equivalent temperature assumption and heat load estimates. Because only relative uncertainties are being examined here, however, this bias does not affect the results.

This analysis shows that aerodynamic rake efficiency may be measured with relative uncertainty between 0.60% and 0.65%. This uncertainty is near that estimated in the pre-test analysis for aerodynamic adiabatic efficiency. When these rake efficiency predictions

[5]The correction is applied to the perfect gas calculation to allow direct comparison to the pre-test uncertainty analysis.

are corrected for heat transfer, however, the relative uncertainty in adiabatic efficiency becomes approximately 2.12%. This uncertainty is much higher than pre-test estimates and does not come close to meeting the uncertainty objectives of this work. The reason for this shortfall is the method used to estimate the required heat transfer correction. By comparing experiments simulating the same operating point but at different inlet temperatures, the change in rake efficiency due to heat transfer is readily available. The uncertainty of this correction, however, is subject to the repeatability of the rake efficiency predictions. The result is a correction uncertainty over 50% of the magnitude of the correction itself. This significantly increases the relative uncertainty of the adiabatic efficiency prediction determined from this correction. The solution to this problem is to determine the required heat transfer correction by analysis rather than experimental data. While this is likely to reduce precision errors in this correction it has the potential to increase bias errors and this may or may not by easily estimated with required accuracy. This analysis thus concludes that mostly due to the difficulty in estimating heat transfer, the aerodynamic approach to measuring turbine adiabatic efficiency does not produce absolute or relative uncertainties consistent with the objectives of this work. It remains to be seen in the next chapter whether or not the mechanical approach will be successful in meeting these objectives.

4.7 Chapter Summary

This chapter has discussed turbine aerodynamic efficiency measurement. The discussion began with a pre-test efficiency uncertainty analysis. The objective of this analysis was to uncover significant sources of uncertainty in the calculation of efficiency and estimate the expected absolute and relative uncertainties in efficiency calculation. It was determined that total temperature is the key measurement in calculating efficiency by the aerodynamic approach in terms of uncertainty due to the large total temperature ratio influence coefficient. Absolute and relative uncertainties were estimated to be 0.61% and 0.49% respectively.

This discussion was followed by a comparison of real and ideal gas models in terms of the approximations they use in calculating turbine work. This comparison was meant

to explore the use of ideal gas assumptions in characterizing turbine performance. It was shown that over the temperature range of operation of the Blowdown Turbine, specific heat variation with temperature is near linear and ideal gas calculations should agree reasonably with real gas calculations.

The next topic of discussion was efficiency calculation from experimental data. This included efficiency predictions from experiment 024 showing an approximate $2-3\%$ deviation between real and ideal gas calculations. This baseline experiment produced near constant rake efficiencies of -14%[6] to -18%[6] between $800-1000\ ms$.

This was followed by an analysis of efficiency prediction to determined the required aerodynamic rake efficiency heat transfer correction. It was shown that at an inlet temperature of $220°F$, aerodynamic rake efficiency must be corrected by approximately -3.49% to account for heat transfer effects.

This chapter concludes with a post-test efficiency uncertainty analysis intended to determine adiabatic efficiency measurement relative uncertainty and verify the pre-test estimate. It was shown that rake efficiency predictions are repeatable within 0.60% to 0.65% depending on the gas model used. The relative uncertainty in the heat transfer correction was determined to be 2.03%, however, as the correction was determined by comparing rake efficiency predictions. This resulted in an aerodynamic adiabatic efficiency relative uncertainty of 2.12%, much higher than the 0.49% pre-test estimate. It was finally concluded that the aerodynamic approach is not capable of precise adiabatic efficiency measurement. This is primarily a result of the approach's sensitivity to non-adiabatic effects and the difficulty in estimating them.

[6]Efficiency is referenced to the Craig and Cox empirical efficiency estimate at the smaller rotor tip clearance discussed in Section 6.3.2.

Chapter 5

Mechanical Measurement of Adiabatic Efficiency

5.1 Introduction

This chapter discusses measurement of turbine adiabatic efficiency using the mechanical approach described in Section 1.2. This approach will determine turbine adiabatic efficiency from turbine torque, speed, and mass flow as well as upstream and downstream total temperature and pressure measurements.

The discussion begins with a pre-test efficiency uncertainty analysis. This analysis, intended to estimate the expected uncertainty in mechanical adiabatic efficiency measurement, follows directly from the analysis presented in Section 4.2 and is based on the uncertainty analysis method outlined in Reference [7]. This analysis is followed by a discussion on the actual efficiency calculation. This includes transient corrections accounting for rotor acceleration and tunnel mass storage and presentation of efficiency calculations for experiment 024, a baseline full-scale turbine design point simulation. The next section will investigate the effect of heat transfer on mechanical efficiency measurement. This is followed by a discussion on additional processes thought to affect this measurement but who are not yet accounted for and thought to be of second order. This chapter will conclude with a post-

test efficiency uncertainty analysis focusing on the repeatability of mechanical efficiency measurement.

5.2 Pre-Test Efficiency Uncertainty Analysis

As discussed in Section 4.2, uncertainty consists of random error, represented by precision index S, and fixed error, represented by bias B. Both are expressed in terms of a Taylor series expansion and involve influence coefficients. Again, assuming perfect gas behavior for algebraic simplicity, mechanical adiabatic efficiency may be written as:

$$\eta_{ad,brk,perf} = \frac{\mathcal{T} \cdot \omega}{\dot{m}_t \bar{C}_P T_{T4} \left(1 - \pi_t^{\frac{R_{CO_2}}{\bar{C}_P}}\right)} \tag{5.1}$$

Efficiency precision index and bias then become:

$$\frac{S_{\eta_{ad,brk,cpg}}}{\eta_{ad,mech,cpg}} = \sqrt{\left(C_{\mathcal{T}} \cdot \frac{S_{\mathcal{T}}}{\mathcal{T}}\right)^2 + \left(C_{\dot{m}_t} \cdot \frac{S_{\dot{m}_t}}{\dot{m}_t}\right)^2 + \left(C_{\bar{C}_P} \cdot \frac{S_{\bar{C}_P}}{\bar{C}_P}\right)^2 + \cdots + \left(C_{T_{T4}} \cdot \frac{S_{T_{T4}}}{T_{T4}}\right)^2 + \left(C_{\pi_t} \cdot \frac{S_{\pi_t}}{\pi_t}\right)^2} \tag{5.2}$$

$$\frac{B_{\eta_{ad,brk,cpg}}}{\eta_{ad,brk,cpg}} = \sqrt{\left(C_{\mathcal{T}} \cdot \frac{B_{\mathcal{T}}}{\mathcal{T}}\right)^2 + \left(C_{\dot{m}_t} \cdot \frac{B_{\dot{m}_t}}{\dot{m}_t}\right)^2 + \left(C_{\bar{C}_P} \cdot \frac{B_{\bar{C}_P}}{\bar{C}_P}\right)^2 + \cdots + \left(C_{T_{T4}} \cdot \frac{B_{T_{T4}}}{T_{T4}}\right)^2 + \left(C_{\pi_t} \cdot \frac{B_{\pi_t}}{\pi_t}\right)^2} \tag{5.3}$$

where uncertainties in rotor speed, ω, and gas constant, R_{CO_2}, have been neglected. The influence coefficients, C_*, come from direct differentiation of Equation 5.1. Ignoring their sign, these expressions as derived by Keogh are [3]:

$$C_{\mathcal{T}} = C_{\dot{m}_t} = C_{T_{T4}} = 1 \tag{5.4}$$

Table 5.1: Pre-Test Efficiency Uncertainty Analysis Summary

Measurement	Nominal	C_*	$S_*/*$	$B_*/*$	t_{95}	$U_{95,abs}$	$U_{95,rel}$
$\mathcal{T}\,(\mathcal{N}\cdot m)$	1992.00	1.00	0.13%	0.10%	2.00	0.28%	0.26%
$\omega\,(RPS)$	87.08	-	-	-	-	-	-
$\dot{m}_t\left(\frac{kg}{s}\right)$	25.00	1.00	0.13%	0.33%	2.00	0.42%	0.26%
$\bar{C}_P\left(\frac{J}{kg\cdot K}\right)$	866.06	0.08	-	0.20%	2.00	0.20%	-
$T_{T4}\,(K)$	378.00	1.00	0.03%	0.02%	2.00	0.06%	0.06%
π_t	0.48	1.26	0.07%	0.25%	2.00	0.29%	0.14%
$R_{CO_2}\left(\frac{J}{kg\cdot K}\right)$	188.92	-	-	-	-	-	-
$\eta_{ad,brk,cpg}$	90%	-	0.21%	0.47%	2.00	0.56%	0.37%

$$C_{\bar{C}_P} = 1 + ln\,(\pi_t)\cdot\frac{\pi_t^{\frac{R_{CO_2}}{\bar{C}_P}}\cdot R_{CO_2}}{\bar{C}_P\cdot\left(1-\pi_t^{\frac{R_{CO_2}}{\bar{C}_P}}\right)} \tag{5.5}$$

$$C_{\pi_t} = \frac{\pi_t^{\frac{R_{CO_2}}{\bar{C}_P}}\cdot R_{CO_2}}{\bar{C}_P\cdot\left(1-\pi_t^{\frac{R_{CO_2}}{\bar{C}_P}}\right)} \tag{5.6}$$

Table 5.1 summarizes the pre-test mechanical efficiency uncertainty analysis. Nominal values of those measurements in Equation 5.1 contributing to efficiency are included. These are determined from design point calculations and experiments prior to those examined in this work. Precision indices and biases for torque and mass flow are taken from calibration data analyses by Keogh [3]. These uncertainty components for total temperature and pressure ratio come from similar analyses by Cai [4]. As in Section 4.2, a constant bias of 0.20% is assumed to account for errors in determining the specific heat of CO_2 as suggested by Friend [8]. Finally, uncertainty is calculated as in Section 4.2, Equation 4.9, again assuming a value of 2.00 for t_{95}.

From this analysis, the estimated absolute uncertainty in mechanical adiabatic efficiency measurement is 0.56%. This is very close to the 0.61% pre-test estimate of aerodynamic adiabatic efficiency absolute uncertainty from Section 4.2. In this case, however, a larger

percentage of absolute uncertainty is due to fixed bias error. The precision index for mechanical efficiency measurement is approximately 0.19%[1]. By Equation 4.9, this corresponds to a relative uncertainty of approximately 0.37%. This is slightly lower than the 0.49% pre-test estimate of aerodynamic adiabatic efficiency relative uncertainty and much less than the post-test 2.12% estimate. This indicates the mechanical efficiency measurement, although containing approximately the same absolute uncertainty, will be more repeatable than the aerodynamic efficiency measurement. More discussion on this conclusion will follow the post-test mechanical efficiency uncertainty analysis presented in Section 5.6.

5.3 Efficiency Calculation

5.3.1 Introduction

This section will describe the calculation of efficiency using the mechanical approach as outlined in Section 1.2. Necessary corrections to this approach accounting for rotor acceleration and tunnel mass storage will be discussed. Reference will also be made to Section 4.4 concerning determination of flow properties required for this calculation. The section will end with the presentation of efficiency calculations for experiment 024, a baseline full-scale turbine design point simulation. This is the same experiment used in Section 4.4 to first present aerodynamic rake efficiency calculations.

Section 4.3 discusses real versus ideal gas models for calculation of turbine work. It shows that over the range of temperatures encountered in the Blowdown Turbine, these models should produce similar results. This is verified by comparison of efficiency calculations from each model in Section 4.4. For this reason and because the real gas model is presumed to be most accurate, ideal turbine work for use in mechanical efficiency calculations will be determined assuming real gas behavior. Mechanical efficiency may then be expressed as:

$$\eta_{brk} = \frac{\mathcal{T} \cdot \omega}{\dot{m}_t \left(h_{T4} - h_{T5,is} \right)} \tag{5.7}$$

[1]Refer to Equation 4.10.

This expression neglects important transient effects of the Blowdown Turbine environment however. Most importantly, it assumes a constant rotor rotational speed. During a blowdown experiment, mechanical speed varies in time and this must be taken into account. Furthermore, the mass flow required for this calculation may deviate significantly from that directly measured from the venturi nozzle. This too must be accounted for. The following two subsections discuss these corrections.

5.3.2 Power Correction

Thus far, power has been expressed as the product of turbine torque and speed. But, this simple expression neglects rotor acceleration. To correct for this transient effect, an additional term must be added to the power expression; the result is:

$$\mathcal{P} = \mathcal{T} \cdot \omega + I \cdot \frac{d\omega}{dt} \cdot \omega \tag{5.8}$$

where I is the moment of inertia of all rotating parts. These parts include the rotor discs and blades, the shaft, and the eddy current brake drum. This inertia was measured experimentally by so called brake tests. A brake test is identical to a blowdown experiment except the supply tank is not pressurized and the fast-acting valve is not armed. In this case, the turbine produces zero power and inertia may be found from Equation 5.8 as turbine torque and speed are measured and acceleration calculated. From numerous brake tests at different speeds and brake settings, the inertia was found to be 1.8085 $kg \cdot m^2$ with standard deviation 0.13%. This work is discussed in more detail by Keogh [3].

Figure 5-1 shows raw and corrected power for experiment 024 displaying the effect of this power correction. Both traces have been passed through a Butterworth lowpass filter with cutoff frequency approximately 25 Hz. Before approximately 300 ms, the rotor is accelerating and corrected power exceeds uncorrected. Beyond 300 ms, the rotor is decelerated by the eddy current brake in order to hold corrected speed constant as inlet temperature decreases. This deceleration accounts for as much as a 10% decrease in turbine power between $300 - 1600$ ms.

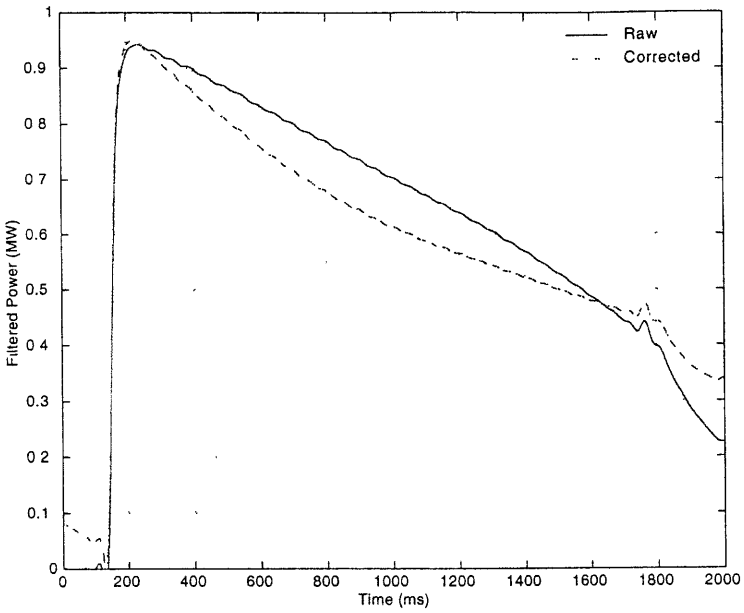

Figure 5-1: Turbine Power Correction for Rotor Acceleration

5.3.3 Tunnel Mass Storage Correction

The purpose of the critical-flow venturi is to measure turbine mass flow. This measurement, however, is taken at the nozzle throat located inside the dump tank whereas the measurement of interest is through the turbine stage. These measurements may differ because of the volume separating the turbine stage and nozzle throat. Density variations in these regions will result in mass storage. Turbine and nozzle mass flows are then related by the following expression:

$$\dot{m}_t = \dot{m}_n + \frac{\partial M_s}{\partial t} \tag{5.9}$$

Stored mass flow must then be estimated to determine turbine mass flow from venturi measurements.

To estimate stored mass flow, the equation of state incorporating compressibility factor is written in terms of mass:

$$M_s = \frac{P}{T}\frac{V}{R_{CO_2} Z} \tag{5.10}$$

This expression is then differentiated in time:

$$\frac{\partial M_s}{\partial t} = \frac{V}{R_{CO_2} Z}\left(\frac{1}{T}\right)\frac{\partial P}{\partial t} - \frac{V}{R_{CO_2} Z}\left(\frac{P}{T^2}\right)\frac{\partial T}{\partial t} \tag{5.11}$$

This expression represents stored mass flow and must be evaluated in time for each volume separating the turbine stage and nozzle throat. To assist in this task various thermocouples and pressure probes are located in the diffuser separating the test section and dump tank. Many other volumes, however, are not accessible to flow measurement. In addition, the accuracy at which many can be calculated is limited. For these reasons a transient model of the blowdown facility was used in developing this stored mass flow correction. This model allows estimation of flow properties at various tunnel locations and is the same model utilized in assessing the effect of an additional choke point downstream of the throttle exhaust. A detailed analysis of stored mass flow including results from this transient blowdown model are available in Reference [3]. Here, this correction will simply be applied and its effect on nozzle mass flow presented.

Figure 5-2 shows nozzle and turbine mass flows labeled *Uncorrected* and *Mass Correction* respectively. These measurements differ by the mass flow stored in the volume separating the two measurement locations. This correction is valid between approximately $400 - 1000\ ms$. As seen, between approximately $400 - 650\ ms$, mass is stored in the diffuser separating the turbine and nozzle and turbine mass flow is higher than nozzle mass flow. This trend reverses at approximately $650\ ms$ after which time turbine mass flow is less than that through the venturi nozzle.

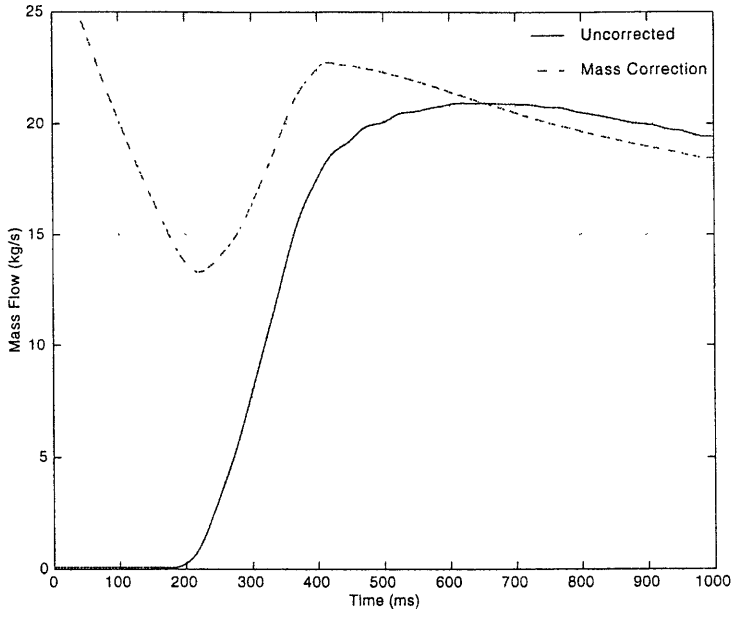

Figure 5-2: Turbine Mass Flow Correction for Tunnel Mass Storage

5.3.4 Corrected Efficiency Calculation

Once turbine power and mass flow have been corrected for rotor acceleration and tunnel mass storage, mechanical efficiency[2] may be expressed as:

$$\eta_{lbrk} = \frac{\mathcal{T} \cdot \omega + I \cdot \frac{d\omega}{dt} \cdot \omega}{\left(\dot{m}_n + \frac{\partial M_s}{\partial t}\right)\left(h_{T4} - h_{T5,is}\right)} \tag{5.12}$$

Figure 5-3 shows this calculation for experiment 024. Overlaid are aerodynamic rake efficiency calculations first presented in Section 4.4.

As seen in Figure 5-3, the mechanical approach predicts efficiency near -7%[3] for the baseline full-scale turbine design point simulation. This is considerably higher than the aerodynamic efficiency predictions. The mechanical prediction is also very near constant

[2]Transient heat transfer is still to be corrected. This correction, discussed in the next section, is much smaller than that required for aerodynamic rake efficiency however.

[3]This value is referenced to the Craig and Cox empirical efficiency estimate at the smaller rotor tip clearance presented in Section 6.3.2.

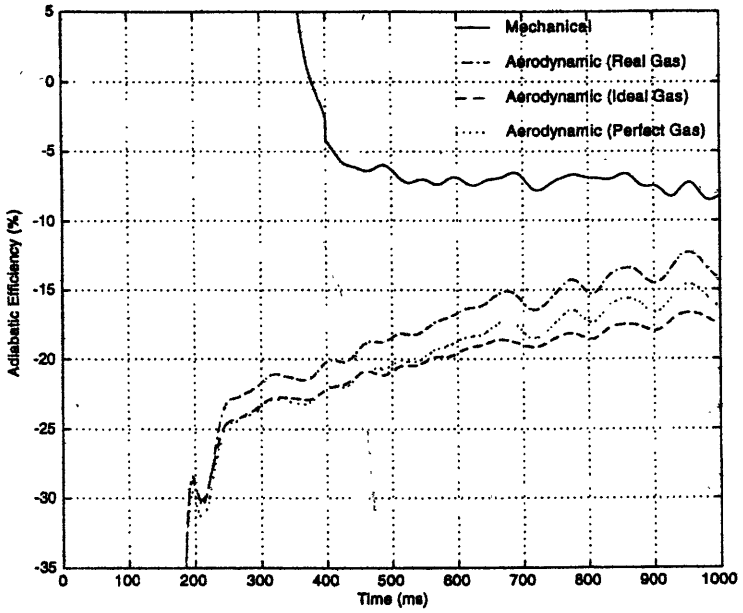

Figure 5-3: Experiment 024 Mechanical and Aerodynamic Rake Efficiencies

between $400 - 1000\ ms$. Aerodynamic and mechanical adiabatic efficiency predictions, those corrected for heat transfer as described in Sections 4.5 and 5.4, are presented for each experiment in Appendix B.

5.4 Heat Transfer Correction

As shown in Section 4.5, heat transfer from the flow to the turbine during a blowdown experiment causes overprediction of adiabatic efficiency using the aerodynamic approach. This is because this approach determines turbine work from the drop in total enthalpy across the turbine stage. By this calculation, work extracted from the flow can not be distinguished from heat extracted from the flow. The result is to assign turbine work a combination of work and heat transfer, a quantity larger than the actual turbine work. Thus, in order to accurately estimate *adiabatic* efficiency using the aerodynamic approach, the change in rake efficiency due to heat transfer had to be estimated and corrected. The

purpose of this section is to similarly characterize the required heat transfer correction to mechanical efficiency.

In Section 4.5 it was assumed that all heat transfer from the flow to the turbine occurs at an equivalent temperature T^*. Further assuming the entropy generated by this heat transfer is reversible, adiabatic and measured exit total enthalpies were related to heat transfer in Equation 4.17. This led to a relationship between adiabatic and aerodynamic rake efficiencies and heat transfer shown in Equation 4.18. Mechanical efficiency is similarly related to adiabatic efficiency and heat transfer. Referring to derivations by Keogh, this relationship can be expressed as follows [3]:

$$\eta_{ad,brk} = \eta_{brk} + \frac{Q}{h_{T4} - h_{T5,is}} \left(1 - \frac{T_5}{T^*}\right) = \eta_{brk} + \Delta\eta_{brk,ht} \tag{5.13}$$

As seen from this equation, adiabatic efficiency is underpredicted due to heat transfer by the mechanical approach, not overpredicted as by the aerodynamic approach. In addition, the term multiplying the heat load in this correction, $\left(1 - \frac{T_5}{T^*}\right)$, is much smaller than that in Equation 4.18, $\left(\frac{T_5}{T^*}\right)$. This means heat transfer will affect mechanical efficiency predictions much less than aerodynamic rake efficiency predictions. This is verified by comparing the aerodynamic corrections in Table 4.3 to the mechanical corrections explained below and summarized in Table 5.2.

As explained in Section 4.5, Keogh estimates the heat transfer at an inlet temperature of $170°F$ to be approximately 2.00% of the ideal total enthalpy drop across the turbine [3]. The conditions for this estimate are very near those used in experiment 038, thus, the heat transfer during this experiment is assumed to be this 2.00%. This is shown in Table 4.3 along with heat loads for experiments 038 and 039 determined in Section 4.5 by comparing aerodynamic efficiency predictions. This information along with Equation 5.13 may then be used to determine the required heat transfer correction to mechanical efficiency. Again assuming an equivalent heat transfer temperature, the required correction to mechanical efficiency due to heat transfer for experiment 038 is approximately 0.14%. This correction for experiments 039 and 034, inlet temperature $200°F$ and $220°F$ respectively, is approximately

Table 5.2: Mechanical Efficiency Heat Transfer Correction Summary

Experiment	034	038	039
$T_{T4}\,(^\circ F)$	220	175	200
$T^*\,(^\circ F)$	134	104	120
$\frac{Q}{h_{T4}-h_{T5,is}}$	3.75%	2.00%	2.40%
$\Delta\eta_{brk,ht}$	0.27%	0.14%	0.17%

0.17% and 0.27%.

The reason that mechanical efficiency measurements are much less affected by heat transfer than aerodynamic rake measurements is clear. As explained above, the aerodynamic calculation of turbine work is unable to distinguish occurring heat transfer. Using the mechanical approach, however, turbine work is measured directly from turbine torque and speed, independent of any heat transfer taking place. This is an intuitive result that is verified by experimental data.

5.5 Additional Corrections

Currently, other processes thought to affect mechanical adiabatic efficiency measurement are being studied to determine appropriate corrections. These items are thought to be of second order relative to those discussed in the three previous sections, however, when combined, they could result in a significant correction to measured mechanical adiabatic efficiency.

An additional non-adiabatic effect not discussed in Section 5.4 is thought to affect mechanical adiabatic efficiency measurement. This effect is heat transfer to the supply tank struts upstream of the upstream total temperature measurement locations. Because upstream total temperature is measured between struts, the cooling behind these struts is not taken into account. For aerodynamic measurements of efficiency, the flow field is sampled between these struts upstream and downstream and this heat transfer does not alter the indicated efficiency as the circumferential temperature nonuniformity is not fully mixed-out

in passing through the turbine stage. The mechanical measurement of turbine work is a global one however. A 120° circumferential sector with uniform temperature can not be concentrated on and the nonuniformities outside of this sector excluded. The strut cooling effect will lower the upstream mass averaged total enthalpy below that indicated by upstream total temperature measurements. This will result in lower indicated turbine work extraction and mechanical efficiency. This correction, which will require analysis to determine the heat transferred to the supply tank struts, will likely be more significant than the non-adiabatic correction discussed in Section 5.4.

The supply tank struts similarly affect upstream total pressure measurement. Currently, the blockage resulting from these struts is not accounted for in determining upstream total pressure as these measurements are taken between struts as are total temperature measurements. The result is a lower upstream mass averaged total pressure than indicated by measurement. This will further decrease indicated mechanical efficiency.

Bearing friction absorbs turbine power and reduces that indicated by the eddy current brake torque meter. Significant levels of bearing friction would thus result in underestimation of mechanical adiabatic efficiency. Early calculations indicate, however, that this effect might contribute only on the order of 0.10% in adiabatic efficiency.

Windage of the turbine shaft and eddy current brake drum would also affect indicated turbine power. Because of low rotational speeds and small shaft and drum length to diameter ratios, this effect is thought to be very small. Calculations verifying this presumption, however, have not been completed.

This section has proposed additional effects within the Blowdown Turbine thought to affect the mechanical measurement of turbine adiabatic efficiency. These effects are currently being studied in the development of corrections that will account for them. When combined, it is expected that they may contribute several tenths of one percent to measured mechanical adiabatic efficiency.

5.6 Post-Test Efficiency Uncertainty Analysis

Section 5.2 estimates the absolute and relative uncertainties in mechanical adiabatic efficiency measurement to be 0.56% and 0.37% respectively. As explained in Section 4.6, efficiency bias can not be determined and absolute uncertainty can not be verified from experimental data. Efficiency relative uncertainty may be determined, however, allowing verification of the pre-test estimate. That is the purpose of this section. In addition, mechanical efficiency relative uncertainty will be compared to aerodynamic rake efficiency relative uncertainty determined in Section 4.6. The same comparison will be presented for mechanical and aerodynamic heat transfer corrections and the resulting mechanical and aerodynamic adiabatic efficiencies.

As in Section 4.6, experiments 025 and 026, near identical simulations of the full-scale turbine design point, will be used to determine the repeatability of the mechanical efficiency measurement. To reiterate, repeatability is determined by the precision index S, as defined in Equation 4.19. A value of 1.28 will again be assumed for $d_2{}^*$.

Table 5.3 summarizes mechanical efficiency predictions from experiments 025 and 026. As seen, they are extremely close; the relative uncertainty in this measurement is estimated to be 0.02%. This is much lower than the aerodynamic rake efficiency relative uncertainty of 0.60% to 0.65% determined in Section 4.6.

Also shown in Table 5.3 are mechanical adiabatic efficiencies determined from the heat transfer correction discussed in Section 5.4. The precision index of this correction (as a percentage of the correction, $S_*/*$) is identical to that of the aerodynamic rake efficiency correction shown in Table 4.4. However, the resulting relative uncertainty in this correction is only 0.15% compared to the 2.03% relative uncertainty in the aerodynamic rake efficiency correction. This is a result of the correction magnitudes. In the mechanical case, this correction is only 0.27% where in the aerodynamic case, it is 3.49%. This can be seen by the correction influence coefficients as well. The mechanical and aerodynamic correction influence coefficients are 0.003 and 0.040 respectively. In other words, the effect of the correction on aerodynamic adiabatic efficiency uncertainty will be an order of magnitude

Table 5.3: Post-Test Efficiency Uncertainty Analysis Summary

	025	026	C_*	$S_*/*$	t_{95}	$U_{95,rel}$
π_t	95.6%	95.8%	-	-	-	-
N_{cor}	102.8%	102.0%	-	-	-	-
R_e	106.7%	110.7%	-	-	-	-
γ_4	99.9%	100.8%	-	-	-	-
η_{brk}[4]	−6.8%	−6.7%	0.997	0.01%	2.00	0.02%
$\Delta\eta_{brk,ht}$	0.27%	0.27%	0.003	29.05%	2.00	0.15%
$\eta_{ad,brk}$[4,5]	−6.5%	−6.4%	-	0.09%	2.00	0.16%

larger than the effect of the correction on mechanical adiabatic efficiency uncertainty. This is verified in Tables 4.4 and 5.3 where the aerodynamic and mechanical adiabatic efficiency relative uncertainties are seen to be 2.12% and 0.16% respectively. These uncertainties differ by more than one order of magnitude.

This analysis thus concludes that turbine adiabatic efficiency may be measured with 0.16% relative uncertainty by the mechanical approach. This is much lower than the 0.37% pre-test estimate. The absolute uncertainty of this measurement can not be verified by experimental data, however, pre-test estimates indicate a level of 0.56%. This may be quite optimistic, though, given the additional corrections yet to be applied. Nonetheless, the relative uncertainty of this measurement far exceeds the goal of below 0.50%. These uncertainties are also much less than those determined for the aerodynamic approach. As explained in Section 4.6, this approach does not measure adiabatic efficiency with uncertainty consistent with the objectives of this work due to the method used to determine the required heat transfer correction. However, using the same method to determine the heat transfer correction, the mechanical approach is successful. This is because of the relatively small effect heat transfer has on the mechanical measurement of efficiency. It is further con-

[4]Efficiency is referenced to the Craig and Cox empirical efficiency estimate at the smaller rotor tip clearance presented in Section 6.3.2.

[5]As previously explained, all mechanical efficiency predictions are based on real gas ideal turbine work, thus, this is where the heat transfer correction is applied. Because of the agreement between the gas models shown in Section 4.4, however, comparison of uncertainties in this prediction to pre-test estimates assuming perfect gas behavior is still valid.

cluded that for this reason alone, the mechanical approach to measuring turbine adiabatic efficiency is more effective in terms of measurement uncertainty.

5.7 Chapter Summary

This chapter has discussed mechanical measurement of adiabatic efficiency. The discussion began with a pre-test mechanical adiabatic efficiency uncertainty analysis. It was estimated that this measurement could be made with 0.56% absolute uncertainty, very near the pre-test aerodynamic adiabatic efficiency absolute uncertainty estimate of 0.61%. In addition, mechanical adiabatic efficiency relative uncertainty was estimated to be 0.37%, slightly lower than the 0.49% pre-test aerodynamic estimate.

This analysis was followed by a discussion on mechanical efficiency calculation. This concluded with the presentation of this calculation for experiment 024, a baseline full-scale turbine design point simulation. The resulting mechanical efficiency prediction was near -7% relative to the Craig and Cox empirical estimate and relatively constant between $400 - 1000\ ms$.

This calculation was followed by an analysis of the effect of heat transfer on mechanical efficiency measurement. It was shown, from heat transfer estimates presented in Section 4.5, that mechanical efficiency underpredicts adiabatic efficiency by approximately 0.27% at an inlet temperature of $220°F$ due to heat transfer effects.

This chapter concludes with a post-test mechanical efficiency uncertainty analysis. The objective of this analysis was to determine the actual repeatability of this measurement and compare this result to the pre-test estimate. It was shown that mechanical efficiency is repeatable within 0.02% and mechanical adiabatic efficiency, within 0.16%. The additional relative uncertainty in adiabatic efficiency was due to uncertainty in the required heat transfer

correction. It was still much lower than the pre-test estimate of 0.37% however. It was further concluded that because of the relative magnitudes of the heat transfer corrections required for the mechanical and aerodynamic approaches, the mechanical approach is much

less sensitive to non-adiabatic effects and thus produces much more consistent efficiency predictions.

Chapter 6

Analysis of Efficiency Measurements

6.1 Introduction

This chapter will summarize aerodynamic and mechanical adiabatic efficiency measurements, discussed in Chapters 4 and 5, for each experiment conducted during this work as summarized in Table 3.2. This will allow characterization of turbine performance at off-design conditions including variation in stage pressure ratio, corrected speed, and rotor tip clearance. This chapter concludes with estimates of the true adiabatic efficiency of the turbine stage considered in this work through well known correlations. This will include comparisons to aerodynamic and mechanical adiabatic efficiency measurements which will lend insight into the bias errors in these measurements.

6.2 Turbine Off-Design Performance

6.2.1 Introduction

Table 3.1 summarizes the full-scale turbine operating points simulated during this work. As explained, this test matrix provides data at higher and lower than design stage pressure

Table 6.1: Turbine Efficiency Analysis Notation

Notation	Explanation
$\Delta\eta_{ad,brk,N_{cor}}$	The change in mechanical adiabatic efficiency due to variation in corrected speed.
$\Delta\eta_{ad,rg,\delta}$	The change in real gas aerodynamic adiabatic efficiency due to variation in rotor tip clearance.
$\eta_{ad,emp,0.5\,\delta}$	Adiabatic efficiency at the smaller rotor tip clearance estimated through correlations.
$\eta_{ad,CC,\delta}$	Adiabatic efficiency at the larger rotor tip clearance estimated by Craig and Cox.

ratio and corrected speed, all at two rotor tip clearances. This off-design data is desired not only to characterize full-scale turbine performance at these operating conditions, but also to test the resolution of efficiency measurement. This section will examine the change in measured efficiency due to these off-design operating conditions. This will result in a characterization of turbine off-design performance in terms of adiabatic efficiency. Before this analysis begins, however, it is important to define a consistent notation which will be used in the remainder of this chapter. Examples of this notation are presented in Table 6.1.

6.2.2 Variation in Corrected Speed

As defined in Equation 3.3, corrected speed is directly proportional to rotor mechanical speed. As shown in Figure 6-1, increasing rotor mechanical speed, U, decreases rotor relative inlet angle, β_2, as the stator exit velocity vector, C_2, is constant. This angle is essentially the rotor angle of attack, thus, decreasing this angle will reduce blade loading. It is therefore expected that increasing corrected speed, for constant stage inlet total temperature and pressure, will reduce blade loading and increase efficiency.

This is indeed the trend observed in Table 6.2. The mechanical approach predicts a 1.33% change in adiabatic efficiency at 109.6% corrected speed and a -0.16% change at 96.8%. The aerodynamic approach predicts changes of 0.37% and -0.47% respectively. These changes are within the relative uncertainty of the measurement. The mechanical ap-

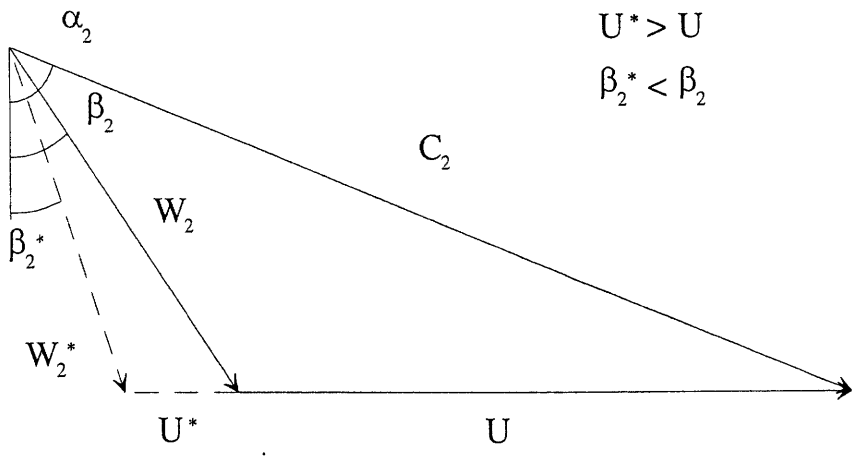

Figure 6-1: Effect of Mechanical Speed on Rotor Incidence

Table 6.2: Changes in Efficiency for Variation in Corrected Speed

Experiment	029	024	028
Target N_{cor}	105.0%	100.0%	95.0%
Actual N_{cor}	109.6%	100.4%	96.8%
Target π_t	100.0%	100.0%	100.0%
Actual π_t	96.4%	95.6%	95.0%
$\Delta\eta_{ad,brk,N_{cor}}$	1.33%	-	−0.16%
$\Delta\eta_{ad,rg,N_{cor}}$	0.37%	-	−0.47%
$\Delta\eta_{ad,brk}(N_{cor}) = 0.0412\ N_{cor}$ - 4.1405			

proach, however, verifies the expected trend between corrected speed and efficiency. Moreover, this trend is very near linear. The least squares fit is also shown in Table 6.2. This expression will be used in proceeding sections to correct changes in efficiency for inadvertent variation in corrected speed.

6.2.3 Variation in Pressure Ratio

Pressure ratio is one indication of the amount of work extracted by the turbine stage. Assuming calorically perfect gas behavior to simplify algebra and referring to the definitions of total temperature and pressure ratio in Section 3.3, turbine work may be written as

follows:

$$\begin{aligned} W_t = \Delta h_{t,45} &= \bar{C}_P T_{T4} \left(1 - \tau_t\right) \\ &= \bar{C}_P T_{T4} \eta_t \left(1 - \pi_t^{\frac{R}{\bar{C}_P}}\right) \end{aligned} \tag{6.1}$$

According to this expression, a larger pressure ratio (inverse) indicates increased turbine work extraction, all else constant. If work coefficient is then defined as follows:

$$\psi = \frac{\Delta h_{t,45}}{U^2} = \frac{\bar{C}_P T_{T4} \eta_t}{U^2} \left(1 - \pi_t^{\frac{R}{\bar{C}_P}}\right) \tag{6.2}$$

it can seen that work coefficient similarly scales with pressure ratio for constant rotor speed, U. Finally, assuming mass flow is not significantly affected by pressure ratio and referring ahead to Figure 6-2, it is seen that a larger pressure ratio (inverse) increases work extraction and work coefficient and decreases efficiency. The reverse is also true. This is the expected trend between adiabatic efficiency and pressure ratio. Efficiency measurements will now be analyzed to determine if this trend is realized.

Table 6.3 summarizes those experiments with varying pressure ratio at the smaller rotor tip clearance. As seen from this data, the mechanical approach predicts a slightly higher efficiency at each off-design pressure ratio condition and the aerodynamic approach, a slightly lower efficiency. The absolute change in efficiency in all cases is relatively small however. The changes predicted by the aerodynamic approach are again near the relative uncertainty of the measurement. The mechanical approach, conversely, should resolve any significant changes in efficiency due to its high level of repeatability. The changes in efficiency predicted by this approach, however, do not follow the expected trend described above. This can partly be explained by additional variation in corrected speed. Experiments 027 and 032 were conducted at slightly higher than target corrected speed due to uncertainty in setting the eddy current brake excitation for off-design pressure ratio conditions. Using the expression in Table 6.2, these changes in efficiency are corrected for this variation in corrected speed and the results are also shown in Table 6.3. After this correction is applied, the changes in efficiency predicted by the mechanical approach are reduced but the trend

Table 6.3: Changes in Efficiency for Variation in Pressure Ratio

Experiment	027	024	032
Target π_t	110.0%	100.0%	90.0%
Actual π_t	102.1%	95.6%	87.5%
Target N_{cor}	100.0%	100.0%	100.0%
Actual N_{cor}	101.7%	100.4%	104.8%
$\Delta\eta_{ad,brk,\pi_t}$	0.60%	-	0.28%
$\Delta\eta_{ad,rg,\pi_t}$	−0.68%	-	−0.83%
$\Delta\eta_{ad,brk,\pi_t,cor}$	0.55%	-	0.10%
$\Delta\eta_{ad,rg,\pi_t,cor}$	−0.73%	-	−1.01%

remains the same. It is therefore concluded from this analysis that for the magnitude of pressure ratio variation examined here and possibly due to additional variation in rotor speed and/or mass flow, there is no recognizable trend between pressure ratio and adiabatic efficiency.

6.2.4 Variation in Rotor Tip Clearance

As explained in Section 1.2, larger rotor tip clearance results in increased secondary flow degrading turbine performance and efficiency. During this work, all experiments were repeated for two tip clearances achieved with two ablatable rub strips of different diameter surrounding the rotor blades. Table 6.4 summarizes the changes in efficiency between equivalent experiments at different tip clearances.

As seen from Table 6.4, near doubling the rotor tip clearance results in an average 1.95% decrease in adiabatic efficiency as predicted by the mechanical approach independent of any other operating condition. This is perhaps the most credible evidence available of the repeatability of the mechanical adiabatic efficiency measurement. Even as corrected speed, pressure ratio, and other operating conditions are varying, this measurement consistently resolves the change in efficiency resulting from increased rotor tip clearance. As for the aerodynamic approach, it predicts significantly higher changes in efficiency due to variation in rotor tip clearance than due to variation in corrected speed or pressure ratio, however,

Table 6.4: Changes in Efficiency for Variation in Rotor Tip Clearance

Simulating	$\pi_t{}^+ N_{cor}$		$\pi_t{}^- N_{cor}$		$\pi_t N_{cor}{}^+$	
Experiment	027	035	032	033	029	037
Tip Clearance	$0.5\,\delta$	δ	$0.5\,\delta$	δ	$0.5\,\delta$	δ
$\Delta\eta_{ad,brk,\delta}$	-	-2.01%	-	-1.93%	-	-1.91%
$\Delta\eta_{ad,rg,\delta}$	-	$+7.78\%$	-	-1.86%	-	-3.00%

the limited precision of this measurement prevents characterization of turbine performance based on changes in efficiency determined from this approach. In addition, this approach predicts unreasonably high adiabatic efficiencies for experiments 035 and 036. This results in an increase in efficiency between experiments 027 and 035 even though rotor tip clearance is increased. This is likely due to isolated downstream total temperature measurement errors as the mechanical approach is not affected and the aerodynamic approach does not produce these results for any other experiment.

6.2.5 Summary of Turbine Off-Design Performance

The three previous subsections examined turbine off-design performance in terms of the resulting change in measured adiabatic efficiency. This analysis also provided additional information on efficiency measurement repeatability and resolution.

Off-design operating conditions examined include variation in corrected speed, pressure ratio, and rotor tip clearance. It was shown that over a small range of corrected speed, adiabatic efficiency increases linearly with increasing corrected speed, all else constant. Using this relationship to correct efficiency measurements for inadvertent variation in corrected speed, it was shown that there is no recognizable trend between adiabatic efficiency and pressure ratio for the magnitude of pressure ratio variation examined. Finally, it was shown that near doubling the rotor tip clearance resulted in an average 1.95% decrease in adiabatic efficiency independent of any other operating condition. These conclusions are summarized in Table 6.5. Furthermore this analysis, specifically the near constant decrease in adiabatic efficiency due to increased rotor tip clearance predicted by the mechanical efficiency

Table 6.5: Summary of Turbine Off-Design Performance

Variation	$\Delta\eta ad, brk$
N_{cor}	$\Delta\eta_{ad,brk}(N_{cor}) = 0.0412\ N_{cor}$ - 4.1405
π_t	No Recognizable Trend
$0.5\,\delta \rightarrow \delta$	-1.95%

measurement approach, provides more evidence of the repeatability and resolution of this measurement. This analysis also demonstrates the limited repeatability of the aerodynamic efficiency measurement.

6.3 Empirical Estimation of Adiabatic Efficiency

6.3.1 Introduction

As shown in Equation 1.1, turbine adiabatic efficiency represents the fraction of isentropic work extracted by the turbine during adiabatic operation. This fraction is always less than unity because of departures from isentropic flow. According to Denton, these departures have historically been divided into three categories, *profile loss*, *endwall loss*, and *leakage loss* [15].

Profile loss describes the loss generated in the blade and vane boundary layers away from the endwalls. Here the flow is often assumed two-dimensional so that cascade test correlations and boundary layer calculations may be applied. In addition, the loss associated with finite trailing-edge thickness is generally considered *profile loss* [15].

Endwall loss, also known as *secondary loss*, results from secondary flows established when annulus boundary layers interact with blade row boundary layers near endwall regions. Often, loss not otherwise accounted for is also considered *secondary loss* [15].

Leakage loss results from flow leakage over blade tips and under vane hub clearances. These leakage flows often interact with the secondary flows described above causing difficulty in distinguishing between *endwall* and *leakage losses* [15].

Efficiency may be roughly estimated without knowledge of each loss category. Figure 6-2

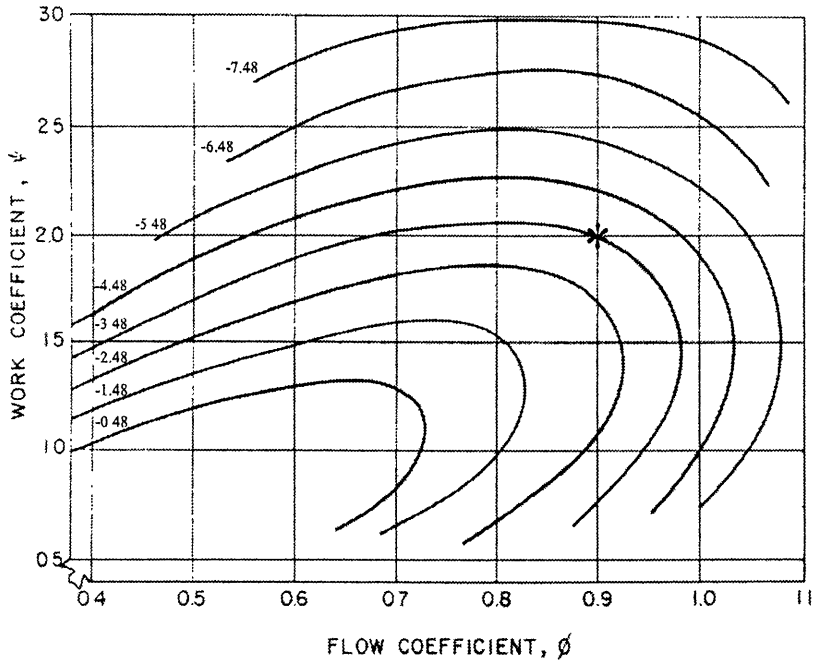

Figure 6-2: Efficiency Contours Versus Flow and Work Coefficients [13]

shows efficiency contours versus flow and work coefficients. This very common correlation yields an estimate of -3.48%[1] for the efficiency of the turbine stage considered in this work[2]. A more precise efficiency estimate, however, requires estimation of each loss category. Many methods have been developed to do this given blade and annulus geometries and stage operating conditions. The next subsection does so using an analysis based on a well known method published in 1971 by Craig and Cox [14]. This is followed by an additional analysis utilizing *TURBine ANalysis*, a government-owned computer code developed at the NASA Lewis Research Center. Results from both analyses as well the efficiency estimate from Figure 6-2 are summarized in Table 6.7.

[1]This efficiency is referenced to $\eta_{ad,CC,0.5\,\delta}$ presented in Section 6.3.2. It is taken from Figure 6-2 for the following values: $\phi \approx 0.90$, $\psi \approx 2.00$

[2]These contours represent a 50% reaction turbine stage whereas the turbine of interest is near 36%. This will result in a slight overestimation of efficiency.

6.3.2 Craig and Cox Method

Following an example by Wilson [13], this subsection estimates the adiabatic efficiency of the turbine stage considered in this work based on the empirical method developed by Craig and Cox [14]. This method estimates *profile* and *secondary losses* and relates them to a zero-clearance efficiency. A tip clearance correlation is applied to account for *leakage loss* resulting in an estimate of stage isentropic efficiency. The full analysis is summarized in Table 6.6.

As explained above, *profile loss* describes the loss generated in the blade and vane boundary layers. This loss will thus depend on the state of the boundary layer and may be parameterized by blade geometry. Figure 6-3 shows the modified basic *profile loss* coefficient versus lift parameter and contraction ratio. Lift parameter is shown in Figure 6-4 versus inlet and exit flow angles and contraction ratio in Figure 6-5 versus a function of these angles and blade axial chord and spacing. The modified basic *profile loss* coefficient accounts for losses incurred within the blade or vane boundary layer but is not influenced by trailing-edge thickness. The additional *profile loss* associated with finite trailing-edge thickness is accounted for in Figure 6-6. Here, *profile loss* increment and ratio due to trailing-edge thickness are plotted versus normalized trailing-edge thickness. Finally, *profile loss* must be corrected for Reynolds number effects. Craig and Cox present all correlations at a throat Reynolds number of 10^5 and correct for the actual throat Reynolds number using the ratio shown in Figure 6-7. As seen, this ratio is more a function of surface finish than Reynolds number. For very smooth finishes, Reynolds numbers larger than 10^5 reduce *profile loss*. For moderate to rough finishes, however, *profile loss* is substantially increased independent of Reynolds number. With this information *profile loss* may be calculated as follows:

$$\mathcal{X}_{pro} = \left(\frac{\mathcal{X}_{pro,basic,mod}}{\frac{s}{b} cos|\beta_2|} \cdot \frac{\mathcal{X}_{pro,t_{te}}}{\mathcal{X}_{pro,t_{te}=0}} \cdot \frac{\mathcal{X}_{R_e}}{\mathcal{X}_{R_e=10^5}} \right) + \Delta\mathcal{X}_{pro,t_{te}} \tag{6.3}$$

where s is the blade or vane spacing, b is the axial chord, and β_2 is the relative exit angle. The first fraction is also known as the corrected basic profile loss parameter, $\mathcal{X}_{pro,basic}$.

As explained above, *secondary loss* is primarily the result of secondary flows established

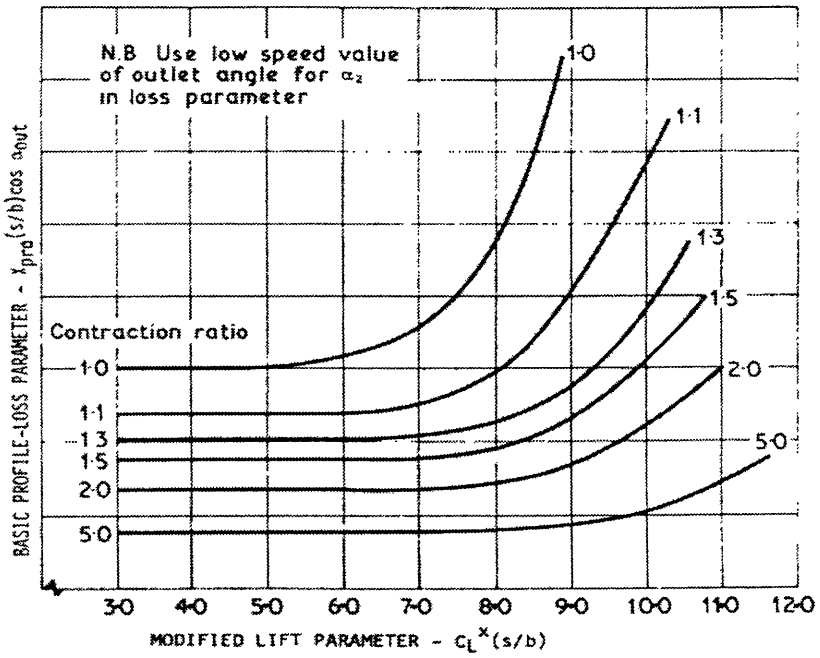

Figure 6-3: Basic *Profile Loss* [13]

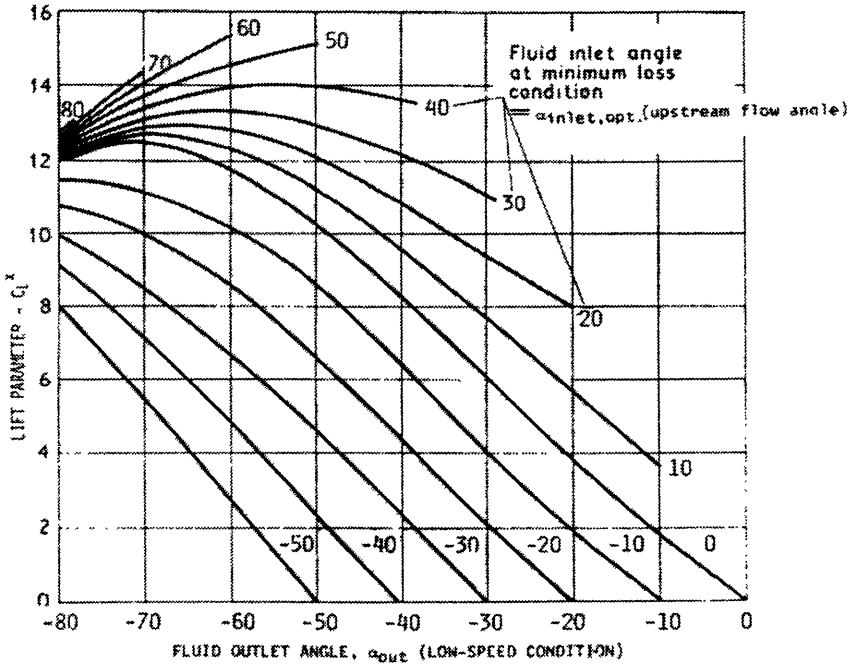

Figure 6-4: Lift Parameter [13]

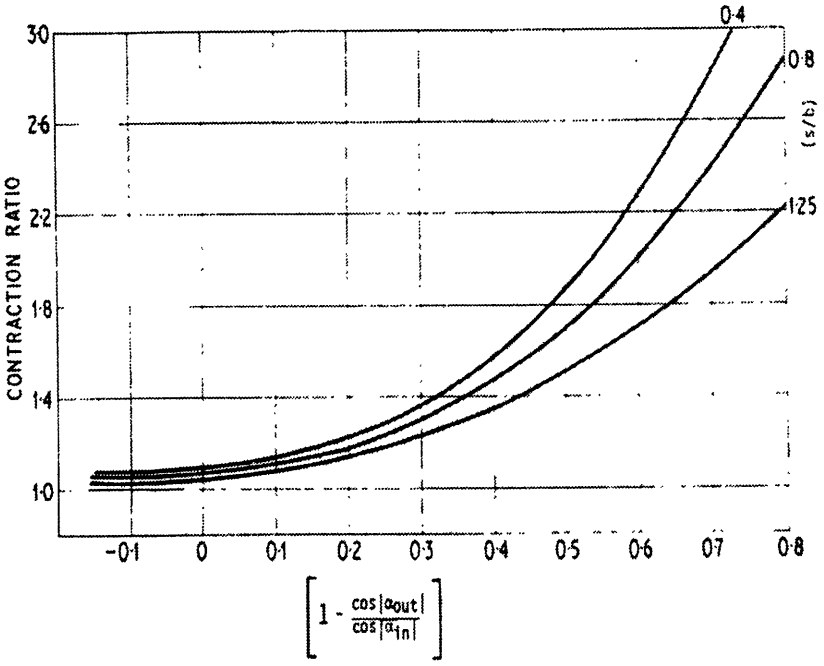

Figure 6-5: Contraction Ratio [13]

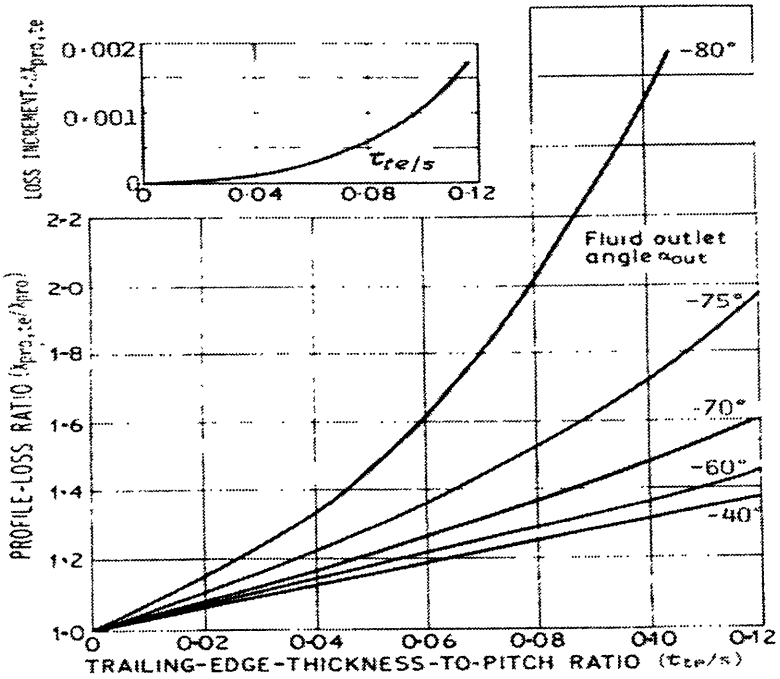

Figure 6-6: *Profile Loss* Associated With Finite Trailing-Edge Thickness [13]

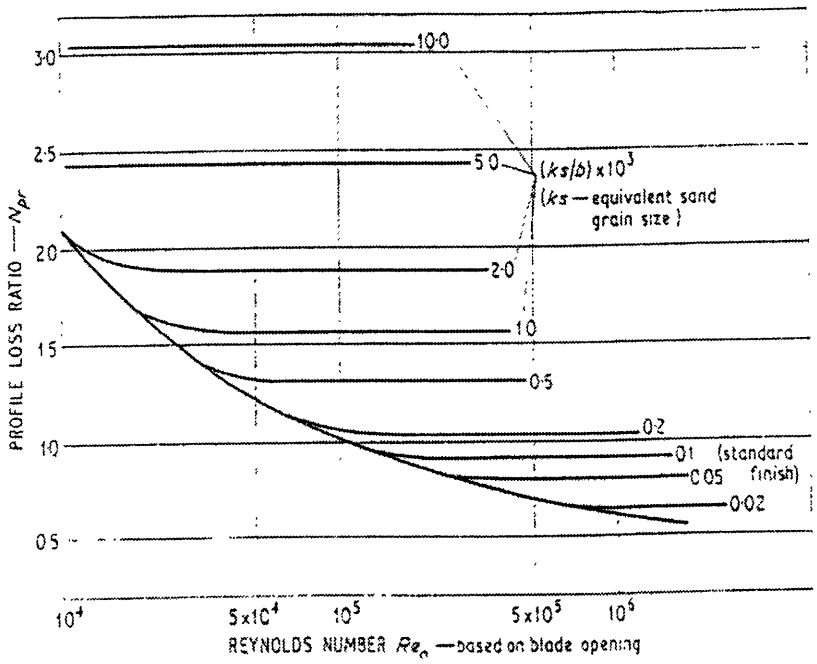

Figure 6-7: Effect of Reynolds Number on *Profile Loss* [14]

by the interaction of annulus and blade row boundary layers. This is a three-dimensional effect and the loss it generates "corrects" the two-dimensional assumption used to evaluate *profile loss* above. That is, when combined, the total loss will reflect not only the two-dimensional component generated within the blade or vane boundary layer but also that associated with the real three-dimensional aspects of the geometry. It is therefore presumed that *secondary loss* will largely be affected by blade aspect ratio. This is verified in Figure 6-8 where the *secondary loss* coefficient is plotted versus blade aspect ratio for three different blade angle configurations. As seen, a blade with lower aspect ratio, or one more three-dimensionally influenced, will suffer larger *secondary loss*. At this point, the total zero-clearance loss coefficient may be defined as follows:

$$\mathcal{X}_{tot,zc} = \mathcal{X}_{pro} + \mathcal{X}_{sec} \tag{6.4}$$

Note that this quantity is defined separately for the blade and vane rows.

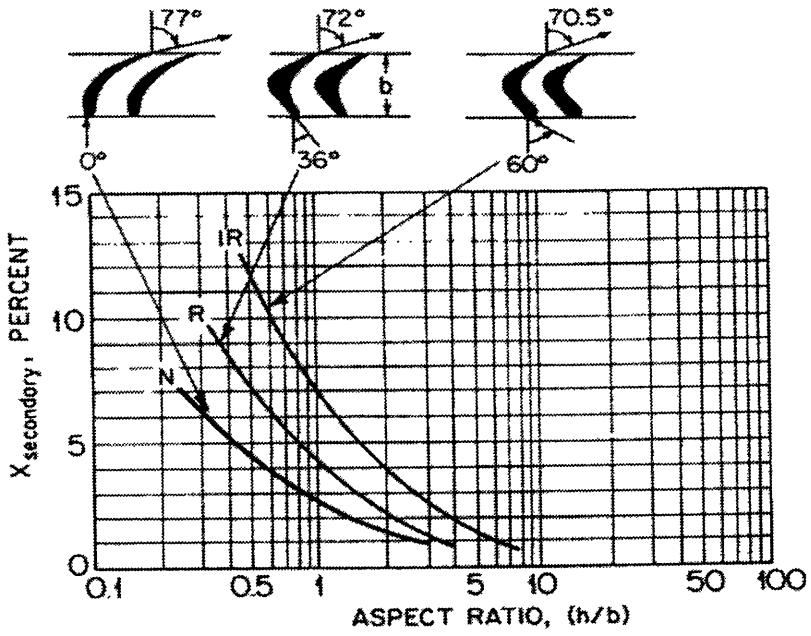

Figure 6-8: *Secondary Loss* [13]

So far loss has been expressed as a loss coefficient, $\mathcal{X}$, but has not been directly related to efficiency. According to Denton, there are many ways to define loss coefficient depending on the machine being analyzed and the purpose of the analysis [15]. The correlations of Craig and Cox, however, are based on the total pressure loss coefficient defined as follows:

$$\mathcal{X} = \frac{P_{T1} - P_{T2}}{P_{T2} - P_2} \tag{6.5}$$

where subscripts 1 and 2 represent conditions upstream and downstream of the blade or vane row being considered [14]. This is simply the loss in total pressure across the row normalized by the downstream dynamic pressure. This loss in total pressure is a direct measure of the departure from isentropic flow discussed previously. With loss coefficient known, total pressure loss may be evaluated as follows:

$$\Delta P_T = \mathcal{X}_{tot,zc} \cdot \frac{1}{2} \rho_{T2} {V_2}^2 \tag{6.6}$$

Table 6.6: Summary of Craig and Cox Analysis

Parameter	Value		
	Blade	Vane	Stage
${C_L}^X$	14.600	12.533	-
CR[3]	1.160	2.096	-
$\mathcal{X}_{pro,basic}$	0.039	0.024	-
$\frac{\mathcal{X}_{pro,t_{te}}}{\mathcal{X}_{pro,t_{te}=0}}$	1.178	1.147	-
$\Delta\mathcal{X}_{pro,t_{te}}$	$1.875e^{-4}$	$1.000e^{-4}$	-
$\frac{\mathcal{X}_{Re}}{\mathcal{X}_{Re=10^5}}$	2.000	2.000	-
$\mathcal{X}_{pro}$	0.243	0.162	-
$\mathcal{X}_{sec}$	0.034	0.027	-
$\mathcal{X}_{tot,zc}$	0.277	0.189	-
$\Delta P_T\,(psia)$	0.631	0.887	1.518
$\eta_{ad,0.5\,\delta}$	-	-	$\eta_{ad,CC,0.5\,\delta}$[4]
$\eta_{ad,\delta}$	-	-	-2.06%

where V_2 is the relative exit velocity from the blade or vane row being considered and g is the acceleration due to gravity. This quantity is again calculated separately for the blade and vane rows and summed. Once the overall stage total pressure loss is known, zero-clearance efficiency is defined by Wilson as follows [13]:

$$\eta_{ad,zc} = \frac{1 - \left(\frac{P_{T5}+\Delta P_T}{P_{T4}}\right)^{\frac{R}{C_P}}}{1 - \left(\frac{P_{T5}}{P_{T4}}\right)^{\frac{R}{C_P}}} \tag{6.7}$$

assuming calorically perfect gas behavior.

Once again, this is the zero-clearance efficiency; *leakage loss* has not been considered. According to Wilson, the simplest correlation accounting for *leakage loss* is that the ratio of finite-clearance to zero-clearance efficiencies is equal to the ratio of blade annulus to case

[3] CR stands for "Contraction Ratio" and is shown in Figure 6-5.

[4] This empirical adiabatic efficiency estimate is used as the reference for all efficiency predictions throughout this work to conceal proprietary information. It is chosen as so for two reasons; it is the result of what is thought to be the most reliable method of empirical efficiency estimation available, and, it is the only method for which estimation uncertainty data is available. An efficiency greater than zero indicates one greater than this value and vice versa.

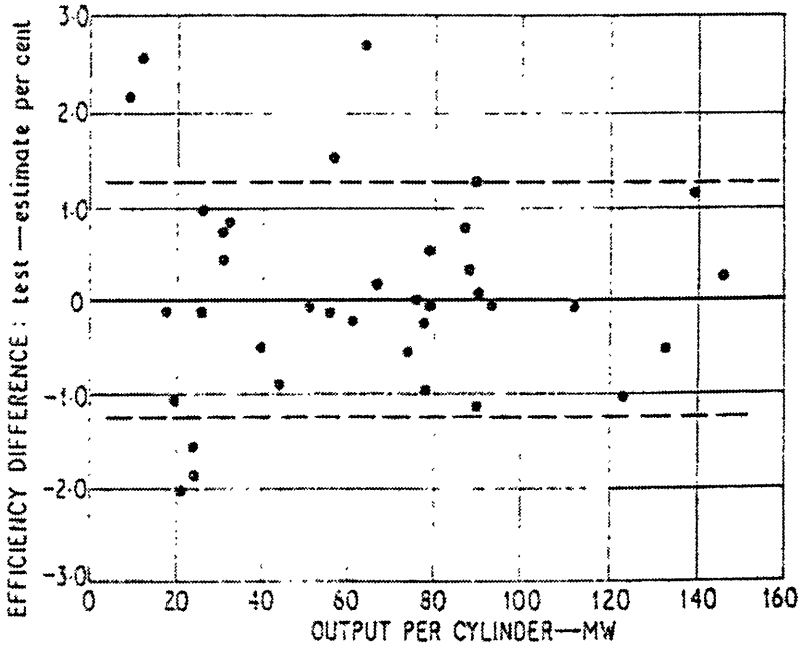

Figure 6-9: Craig and Cox Efficiency Estimation Uncertainty [14]

annulus areas. In other words,

$$\eta_{ad} = \frac{A_{t,zc}}{A_t} \cdot \eta_{ad,zc} \tag{6.8}$$

Wilson suggests this approach for unshrouded blade rows with smooth wall casings as is the case in this situation. This value represents the stage isentropic efficiency and concludes the Craig and Cox empirical adiabatic efficiency estimation analysis.

Figure 6-9 shows efficiency estimation uncertainty data for the Craig and Cox method. This data, compiled from many analyses and experiments, suggests this method generally predicts efficiency within 1.28% of the experimentally measured value.

6.3.3 *TURBine ANalysis* Computer Code

TURBine ANalysis, or *TURBAN* is a government-owned computer code developed by the Propulsion Systems Analysis Office at the NASA Lewis Research Center. This code per-

Table 6.7: Summary of Empirical Adiabatic Efficiency Estimates

Method	$\psi\phi$[5]	Craig and Cox	*TURBAN*
$\eta_{ad,emp,0.5\,\delta}$	-3.48%	-	-4.84%
$\eta_{ad,emp,\delta}$	-	-2.06%	-6.67%
$\Delta\eta_{ad,emp,\delta}$	-	-2.06%	-1.83%
U_{xx}[6]	?	1.28%	?

forms meanline turbine analysis and design calculations given basic stage geometry and operating conditions. Output includes stage property distributions and overall stage performance and efficiency data. Appendix C provides more information on *TURBAN* including reference information, a sample output file, and an explanation of its use in this situation. Adiabatic efficiency of the turbine stage considered in this work as predicted by *TURBAN* is presented in Table 6.7.

6.3.4 Summary of Empirical Adiabatic Efficiency Estimates

Table 6.7 summarizes the empirical adiabatic efficiency estimates presented in the three previous subsection referenced to $\eta_{ad,CC,0.5\,\delta}$. As seen in this table, the Craig and Cox method predicts the highest efficiencies of the methods presented here. It also predicts a 2.06% decrease in efficiency due to the larger rotor tip clearance. This prediction is very near that of the mechanical approach as summarized in Table 6.4. The Craig and Cox efficiency predictions are followed by the efficiency correlation to flow and work coefficients. This prediction, only available for the nominal rotor tip clearance, is 3.48% less than the Craig and Cox reference prediction. This is followed by the efficiency predictions from *TURBAN*. These predictions are the lowest presented here and indicate a 1.83% decrease in efficiency due to the larger rotor tip clearance. This is again near that predicted by the mechanical approach.

[5]See Figure 6-2.

[6]U_{xx} is the estimated empirical adiabatic efficiency uncertainty.

Table 6.8: Summary of Efficiency Measurements

Experiment	Variation	Tip Clearance	$\eta_{ad,brk}$	$\eta_{ad,rg}$	$\eta_{ad,ig}$	$\eta_{ad,cpg}$
024	-	$0.5\,\delta$	-7.27%	-13.70%	-17.51%	-15.89%
027	${\pi_t}^+$	$0.5\,\delta$	-6.66%	-14.38%	-18.67%	-16.57%
032	${\pi_t}^-$	$0.5\,\delta$	-6.99%	-14.53%	-16.62%	-16.56%
029	${N_{cor}}^+$	$0.5\,\delta$	-5.94%	-13.33%	-16.44%	-15.48%
028	${N_{cor}}^-$	$0.5\,\delta$	-7.43%	-14.17%	-18.04%	-16.33%
021	$0.5\ R_e$	$0.5\,\delta$	-9.90%	-19.89%	-18.86%	-20.90%
034	-	δ	-8.27%	-15.32%	-17.75%	-17.34%
035	${\pi_t}^+$	δ	-8.68%	-6.60%	-12.92%	-9.44%
033	${\pi_t}^-$	δ	-8.92%	-16.39%	-17.72%	-18.28%
037	${N_{cor}}^+$	δ	-7.85%	-16.32%	-17.82%	-18.23%
036	${N_{cor}}^-$	δ	-8.86%	-4.88%	-10.81%	-7.76%
041	$0.5\ R_e$	δ	-9.17%	-22.98%	-21.45%	-23.88%
Estimated Efficiency Measurement Bias[7]			-6.74%	-13.48%	-16.60%	-15.59%

6.3.5 Comparison Between Efficiency Empirical Estimates and Measurements

Table 6.8 summarizes aerodynamic and mechanical adiabatic efficiency measurements from each experiment conducted during this work as summarized in Table 3.2. These predictions, discussed in Chapters 4 and 5, are referenced to the Craig and Cox empirical efficiency estimate at the smaller rotor tip clearance, $\eta_{ad,CC,0.5\,\delta}$, discussed in Section 6.3.2. Also included is the adiabatic efficiency measurement estimated bias for each measurement approach. As seen from this data, the estimated bias in the mechanical adiabatic efficiency measurement is approximately 6.74% relative to the Craig and Cox empirical analysis method. The aerodynamic measurement biases vary from approximately 13.50% to 16.50% depending on the gas model. These biases seem rather large, however, this is partly due to the reference efficiency chosen. As shown in the previous section, the Craig and Cox method, used to produce the reference efficiency estimate, predicts the highest efficiencies of the methods presented. Nonetheless, this method was chosen as reference because of its thoroughness

[7]Bias is estimated to be the average deviation of experiments 024 and 034 from the Craig and Cox empirical estimate at the respective rotor tip clearance.

and availability of uncertainty data.

6.4 Chapter Summary

This chapter began with an analysis intended to characterize turbine performance at off-design conditions and test the resolution of efficiency measurement. Off-design conditions examined include variation in corrected speed, stage pressure ratio, and rotor tip clearance. It was first shown that over a small range of corrected speed, adiabatic efficiency varies linearly with corrected speed, increasing as corrected speed is increased. It was then shown that adiabatic efficiency is not significantly affected by the magnitude of variation of stage pressure ratio achieved during this work. Finally, near doubling the rotor tip clearance was shown to decrease adiabatic efficiency by approximately 1.95%. By examining these changes in efficiency due to off-design operating conditions and comparing the observed trends to those intuitively expected, it was concluded that the mechanical approach to adiabatic efficiency measurement may be used to characterize turbine off-design performance in this manner. The aerodynamic approach, however, failed to establish the expected trends due to its limited level of repeatability.

Following the turbine off-design performance analysis, focus shifted to empirical estimation of adiabatic efficiency. First, it was shown that efficiency may be correlated to flow and work coefficients allowing efficiency estimation with no knowledge of loss mechanisms. To refine this estimate, however, each loss mechanism was estimated using a well known analysis method developed by Craig and Cox. This produced an estimate of the adiabatic efficiency of the turbine stage which was used as a reference for all other efficiency empirical estimates and measurements. Repeating this analysis for increased rotor tip clearance, a 2.06% decrease in efficiency was predicted. This was very near the change in efficiency predicted by the mechanical approach in Section 6.2.4 as shown in Table 6.4. Finally, data was presented showing the Craig and Cox method to be accurate within approximately 1.28% on average. Following the Craig and analysis, an additional analysis utilizing *TURBAN* was presented. This approach predicted the lowest empirical efficiencies and produced a

1.83% decrease in efficiency due to larger rotor tip clearance. This prediction was also very near that of the mechanical approach shown in Table 6.4.

After empirically estimating adiabatic efficiency, these estimates were compared to mechanical and aerodynamic efficiency measurements. Mechanical and aerodynamic efficiency measurement biases were estimated to be approximately -6.74% and -13% to -16% respectively. The relatively large biases were due partly to the chosen efficiency reference. This reference was predicted by the Craig and Cox method which produced the highest efficiency predictions of the methods presented.

Chapter 7

Conclusions and Recommendations

7.1 Review of Objectives

The primary objective of this work is to experimentally measure turbine adiabatic efficiency with uncertainty less than 0.50%. Two independent efficiency measurement approaches are taken to meet this objective. The aerodynamic approach measures turbine work from upstream and downstream total temperature and pressure and the mechanical approach, from turbine torque, speed, and mass flow. Another objective of this work is to determine by which method adiabatic efficiency may be measured most accurately and most repeatably in the short duration test facility.

In implementing these efficiency measurements, real, ideal, and calorically perfect gas models are utilized for enthalpy evaluation and efficiency calculation. Another objective of this work is to assess the validity of simplified gas models in this situation by comparing their efficiency predictions to those obtained assuming real gas behavior.

Finally, this work seeks to characterize turbine performance at off-design conditions, specifically increased rotor tip clearance. By comparing efficiency predictions between duplicate experiments at different tip clearances, the effect of increased tip clearance on adiabatic

efficiency may be determined as well as information on efficiency measurement resolution.

7.2 Aerodynamic Adiabatic Efficiency Measurement

Chapter 4 discusses the aerodynamic adiabatic efficiency measurement. A pre-test uncertainty analysis estimates the absolute and relative uncertainties in this measurement to be approximately 0.61% and 0.49% respectively based on instrumentation calibration data.

After examination of aerodynamic efficiency predictions it is determined that rake efficiency is repeatable within approximately 0.65%. These predictions, however, are sensitive to inlet total temperature due to heat transfer effects. After estimating and correcting for these effects, the relative uncertainty in aerodynamic adiabatic efficiency is estimated to be approximately 2.12%. This substantial increase in relative uncertainty is due to the uncertainty in and the magnitude of the required heat transfer correction as this correction is determined by comparing aerodynamic rake efficiency predictions. It is finally concluded that the aerodynamic approach is not capable of precise adiabatic efficiency measurement due to its sensitivity to non-adiabatic effects and the difficulty in estimating them.

7.3 Real Versus Ideal Gas Models

Section 4.3 discusses enthalpy evaluation assuming real, ideal, and calorically perfect gas behavior. It is shown that enthalpy change may be expressed as the sum of an integral of specific heat over temperature and an integral over pressure and that different gas models differ in their approximation of this expression. Real gas effects may be accounted for, as in this case, through real gas property tables allowing direct evaluation of enthalpy change.

Simplified gas models, however, evaluate this expression through numerical integration. First, property variation due to changes in pressure is neglected and enthalpy change is expressed only as the integral of specific heat over temperature. Further assumptions are required to quantify this variation in order to integrate the expression and these distinguish ideal and calorically perfect gas models.

Finally, the integration of specific heat is evaluated graphically assuming ideal and calorically perfect gas behavior and the results qualitatively compared. It is concluded that due to the near linear relationship between specific heat and temperature as determined from real gas property tables, both integrations should produce similar results and agree reasonably with the real gas evaluation. Aerodynamic efficiency predictions later show a $2 - 3\%$ deviation between the gas models.

7.4 Mechanical Adiabatic Efficiency Measurement

Chapter 5 is devoted to the mechanical measurement of adiabatic efficiency and follows closely from Chapter 4. First, a pre-test analysis estimates the absolute and relative uncertainties in this measurement to be approximately 0.56% and 0.37% respectively. These results suggest the mechanical approach will predict adiabatic efficiency with similar absolute uncertainty, but lower relative uncertainty than the aerodynamic approach.

Actual mechanical efficiency predictions show that this measurement is repeatable within 0.02%; this is only the first indication of the consistency of this measurement. Using results from the aerodynamic rake efficiency heat transfer correction analysis, mechanical efficiency is similarly corrected resulting in a mechanical adiabatic efficiency relative uncertainty of 0.16%. Although the relative uncertainty of the mechanical efficiency heat transfer correction (per unit correction) is the same as for aerodynamic rake efficiency, this uncertainty does not propagate to mechanical adiabatic efficiency as it does for aerodynamic adiabatic efficiency. This is due to the small magnitude of the mechanical efficiency heat transfer correction relative to the aerodynamic rake efficiency correction. Based on this information, it is concluded that the mechanical approach is much less sensitive to non-adiabatic effects and thus produces much more consistent efficiency predictions than the aerodynamic approach.

7.5 Turbine Off-Design Performance

The experimental test matrix, as shown in Table 3.1, provides data at, above, and below design stage pressure ratio and corrected speed, all at two rotor tip clearances. This data is used to characterize turbine off-design performance in terms of adiabatic efficiency and test efficiency measurement resolution.

As shown in Chapter 6, no recognizable trend is observed between stage pressure ratio and adiabatic efficiency. Over a small range of corrected speed, however, adiabatic efficiency varies linearly, increasing with increasing corrected speed and vice versa. Finally, near doubling the rotor tip clearance produces an average 1.95% decrease in adiabatic efficiency as predicted by the mechanical approach independent of any other operating conditions. This near constant decrease in efficiency predicted by the mechanical approach despite variation in other operating conditions is perhaps the most convincing evidence of the repeatability of this measurement.

7.6 Empirical Estimation of Adiabatic Efficiency

After characterization of turbine off-design performance, adiabatic efficiency is estimated empirically by three independent analyses. First, with no knowledge of loss mechanisms, efficiency is estimated from flow and work coefficients. Next, stage total pressure loss is estimated using the Craig and Cox method and adiabatic efficiency inferred. Finally, *TURBAN*, a preliminary turbine design and analysis code, is used to estimate adiabatic efficiency.

These analyses result in a range of empirical adiabatic efficiency estimates of approximately 4.48%. In other words, the true adiabatic efficiency is unknown. The Craig and Cox estimate, however, is chosen as the reference for *all* efficiency quotations to conceal proprietary information due to its thoroughness and availability of uncertainty data. In addition, the Craig and Cox and *TURBAN* analyses predict a decrease in adiabatic efficiency due to increased rotor tip clearance of 2.06% and 1.83% respectively. These results closely match

the 1.95% decrease in efficiency predicted by the mechanical approach.

7.7 Recommendations

This work has attempted a comprehensive summary of the work completed to date in the Blowdown Turbine facility regarding adiabatic efficiency measurement. As so, optimization of data processing and efficiency calculation has not been explored in detail. Specifically, turbine mass flow, therefore mechanical adiabatic efficiency, is slightly sensitive to the processing of the tunnel mass storage correction. In addition, a series of processes thought to affect the mechanical adiabatic efficiency measurement are discussed in Section 5.5. All of these processes should be examined thoroughly before this measurement is truly considered validated.

The most promising result of this work has been the shown repeatability of the mechanical adiabatic efficiency measurement. This is demonstrated by comparison of near identical experiments and those conducted at different rotor tip clearances. Repeatability, however, is a statistic and is sensitive to the size of the data set. It is therefore recommended that many more experiments be compared in characterizing the repeatability of this measurement. This will not likely change the overall conclusion presented here, however, it will increase confidence in the actual repeatability determined.

As a last measure of the accuracy and precision of efficiency measurement, predictions are compared to empirical estimates. These estimates, however, establish a not so narrow band of true adiabatic efficiency. Further efficiency estimates, perhaps by more sophisticated methods such as computational fluid dynamics, are therefore suggested to better characterize efficiency measurement uncertainty.

7.8 Future Work

This work has discussed efficiency measurements of a single uncooled turbine stage. Currently, these blades and vanes are being modified by wire EDM and laser-drilling to simulate

the cooling configuration of the full-scale turbine stage. The efficiency measurements presented here will then be repeated allowing the change in adiabatic efficiency due to cooling to be determined. This work is intended to acquire data for use in improving overall cooled turbine stage performance and efficiency.

The Blowdown Turbine project has the ability to directly measure the time resolved heat flux to any turbine surface. There has also been discussion on exercising this measurement capability to acquire more detailed data on cooled turbine performance. More information on heat flux measurements may be found in References [2] and [11].

Appendix A

Experimental Data

A.1 Introduction

This appendix is devoted to experimental data. Included are traces of tunnel conditions and turbine performance parameters for each experiment conducted during this study as summarized in Table 3.2. All calculations are defined in Section 3.3 and all traces are presented on the same scale for easy comparison. Filtered signals, such as Reynolds number and raw and corrected power, are the result of a Butterworth lowpass filter with cuttoff frequency approximately 25 Hz.

A.2 Figures

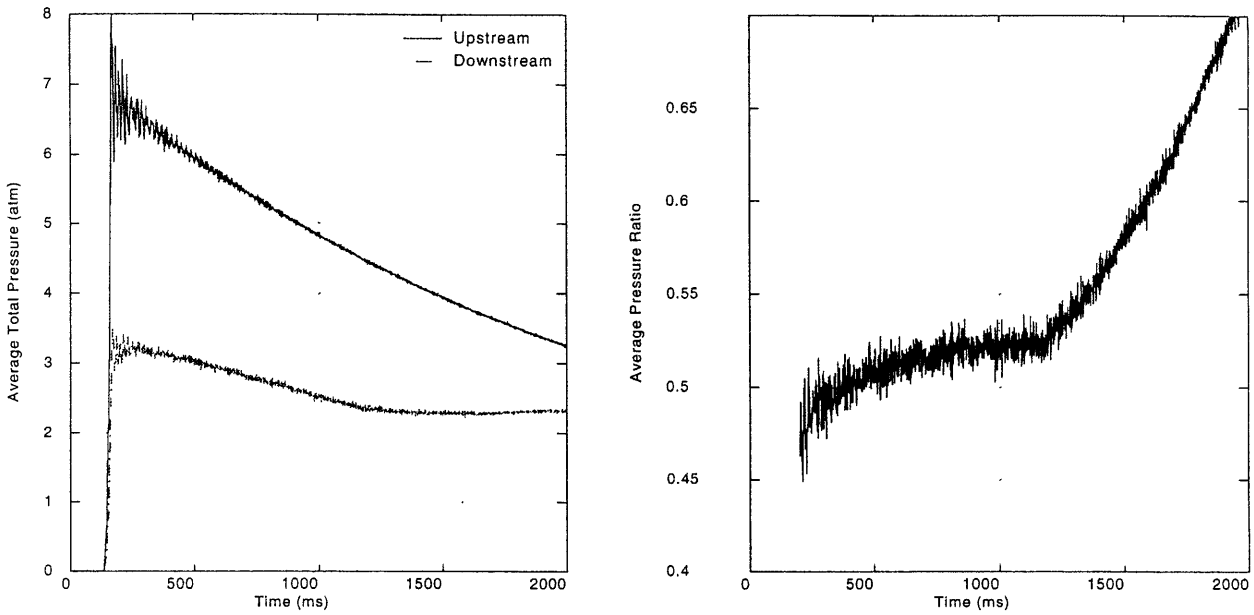

Figure A-1: Experiment 024 Average Total Pressure and Pressure Ratio

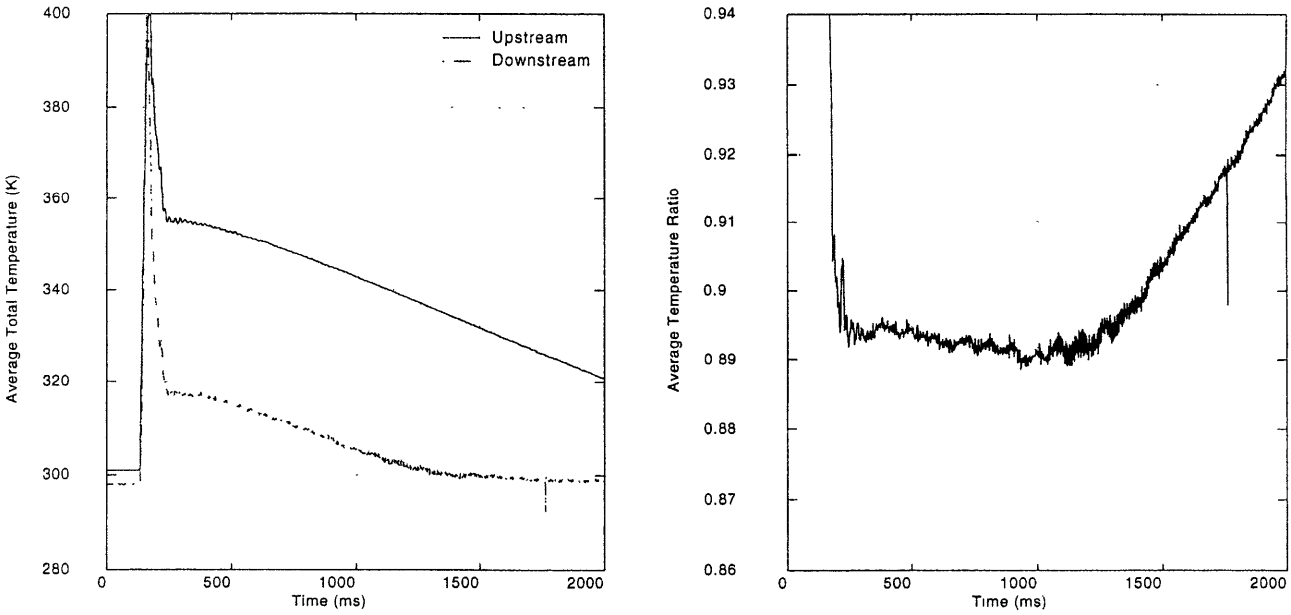

Figure A-2: Experiment 024 Average Total Temperature and Temperature Ratio

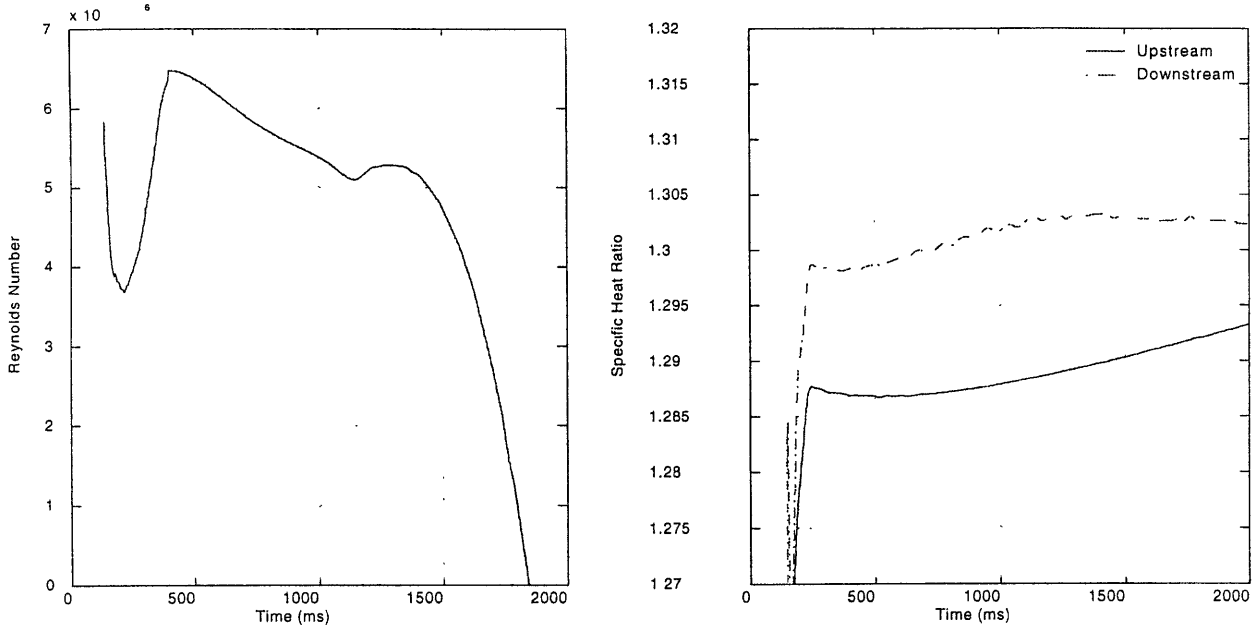

Figure A-3: Experiment 024 Reynolds Number and Specific Heat Ratio

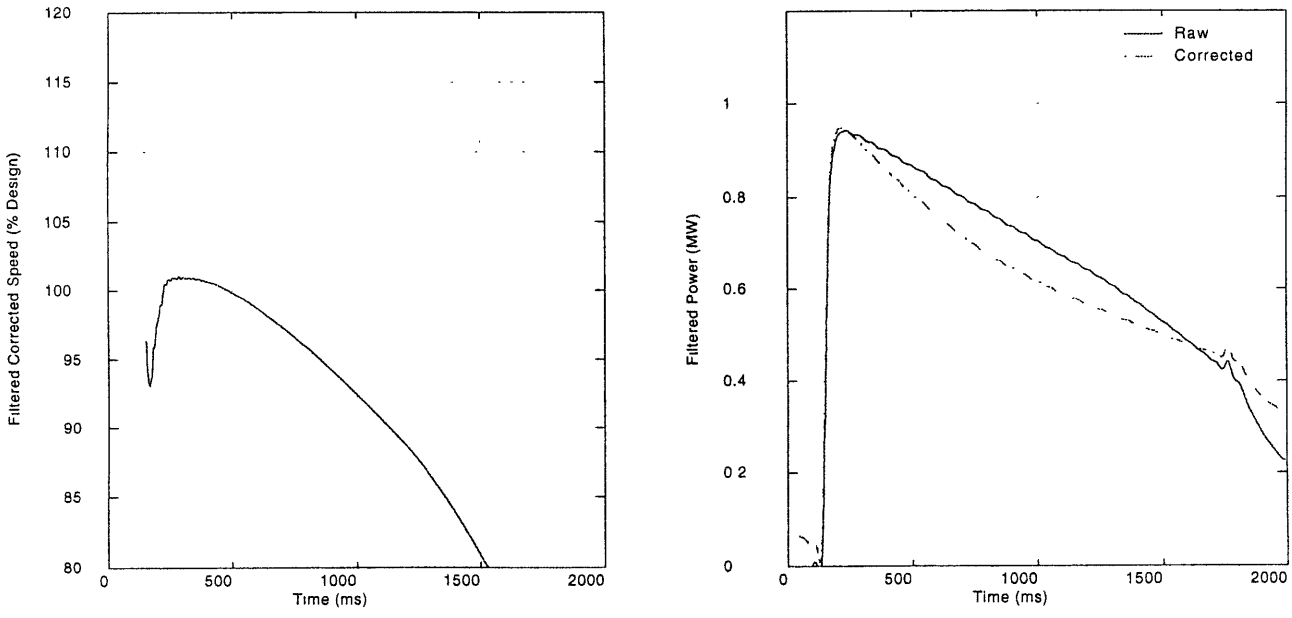

Figure A-4: Experiment 024 Corrected Speed and Power

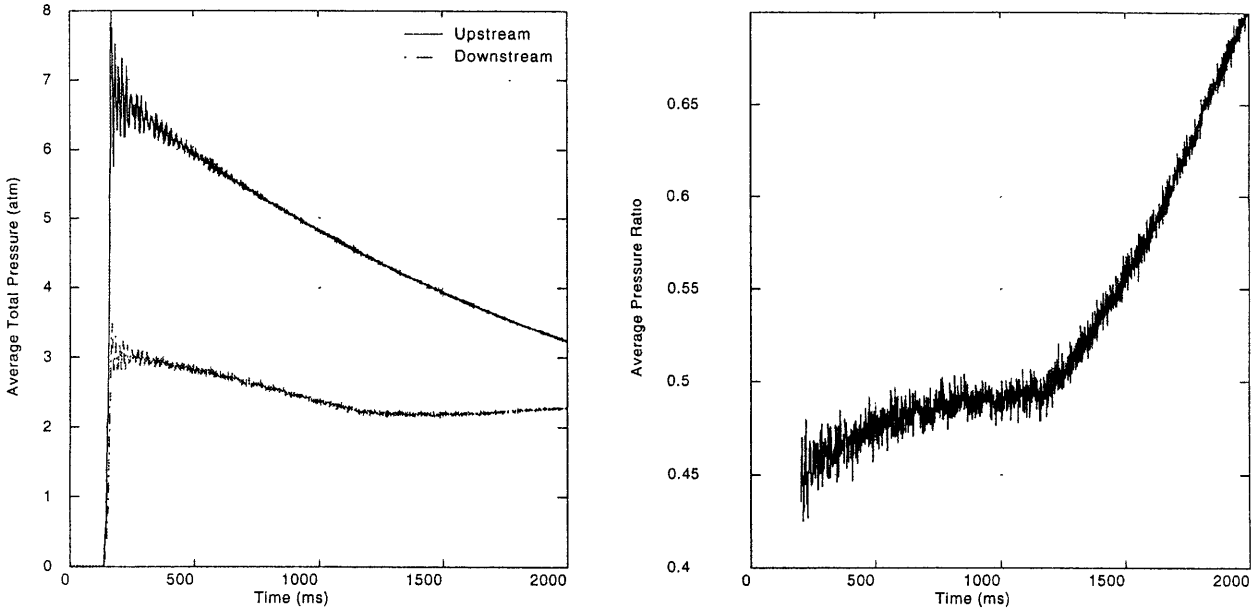

Figure A-5: Experiment 027 Average Total Pressure and Pressure Ratio

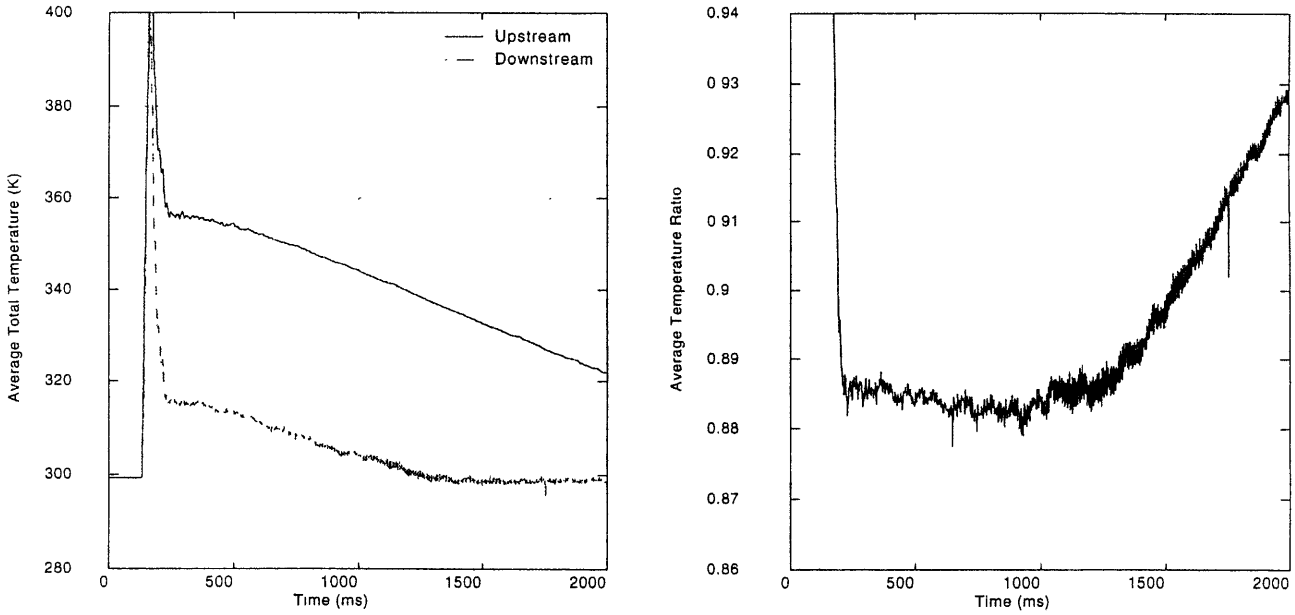

Figure A-6: Experiment 027 Average Total Temperature and Temperature Ratio

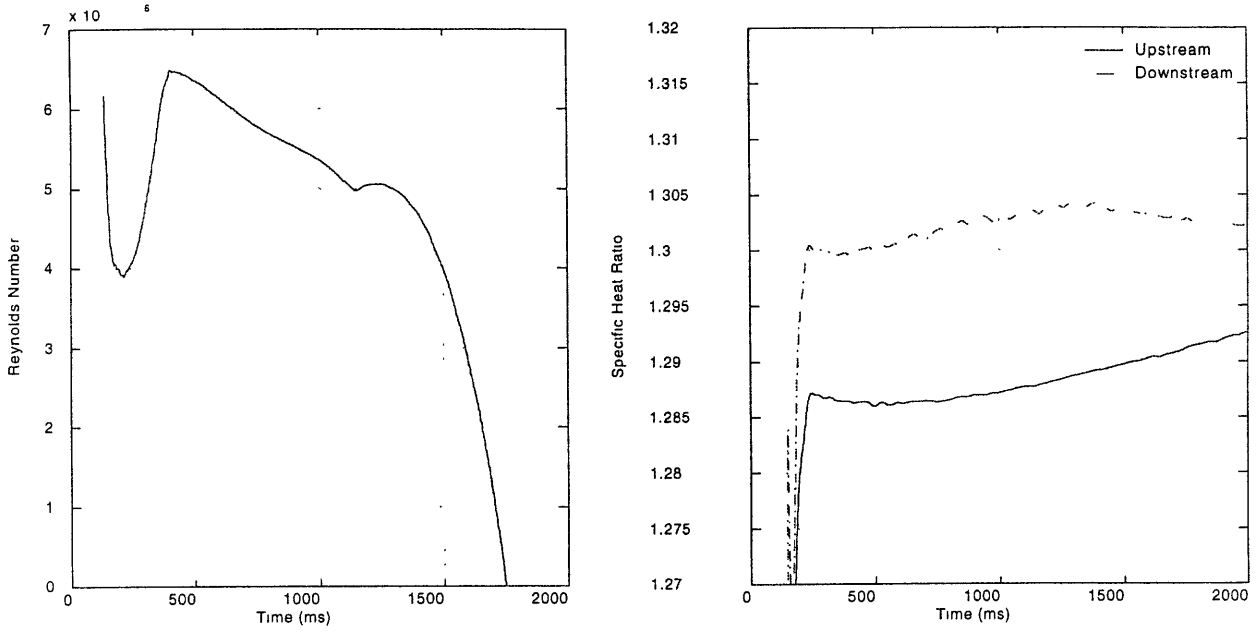

Figure A-7: Experiment 027 Reynolds Number and Specific Heat Ratio

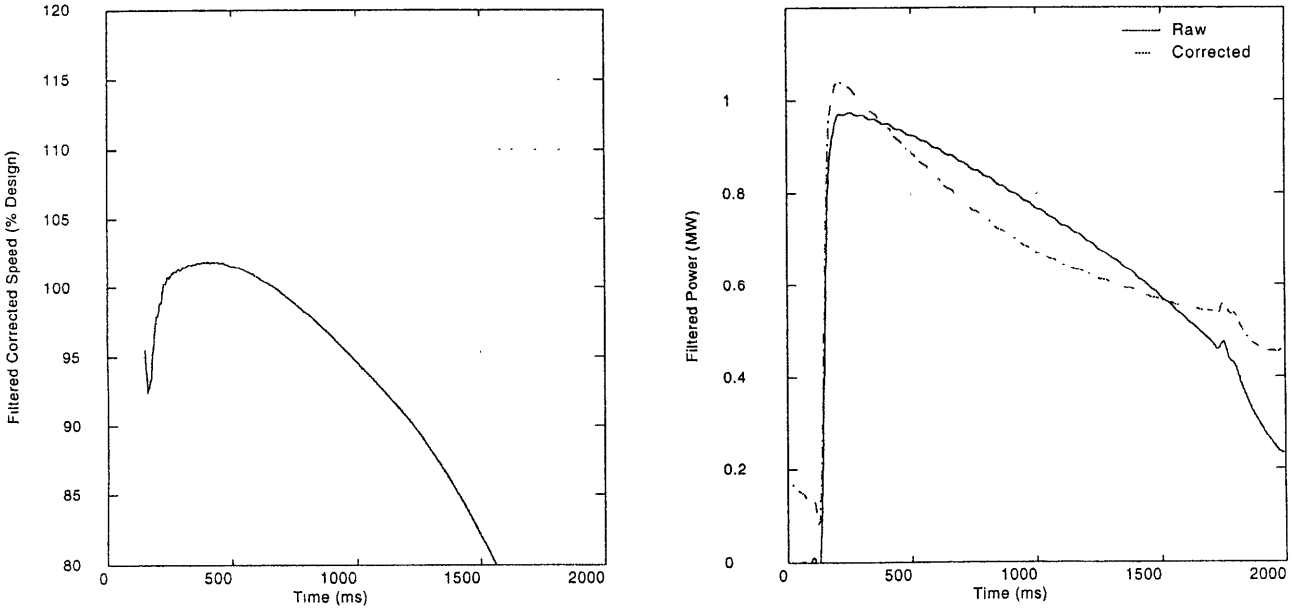

Figure A-8: Experiment 027 Corrected Speed and Power

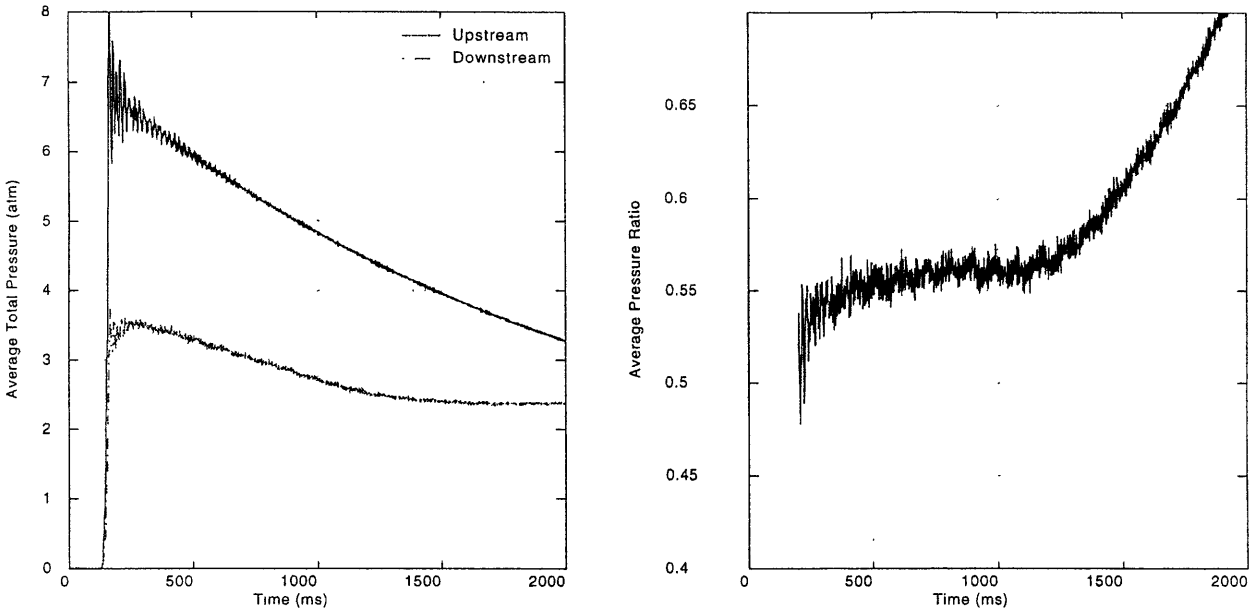

Figure A-9: Experiment 032 Average Total Pressure and Pressure Ratio

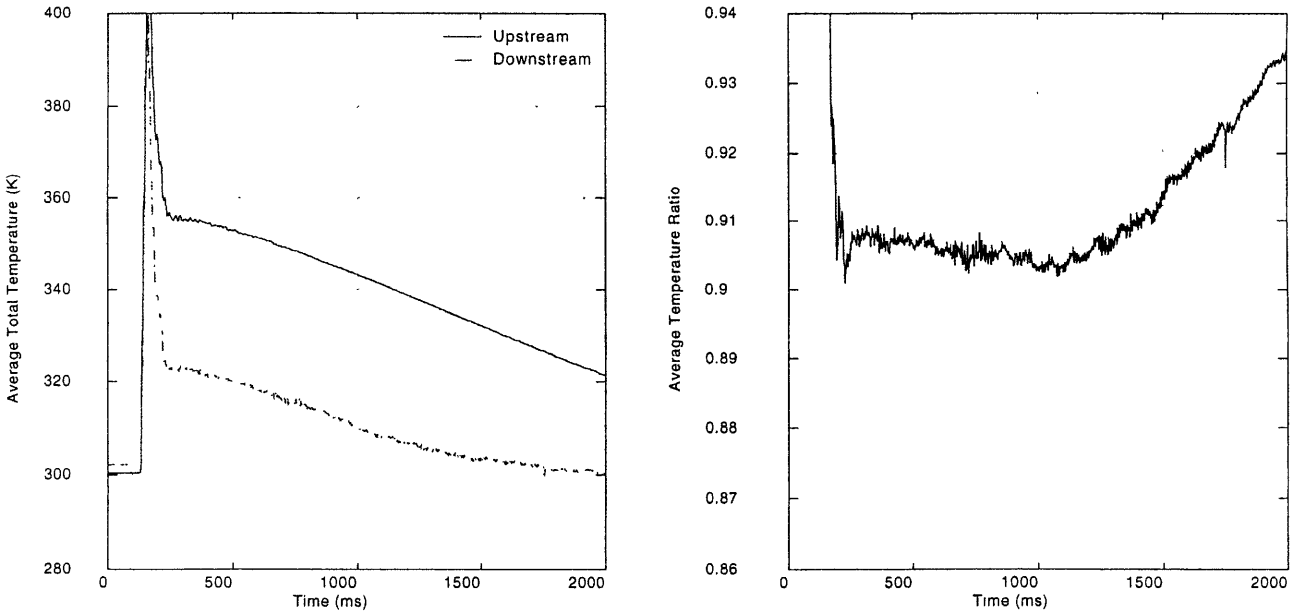

Figure A-10: Experiment 032 Average Total Temperature and Temperature Ratio

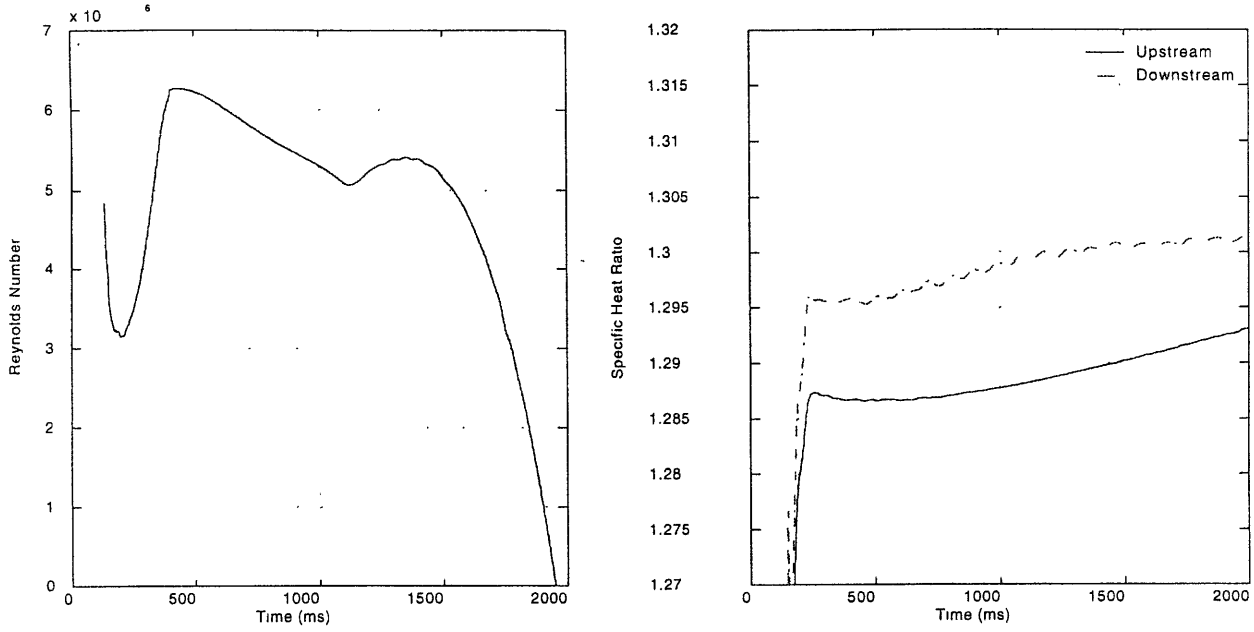

Figure A-11: Experiment 032 Reynolds Number and Specific Heat Ratio

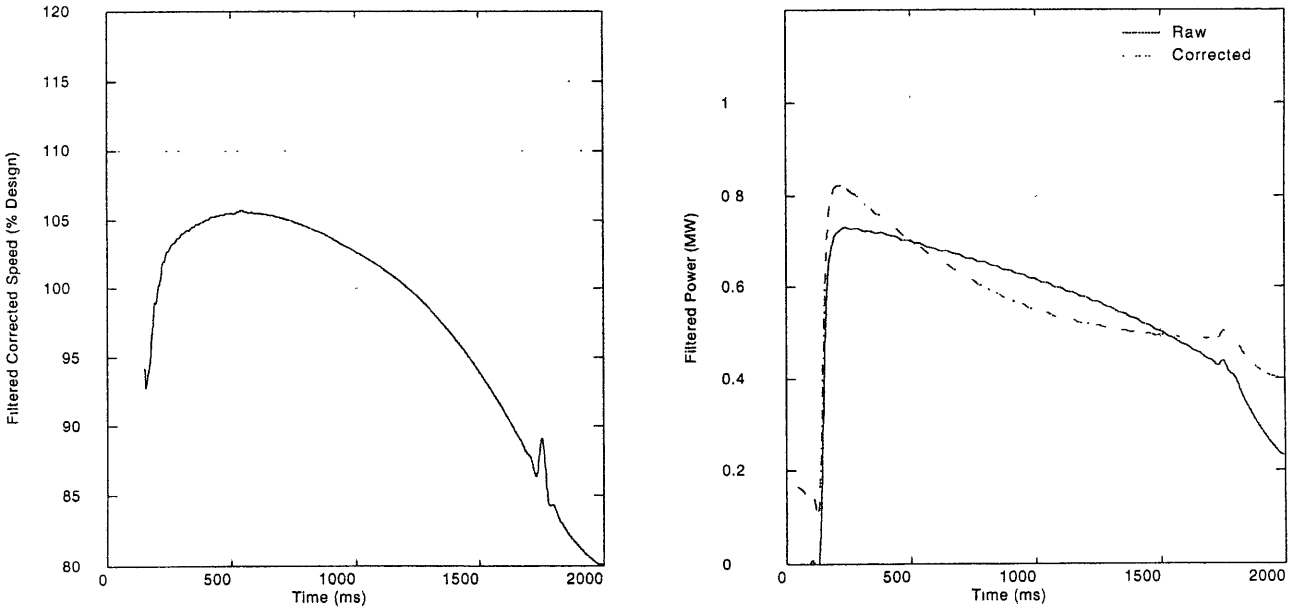

Figure A-12: Experiment 032 Corrected Speed and Power

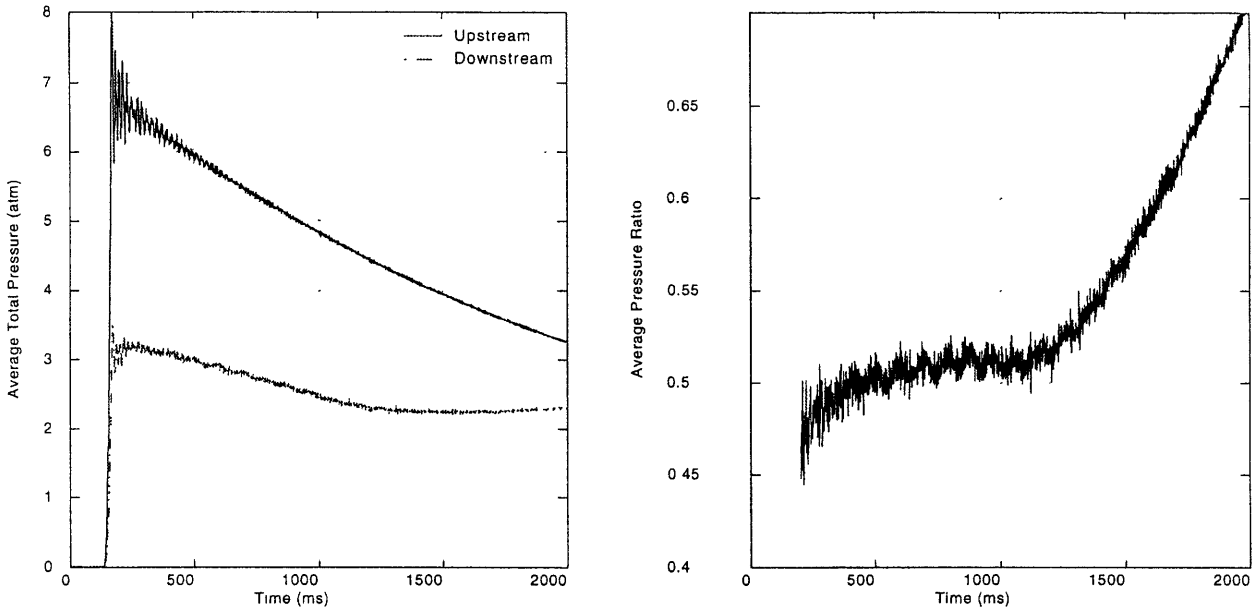

Figure A-13: Experiment 029 Average Total Pressure and Pressure Ratio

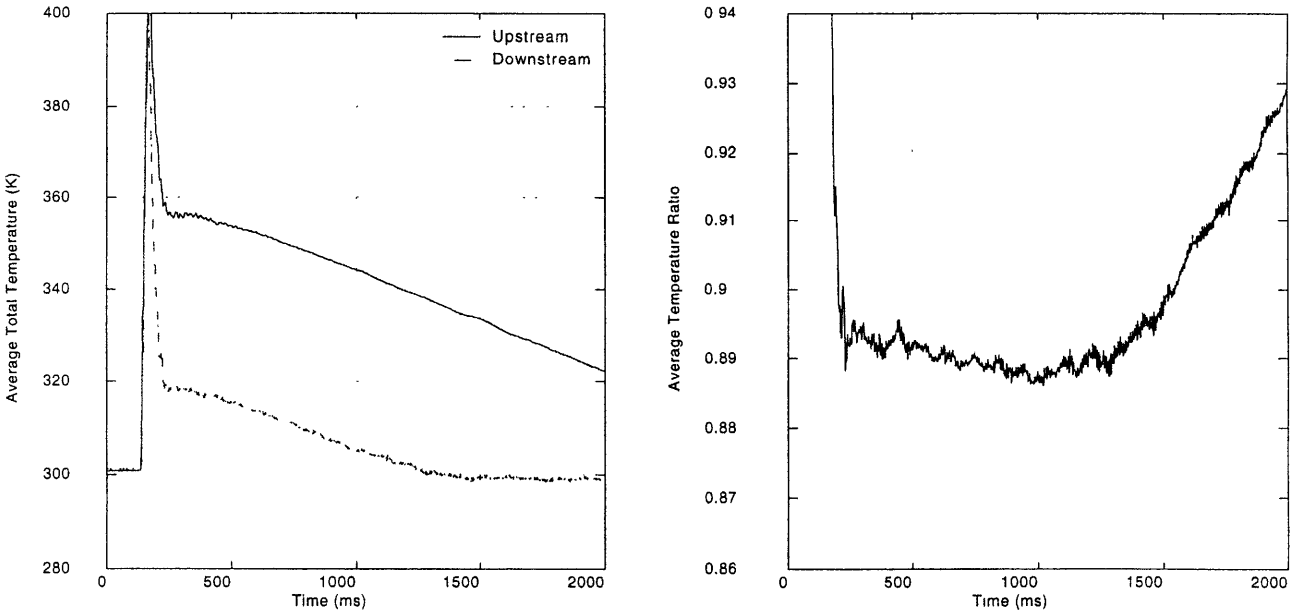

Figure A-14: Experiment 029 Average Total Temperature and Temperature Ratio

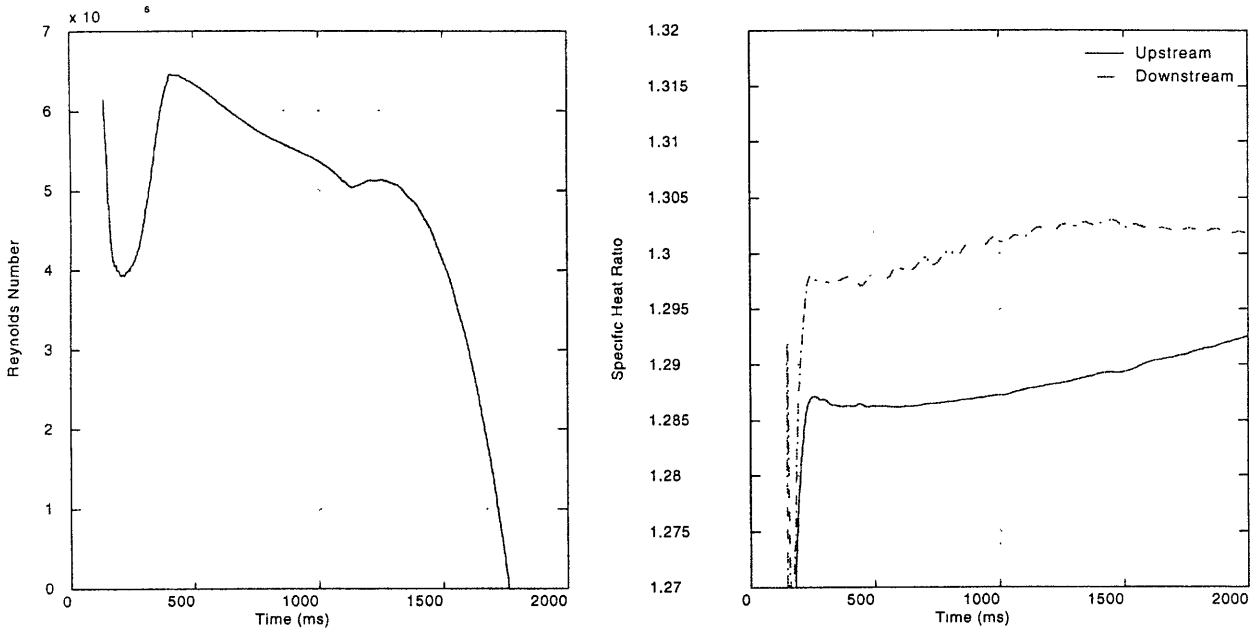

Figure A-15: Experiment 029 Reynolds Number and Specific Heat Ratio

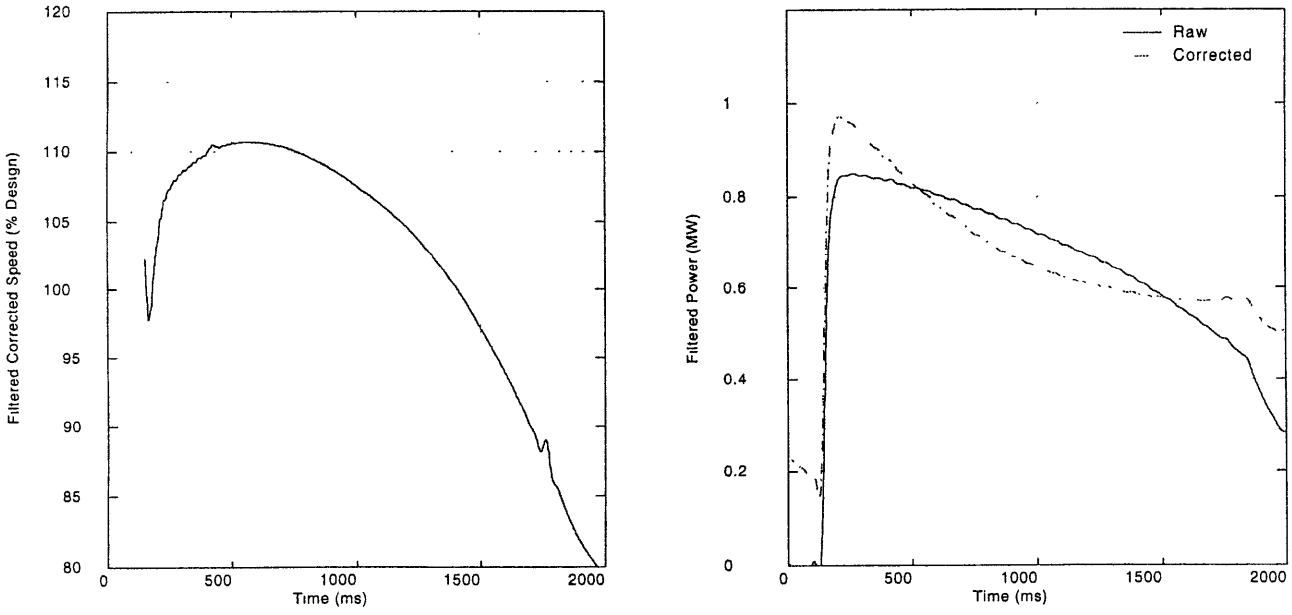

Figure A-16: Experiment 029 Corrected Speed and Power

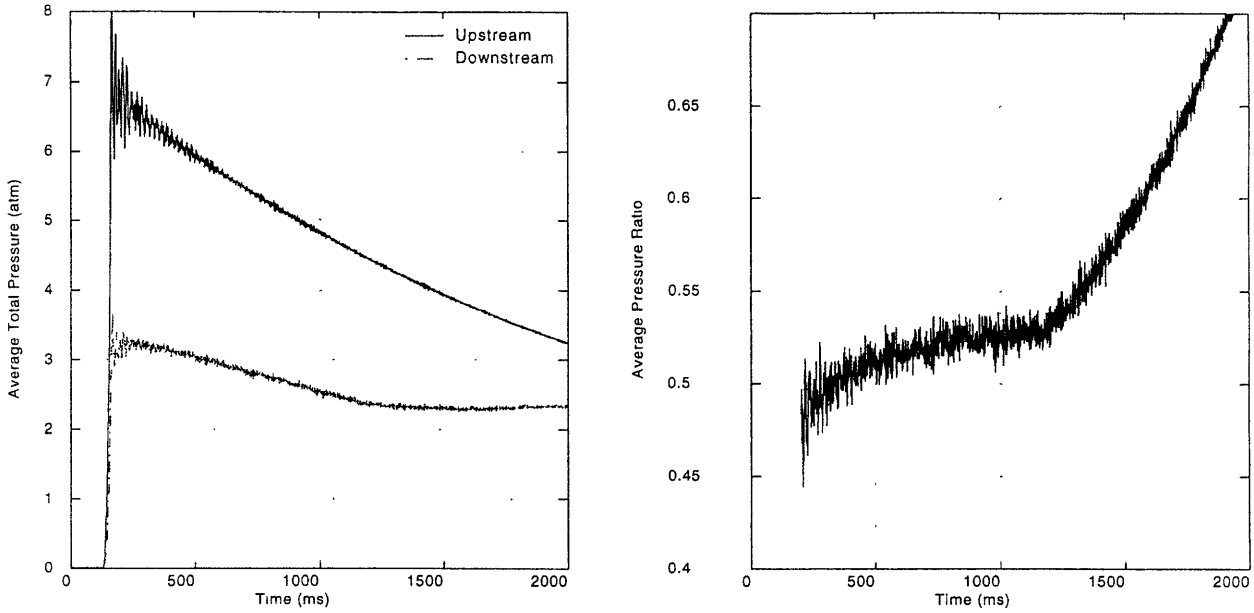

Figure A-17: Experiment 028 Average Total Pressure and Pressure Ratio

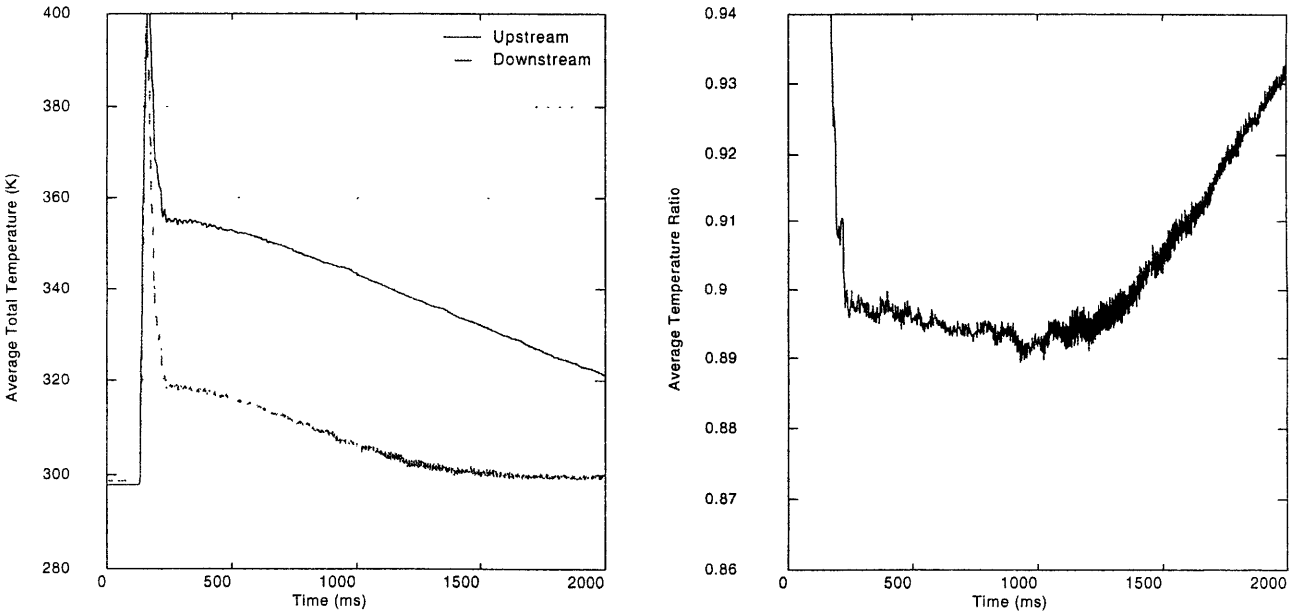

Figure A-18: Experiment 028 Average Total Temperature and Temperature Ratio

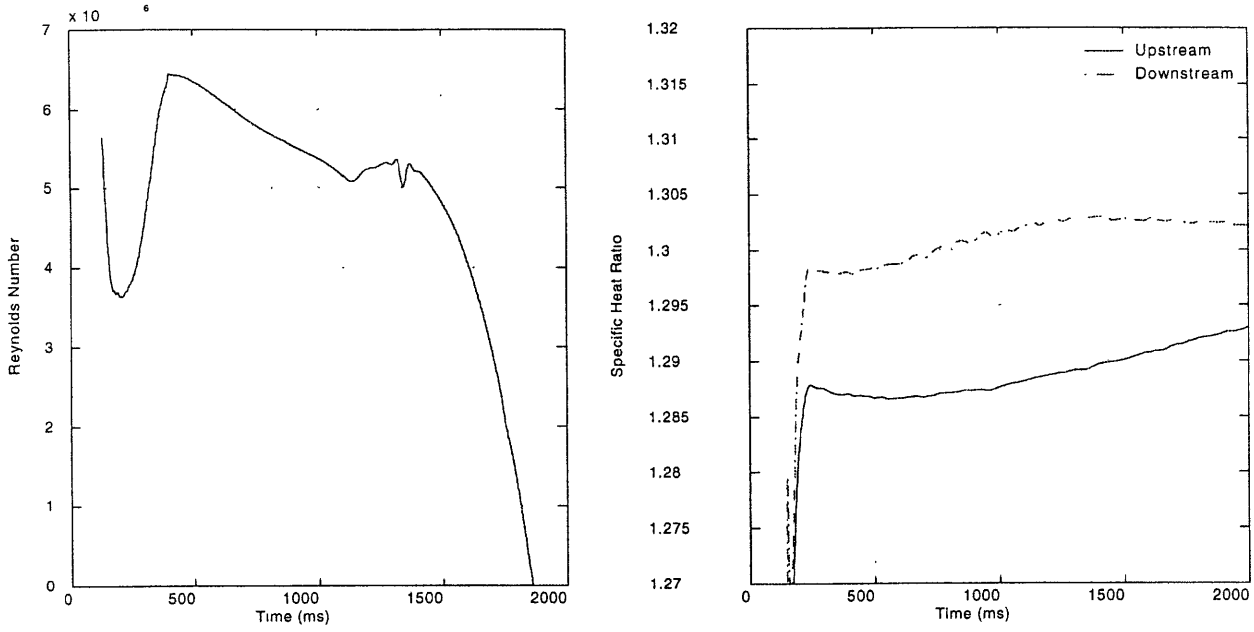

Figure A-19: Experiment 028 Reynolds Number and Specific Heat Ratio

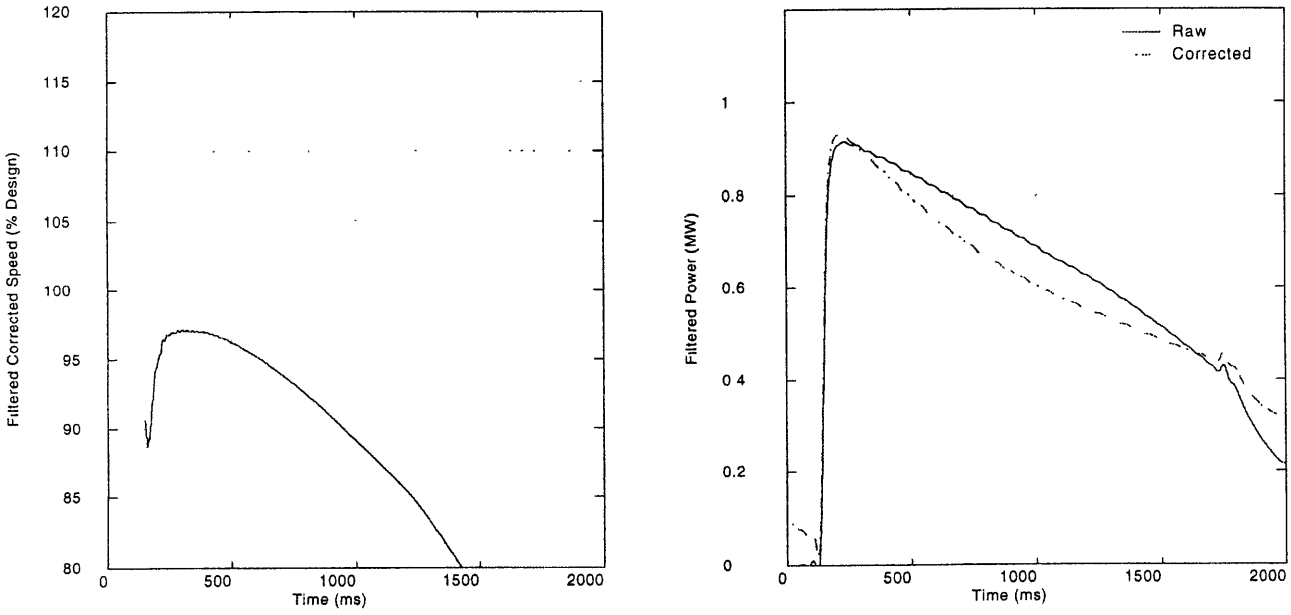

Figure A-20: Experiment 028 Corrected Speed and Power

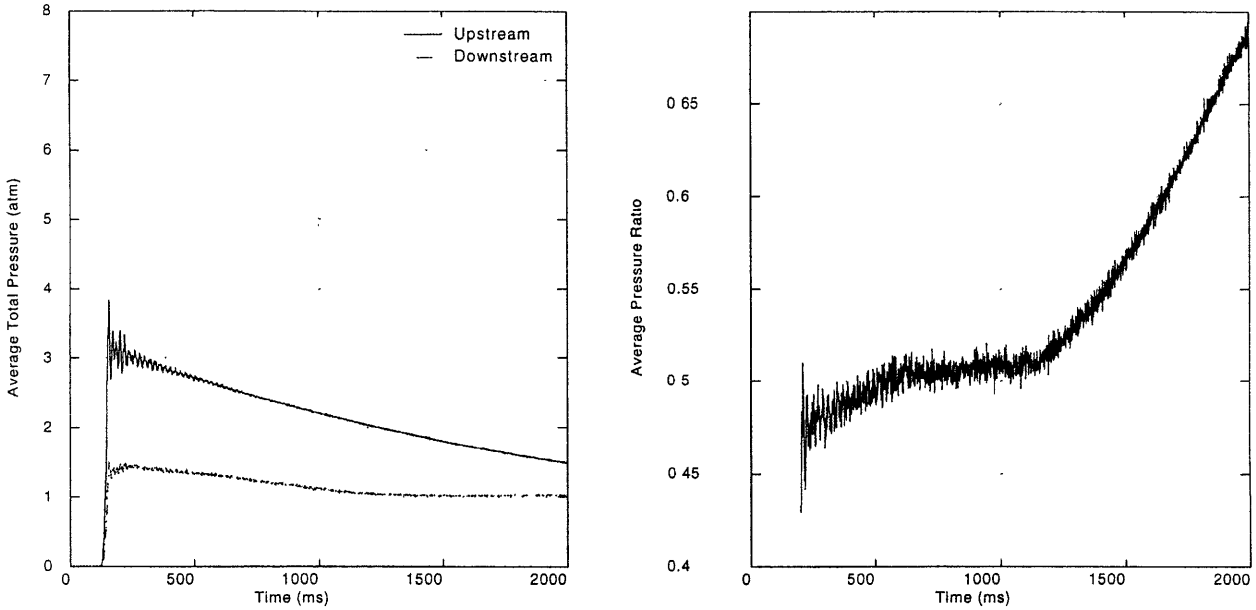

Figure A-21: Experiment 021 Average Total Pressure and Pressure Ratio

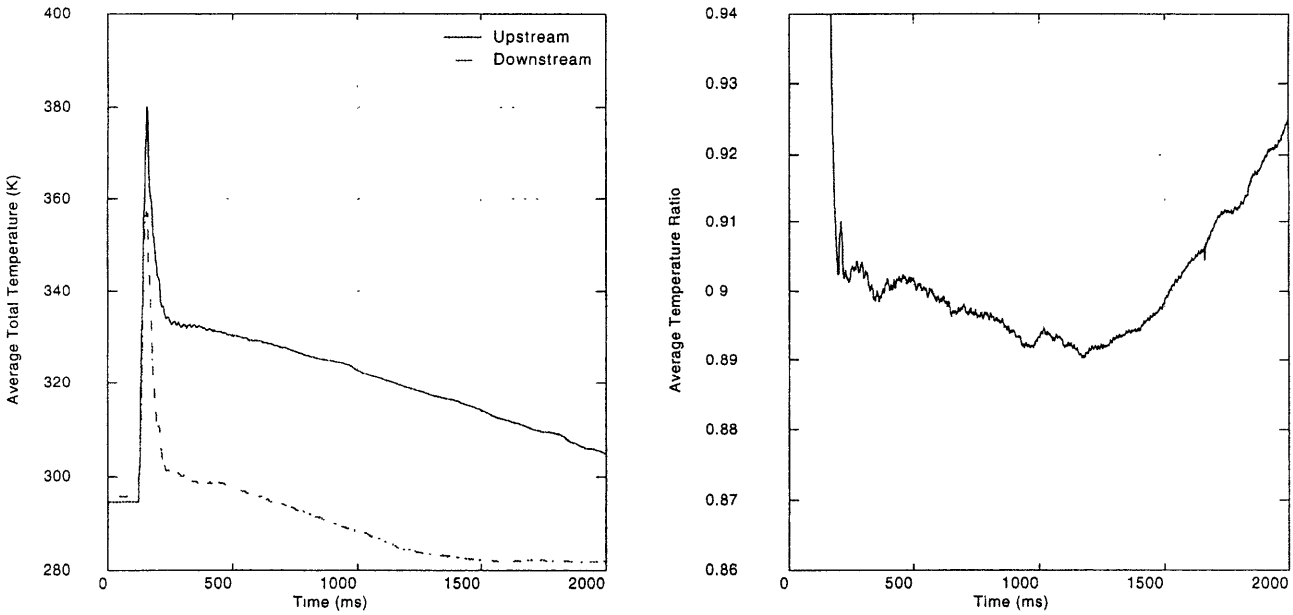

Figure A-22: Experiment 021 Average Total Temperature and Temperature Ratio

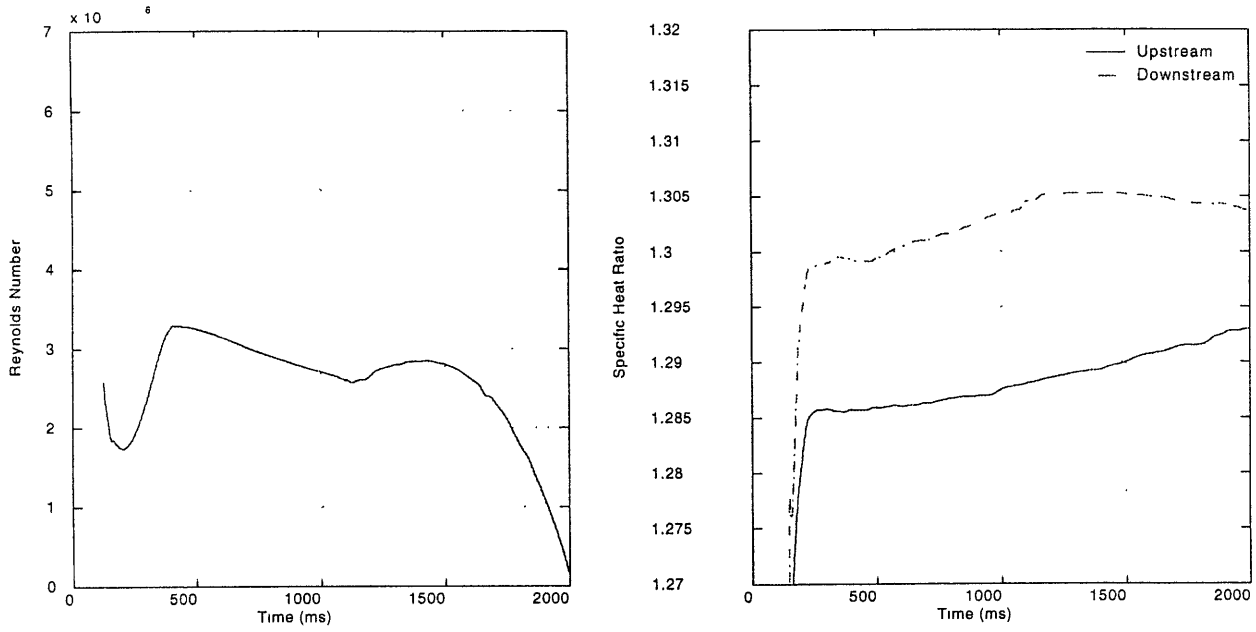

Figure A-23: Experiment 021 Reynolds Number and Specific Heat Ratio

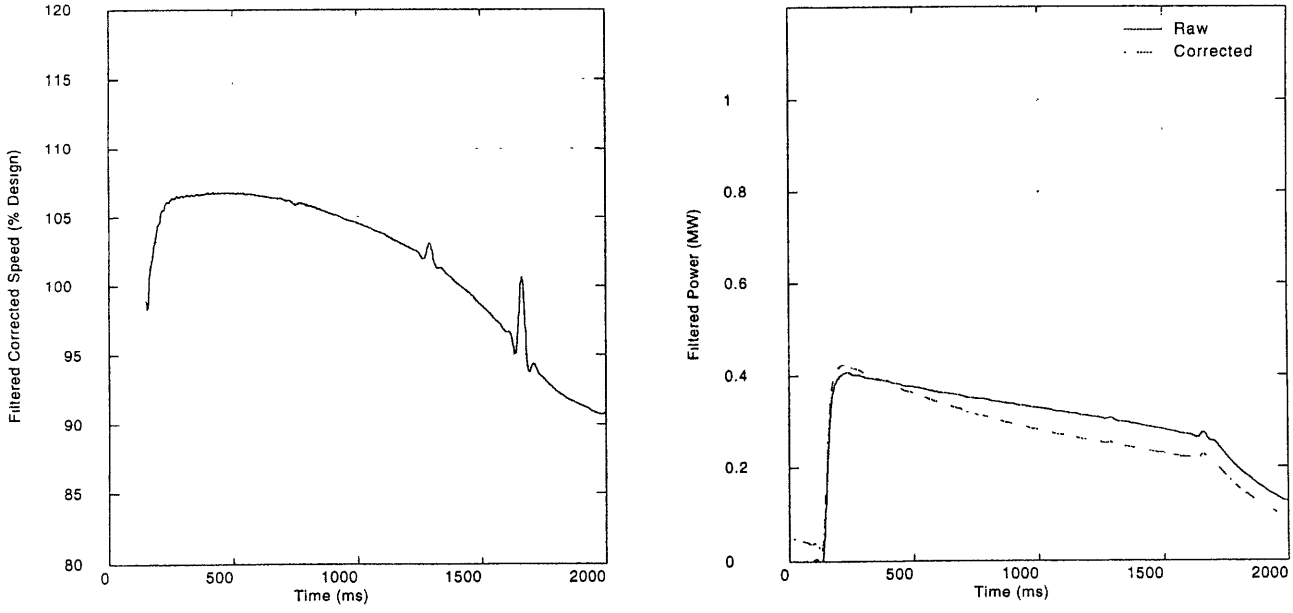

Figure A-24: Experiment 021 Corrected Speed and Power

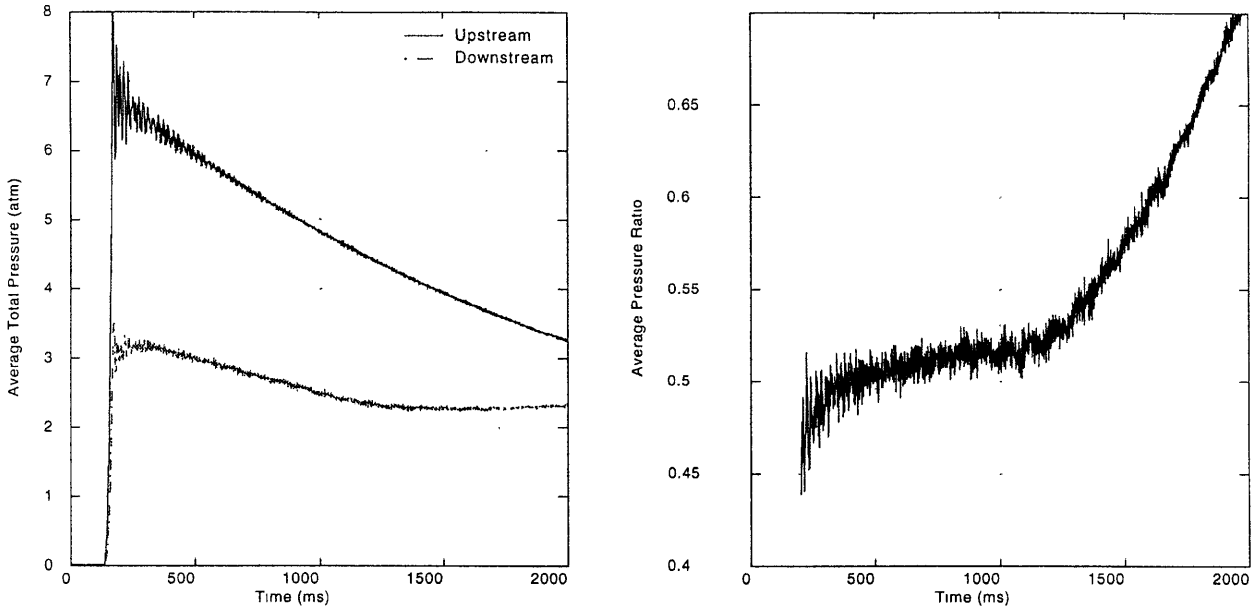

Figure A-25: Experiment 034 Average Total Pressure and Pressure Ratio

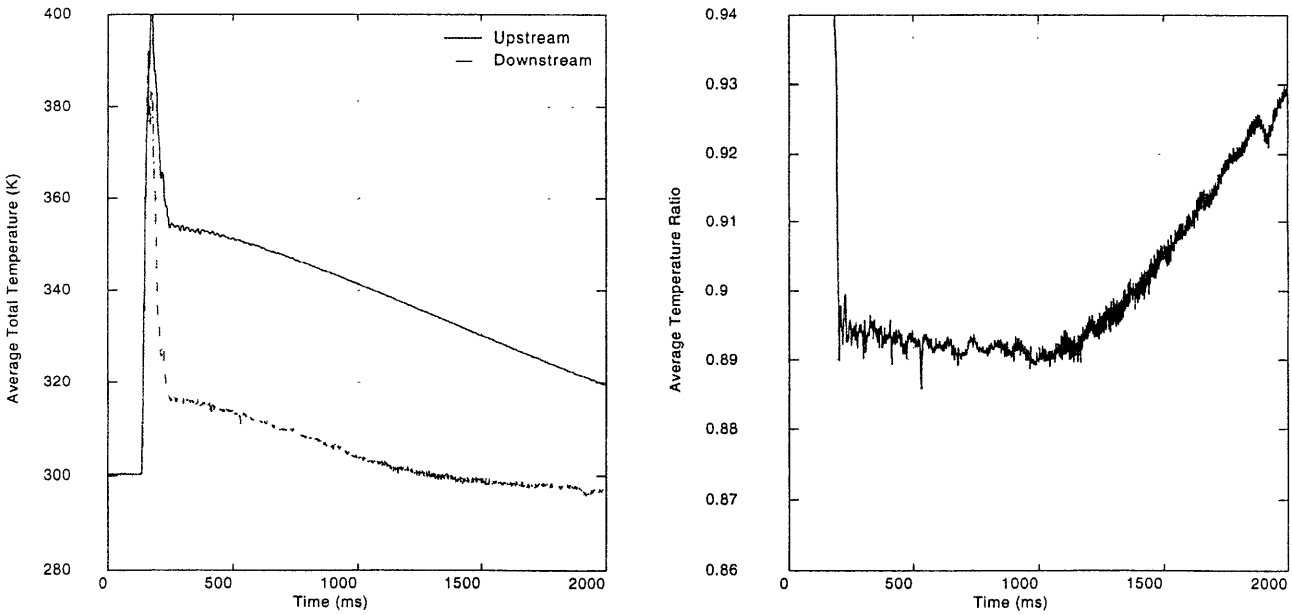

Figure A-26: Experiment 034 Average Total Temperature and Temperature Ratio

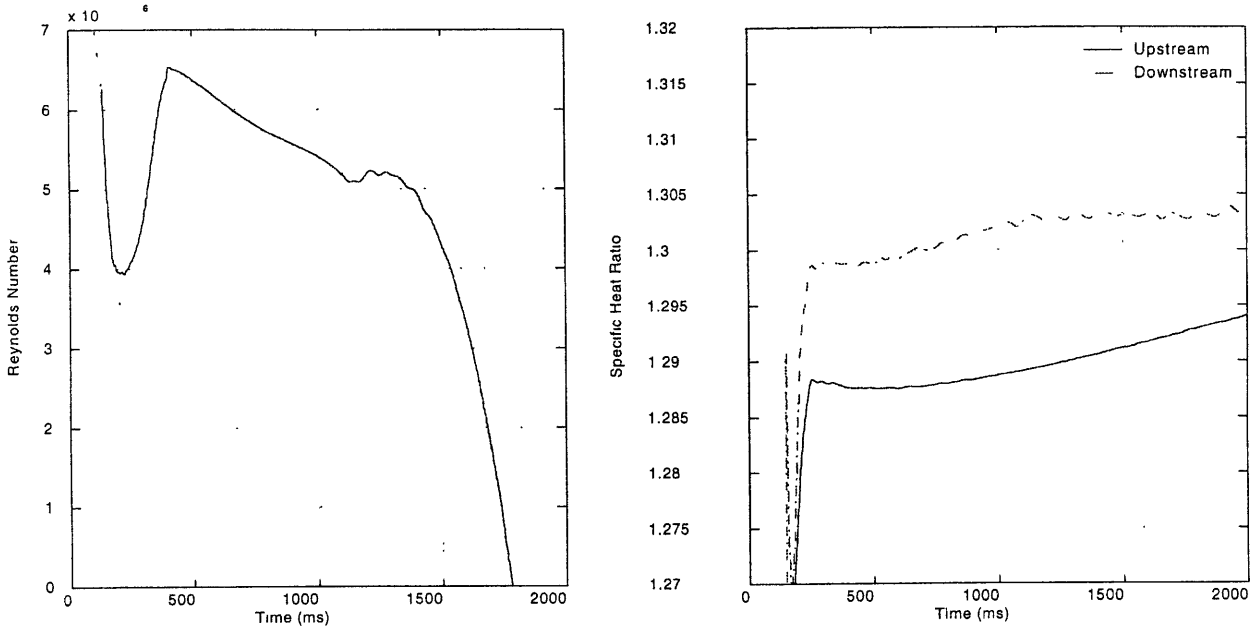

Figure A-27: Experiment 034 Reynolds Number and Specific Heat Ratio

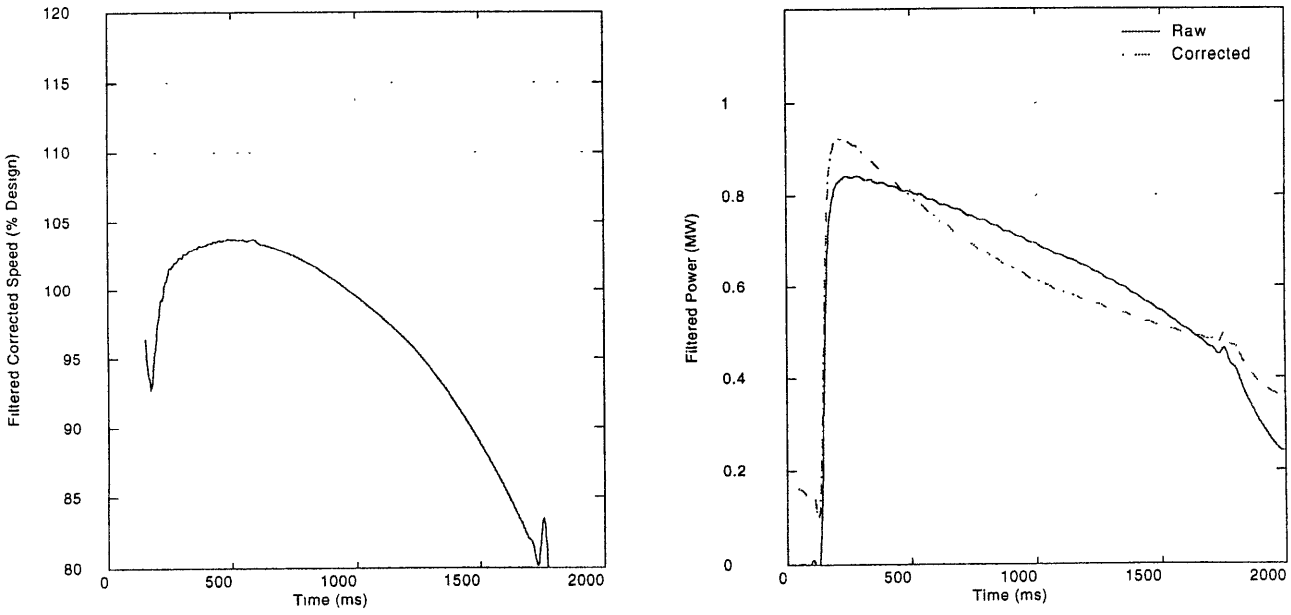

Figure A-28: Experiment 034 Corrected Speed and Power

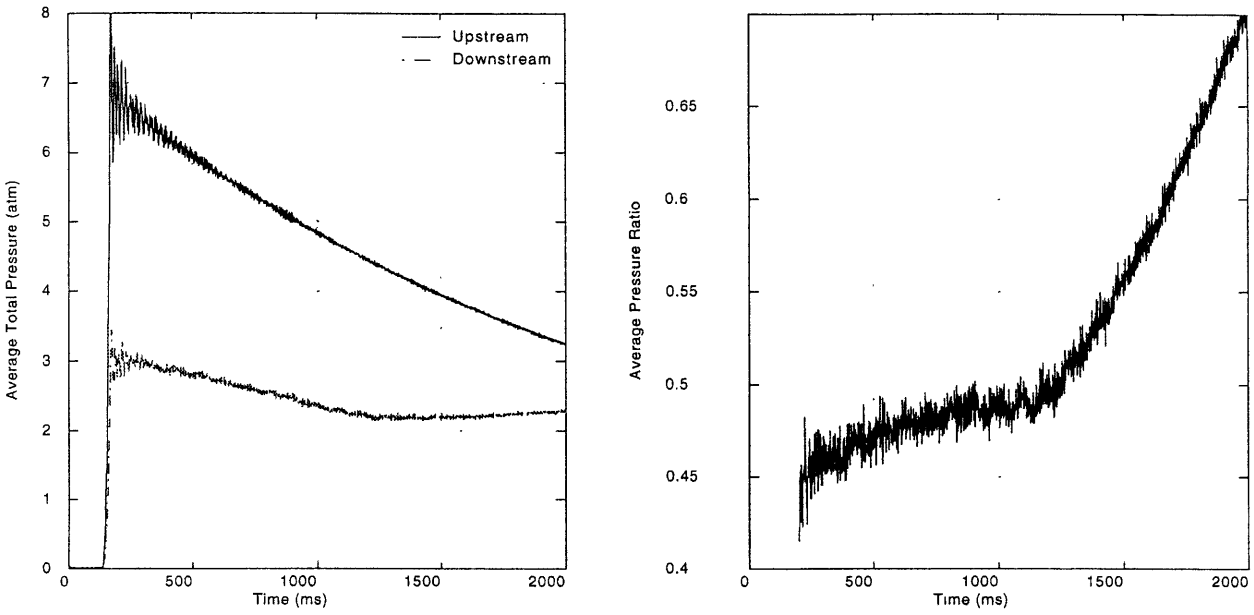

Figure A-29: Experiment 035 Average Total Pressure and Pressure Ratio

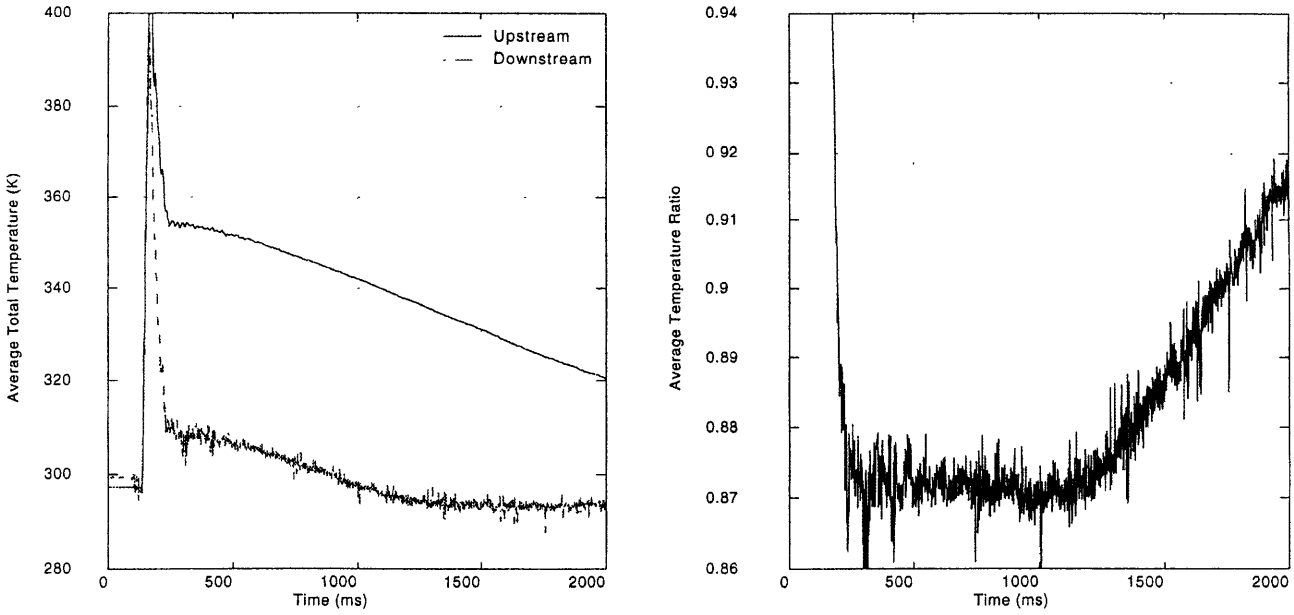

Figure A-30: Experiment 035 Average Total Temperature and Temperature Ratio

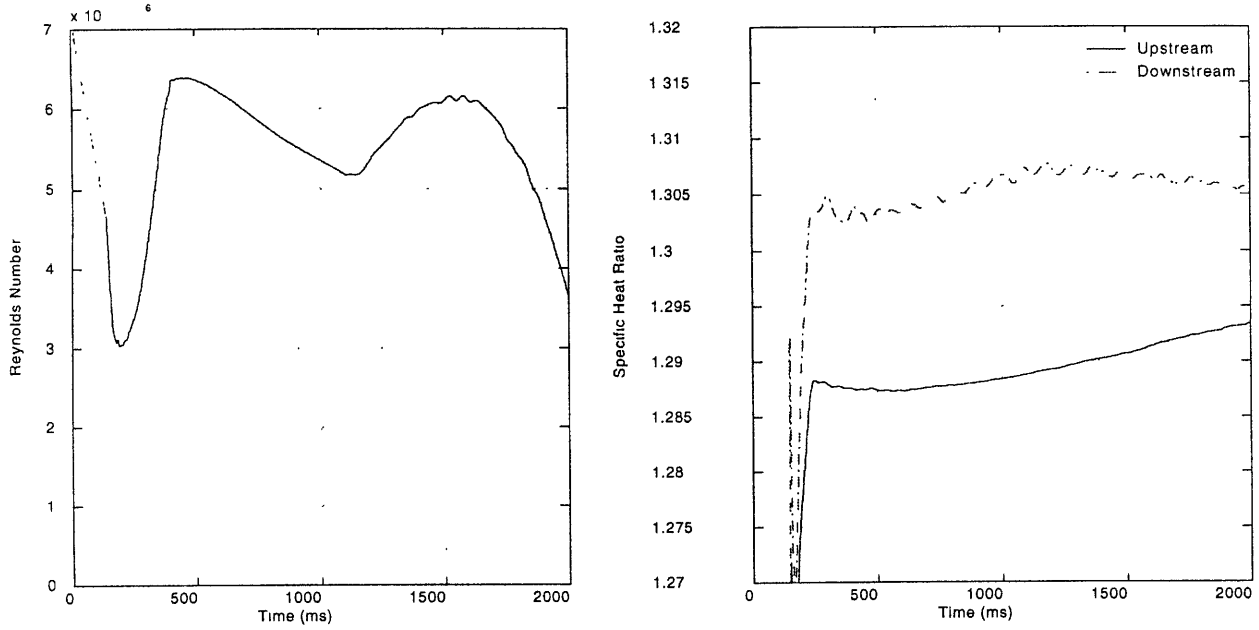

Figure A-31: Experiment 035 Reynolds Number and Specific Heat Ratio

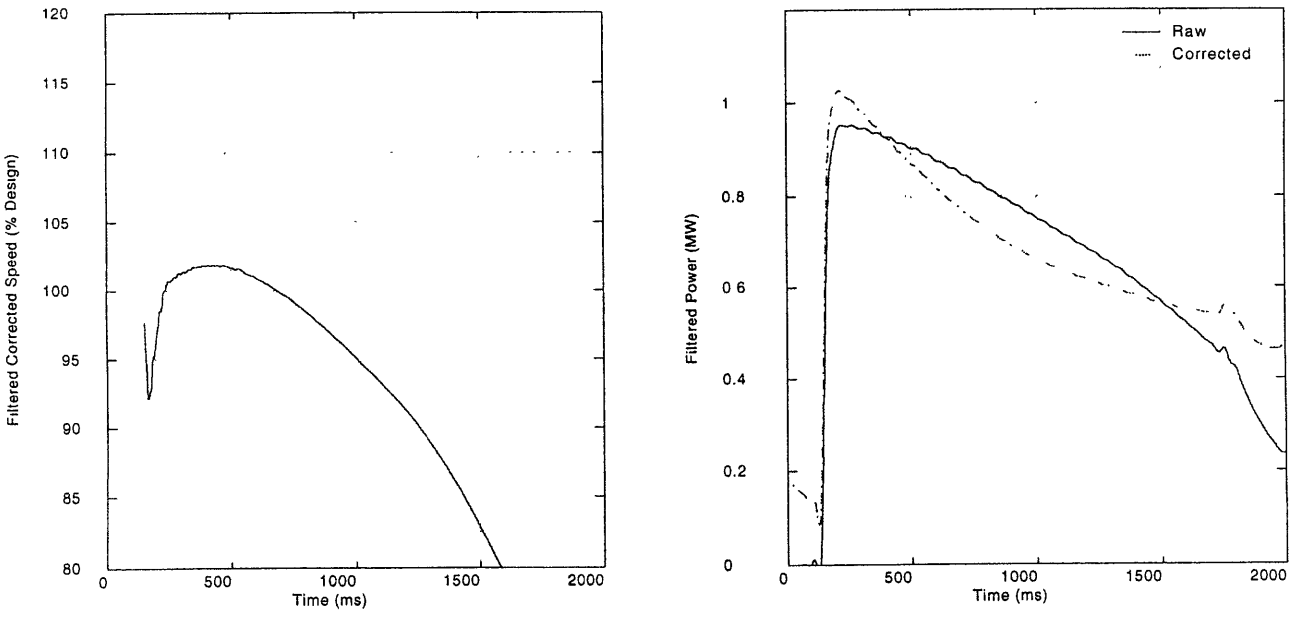

Figure A-32: Experiment 035 Corrected Speed and Power

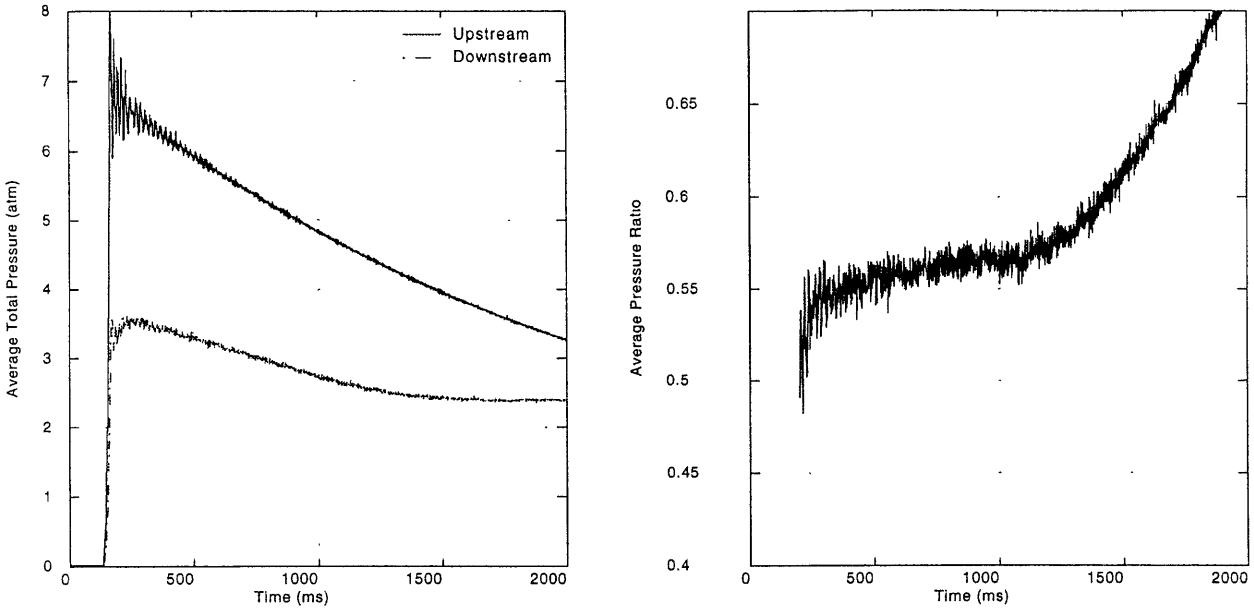

Figure A-33: Experiment 033 Average Total Pressure and Pressure Ratio

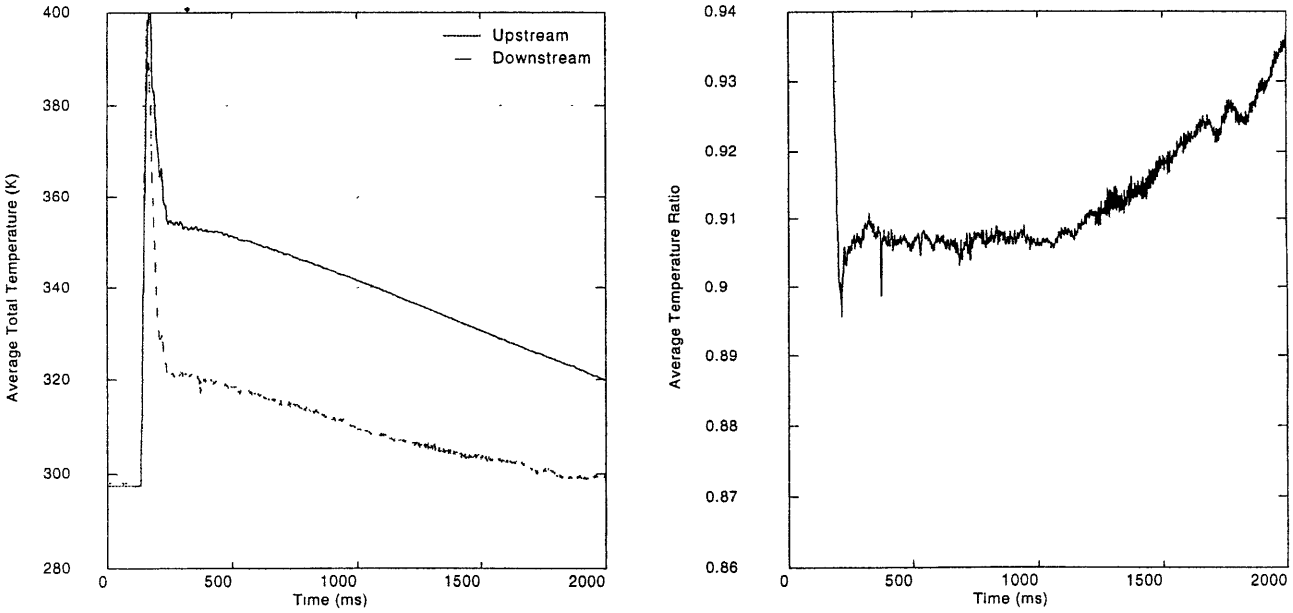

Figure A-34: Experiment 033 Average Total Temperature and Temperature Ratio

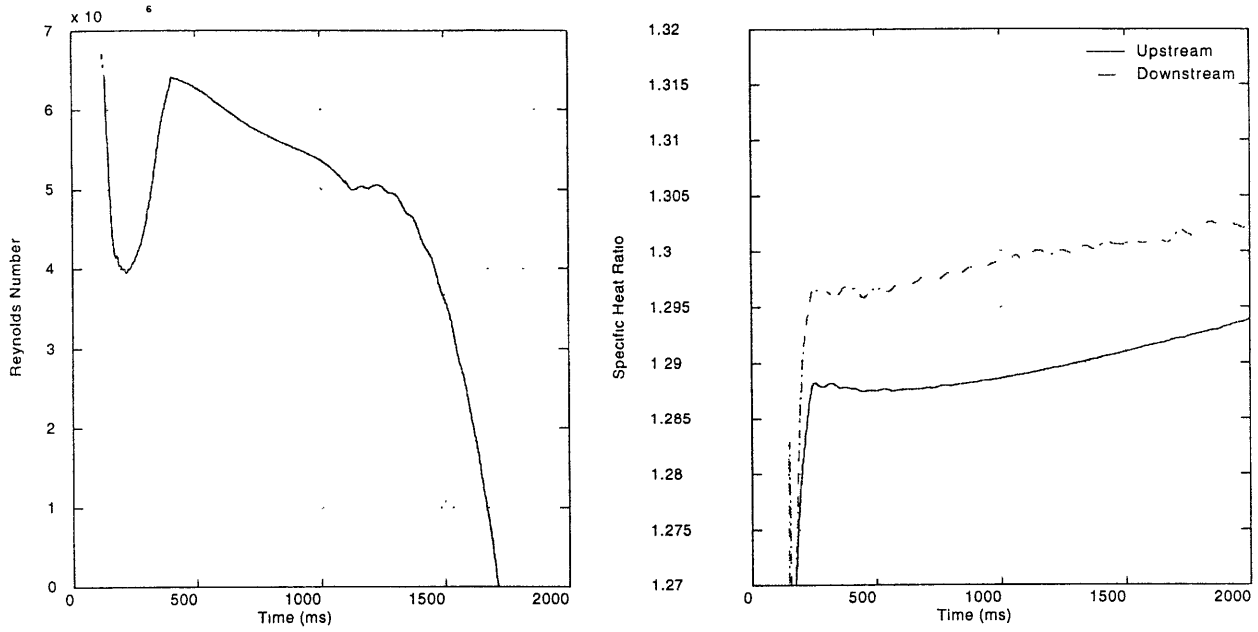

Figure A-35: Experiment 033 Reynolds Number and Specific Heat Ratio

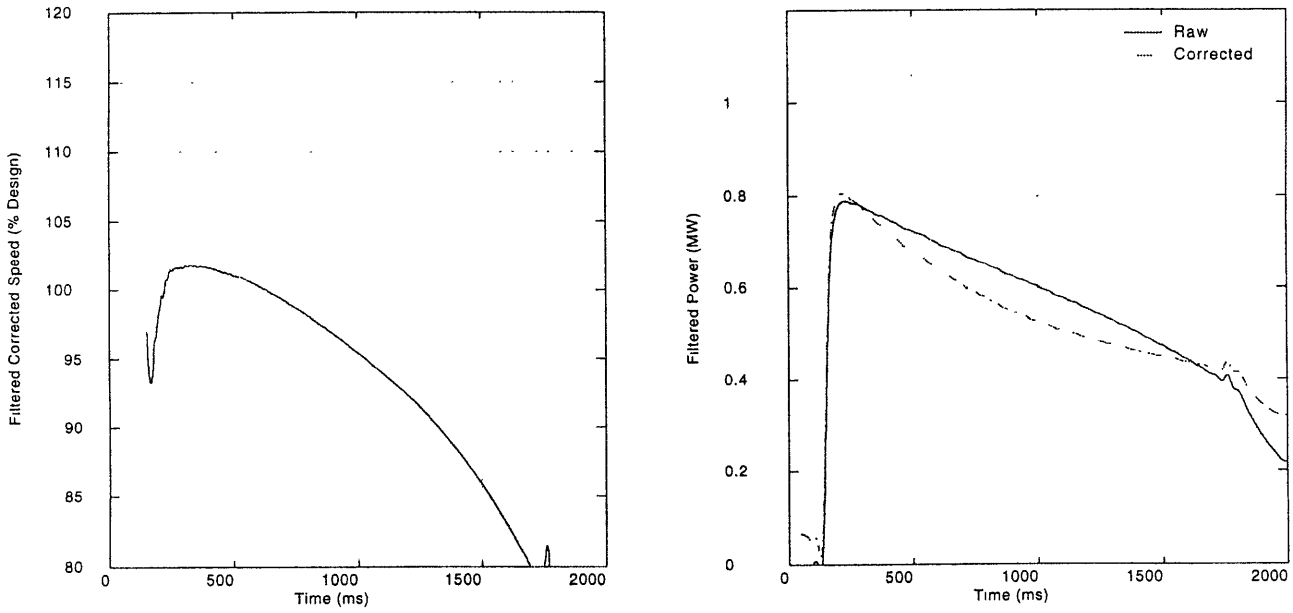

Figure A-36: Experiment 033 Corrected Speed and Power

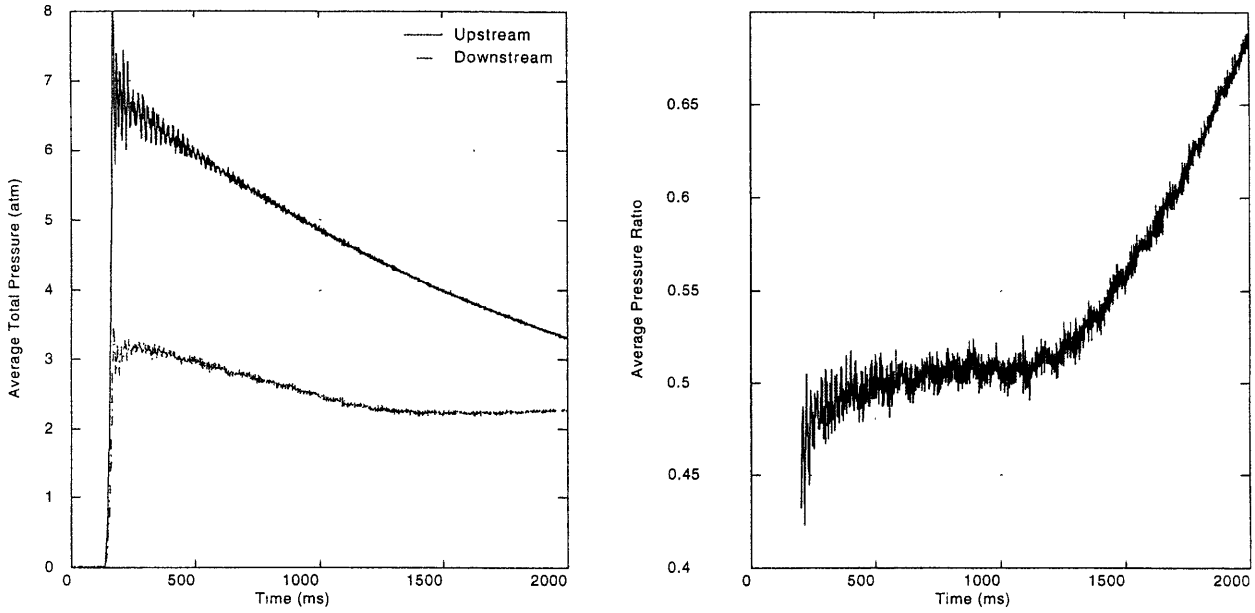

Figure A-37: Experiment 037 Average Total Pressure and Pressure Ratio

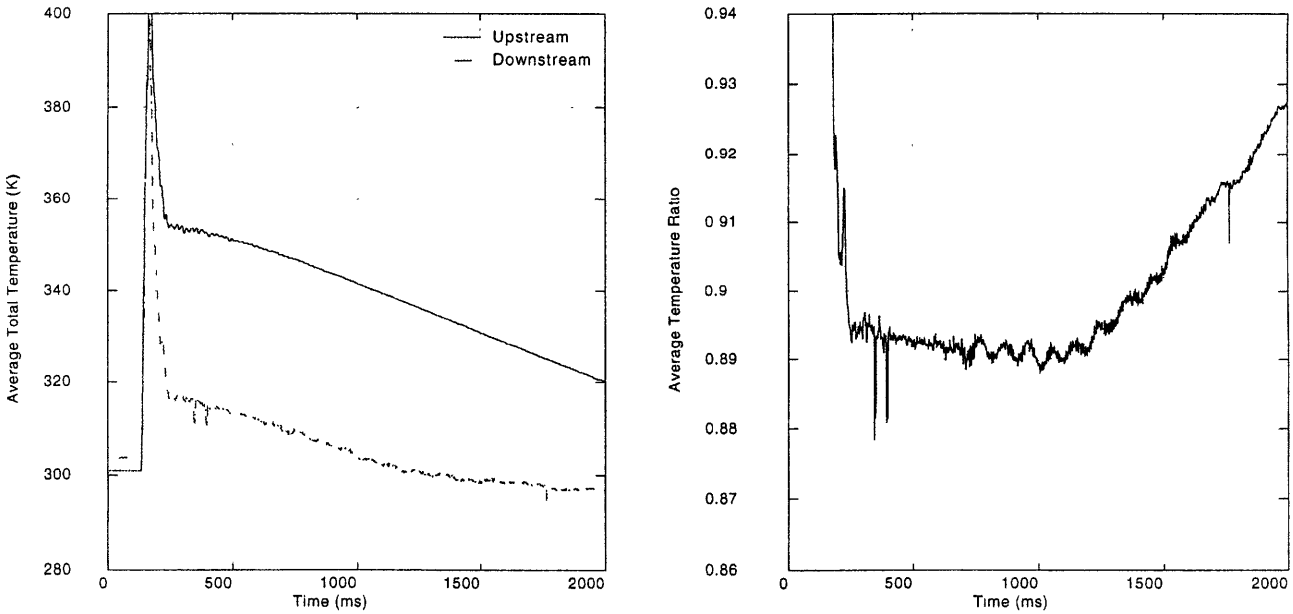

Figure A-38: Experiment 037 Average Total Temperature and Temperature Ratio

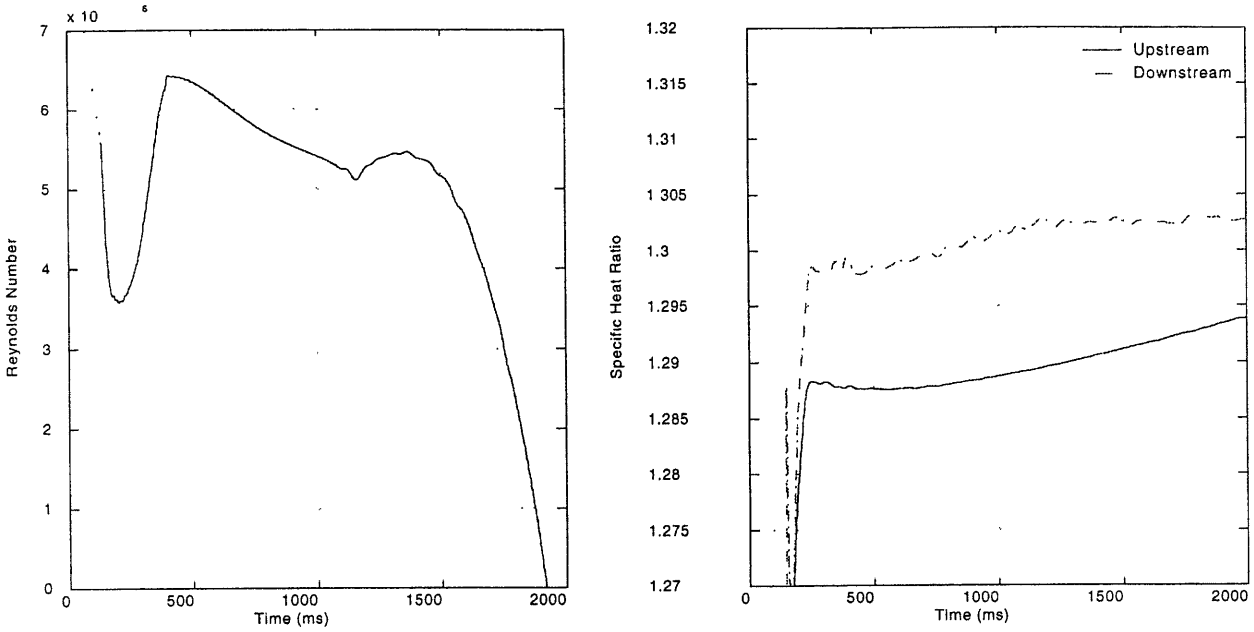

Figure A-39: Experiment 037 Reynolds Number and Specific Heat Ratio

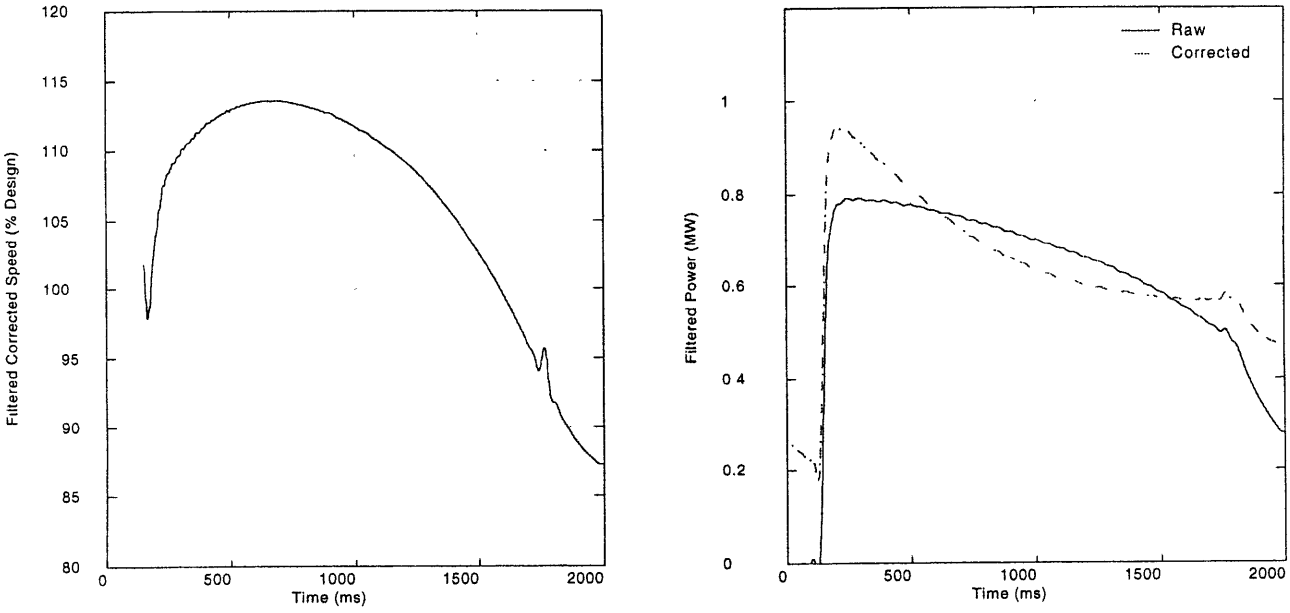

Figure A-40: Experiment 037 Corrected Speed and Power

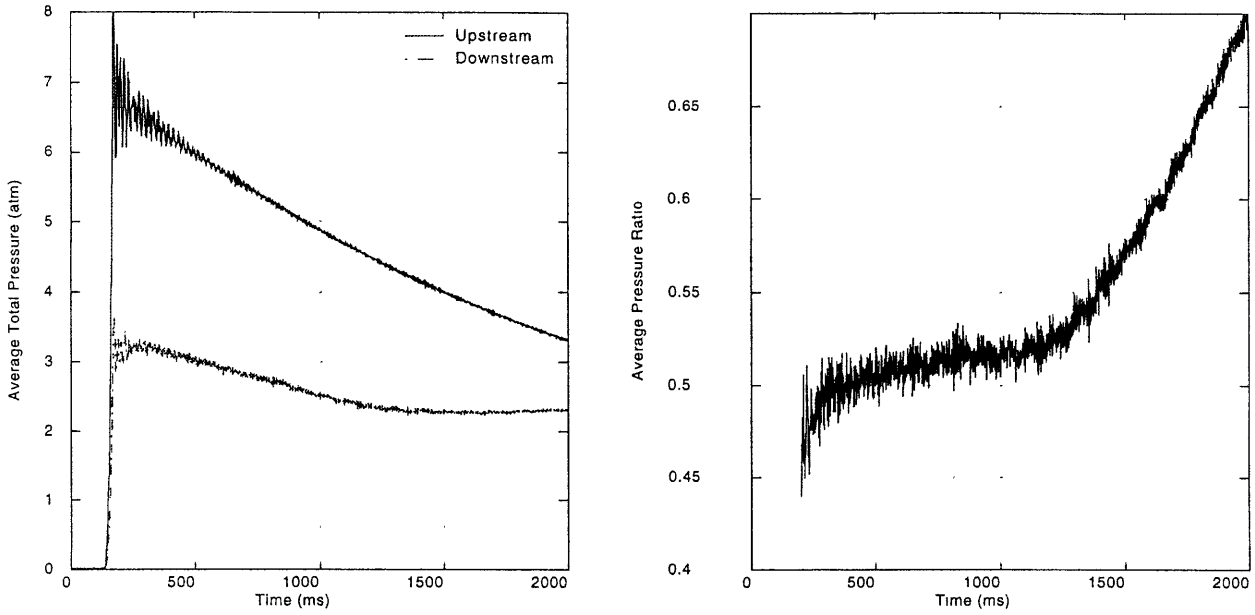

Figure A-41: Experiment 036 Average Total Pressure and Pressure Ratio

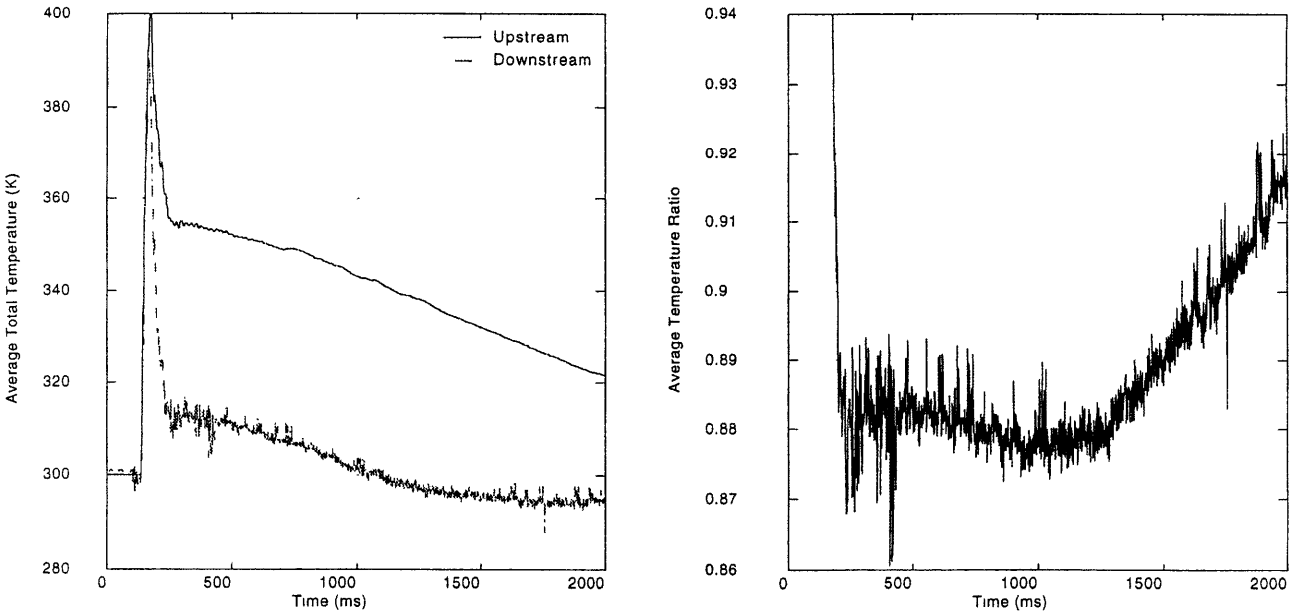

Figure A-42: Experiment 036 Average Total Temperature and Temperature Ratio

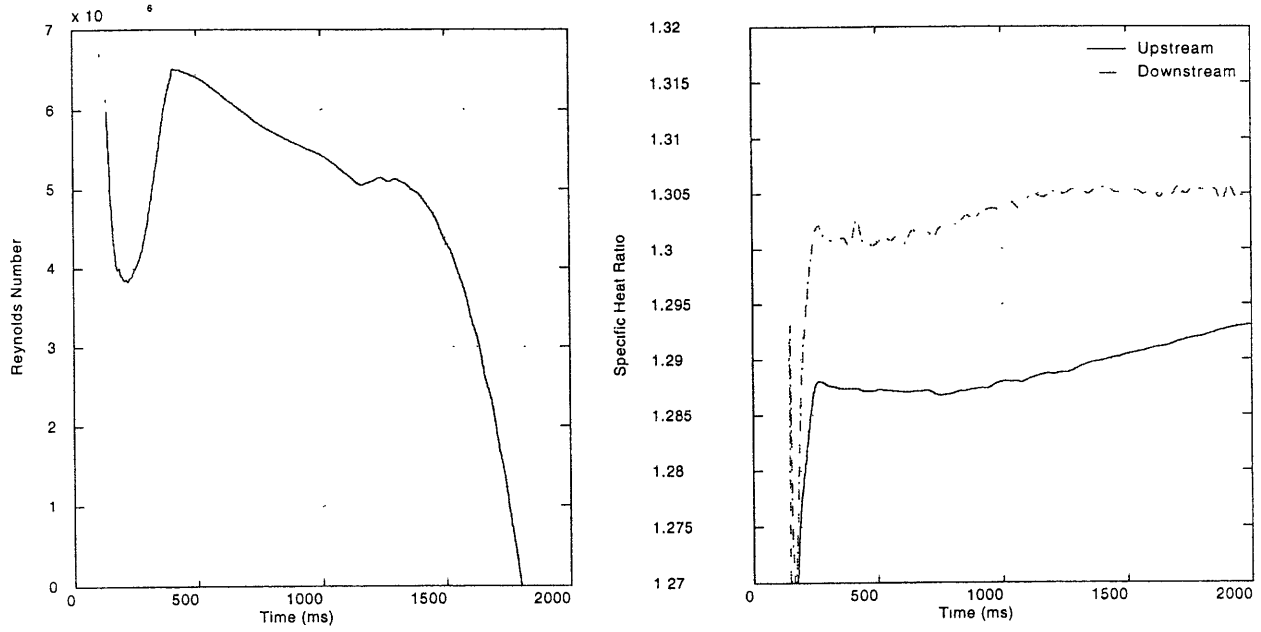

Figure A-43: Experiment 036 Reynolds Number and Specific Heat Ratio

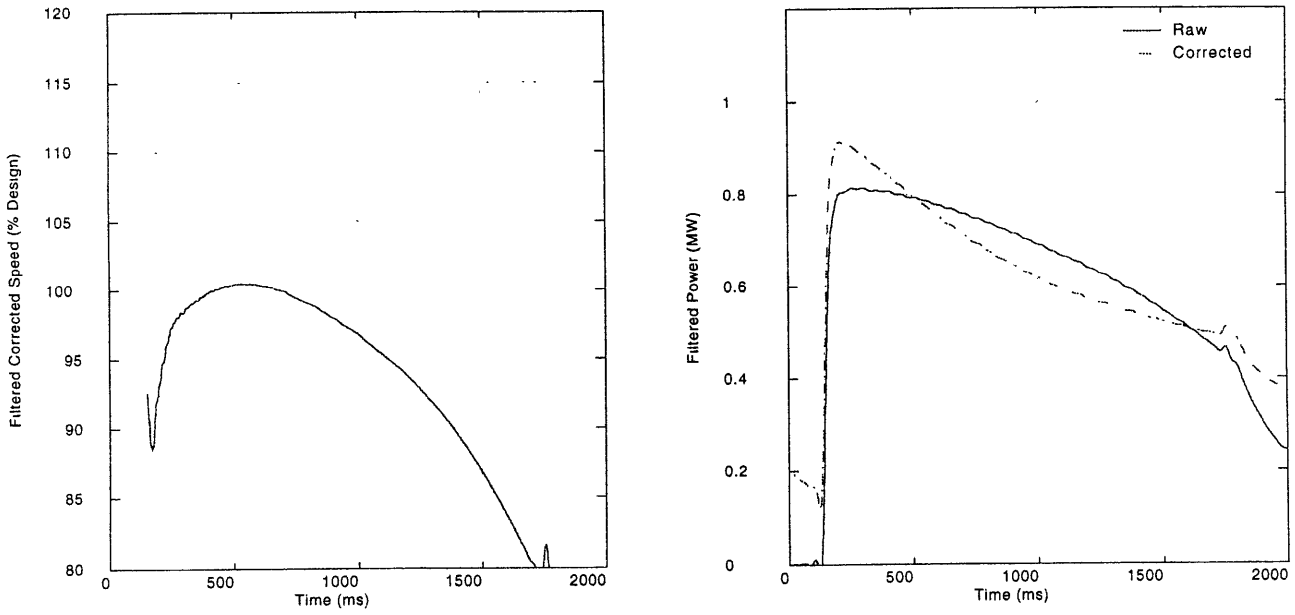

Figure A-44: Experiment 036 Corrected Speed and Power

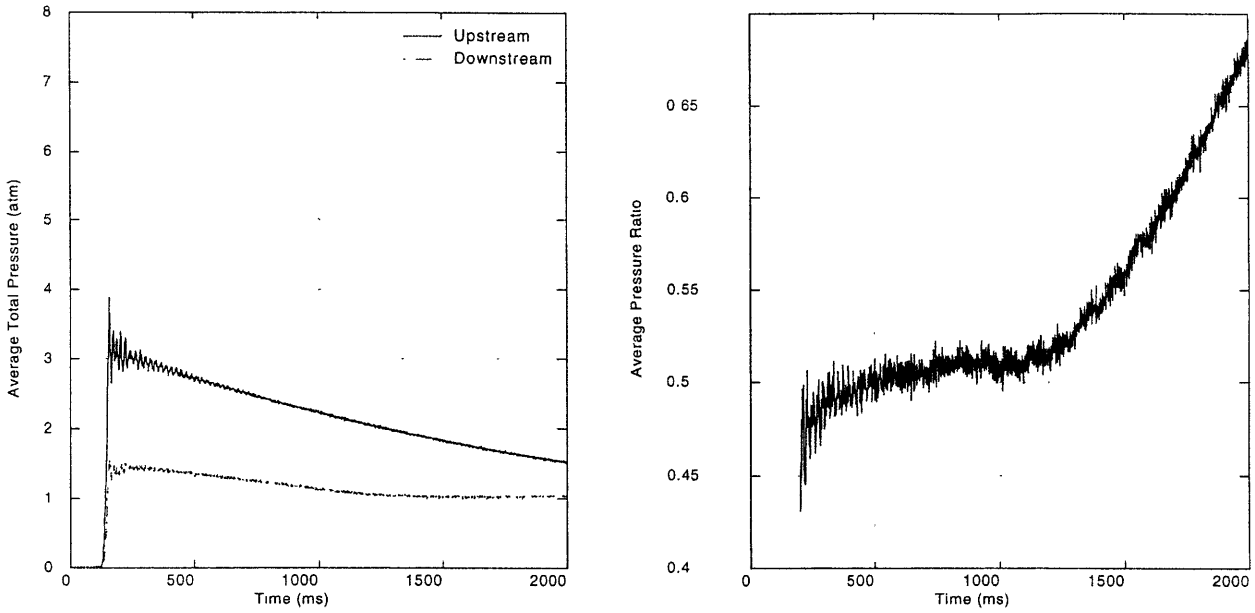

Figure A-45: Experiment 041 Average Total Pressure and Pressure Ratio

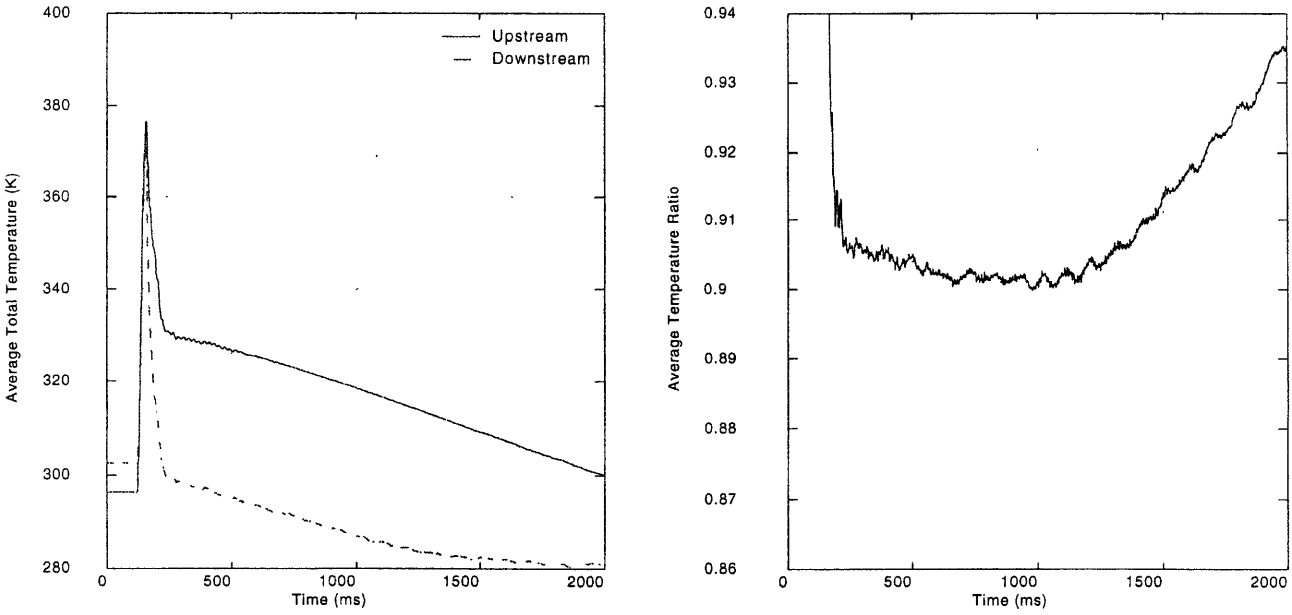

Figure A-46: Experiment 041 Average Total Temperature and Temperature Ratio

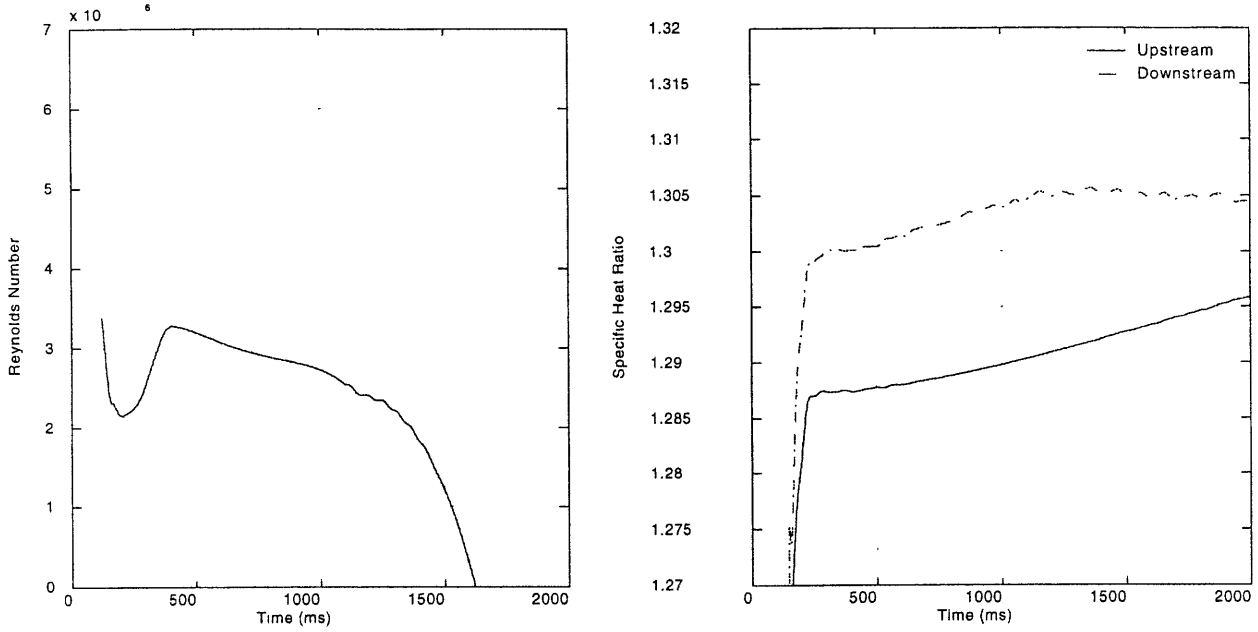

Figure A-47: Experiment 041 Reynolds Number and Specific Heat Ratio

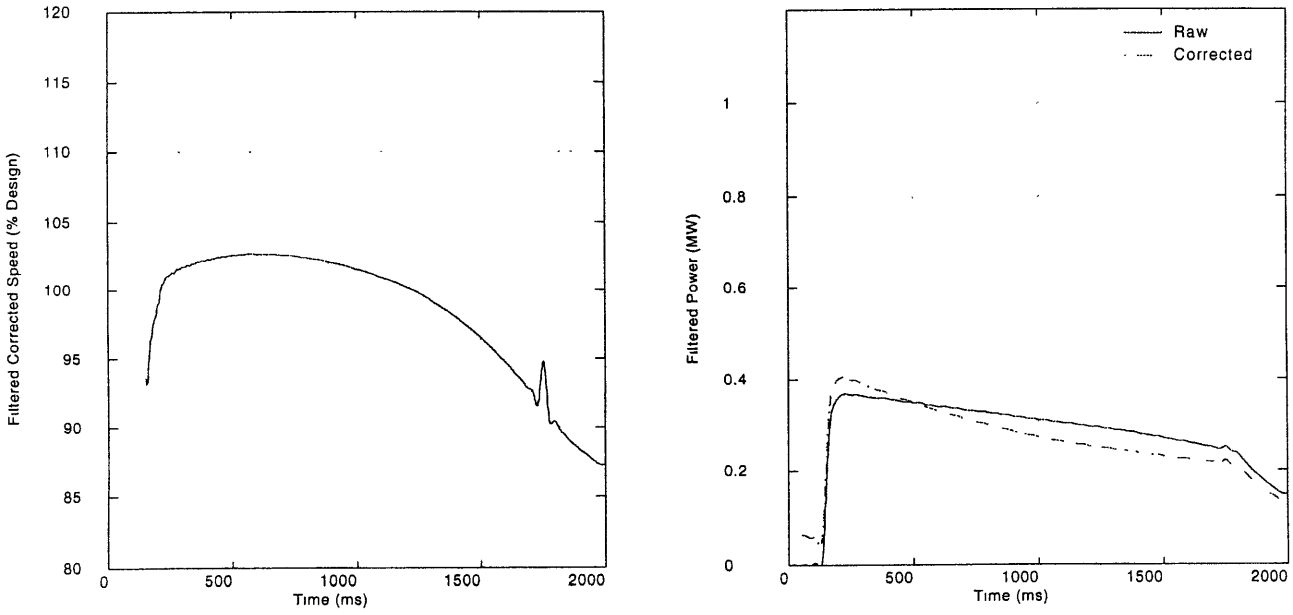

Figure A-48: Experiment 041 Corrected Speed and Power

Appendix B

Efficiency Calculations

B.1 Introduction

This appendix contains aerodynamic and mechanical adiabatic efficiency calculations for all experiments conducted during this work as summarized in Table 3.2. These calculations are discussed in Chapters 4 and 5 and are presented on the same scale for easy comparison. This scale is referenced to the Craig and Cox empirical efficiency estimate at the smaller tip clearance, $\eta_{ad,CC,0.5\,\delta}$, discussed in Section 6.3.2. All efficiency calculations have been corrected for heat transfer as described in Sections 4.5 and 5.4.

B.2 Figures

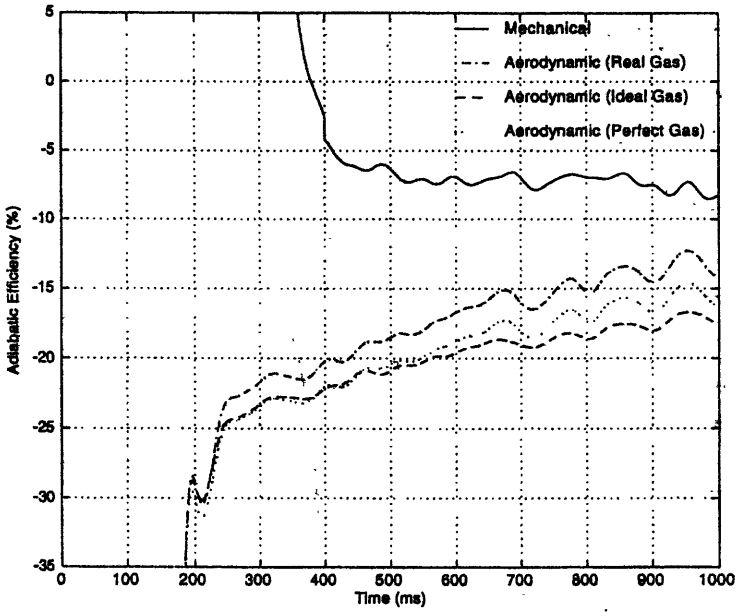

Figure B-1: Experiment 024 Aerodynamic and Mechanical Adiabatic Efficiencies

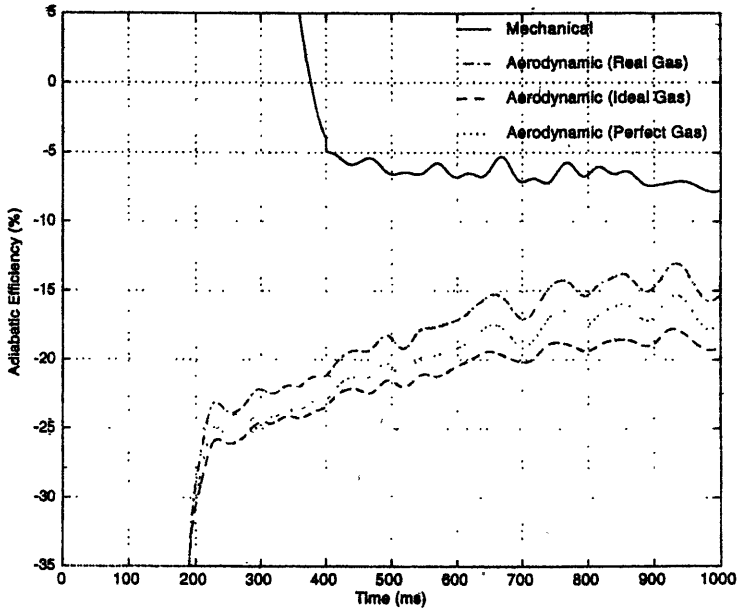

Figure B-2: Experiment 027 Aerodynamic and Mechanical Adiabatic Efficiencies

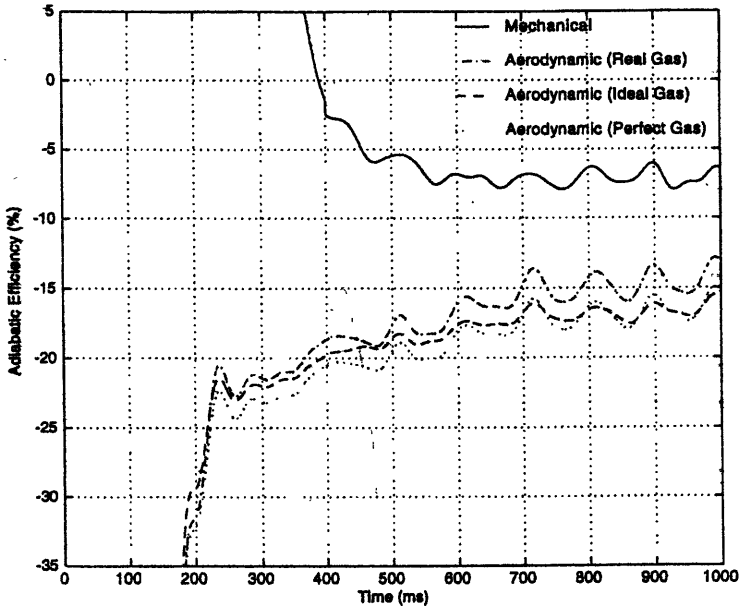

Figure B-3: Experiment 032 Aerodynamic and Mechanical Adiabatic Efficiencies

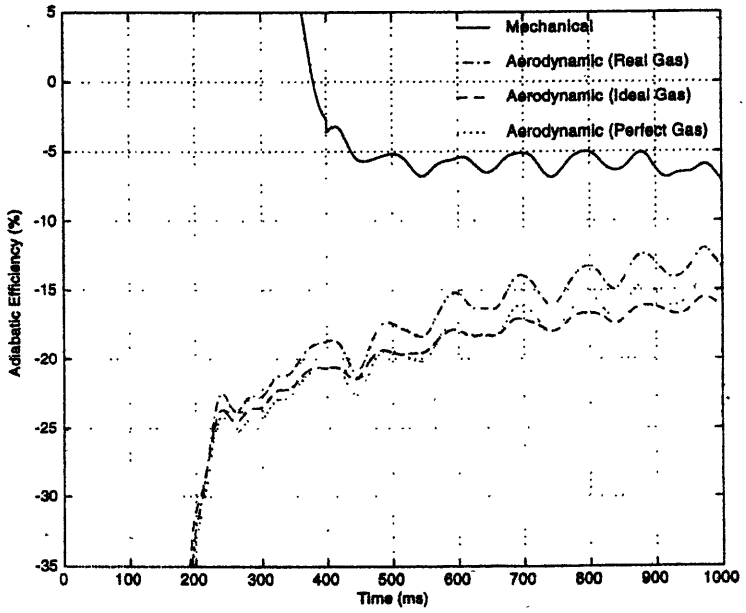

Figure B-4: Experiment 029 Aerodynamic and Mechanical Adiabatic Efficiencies

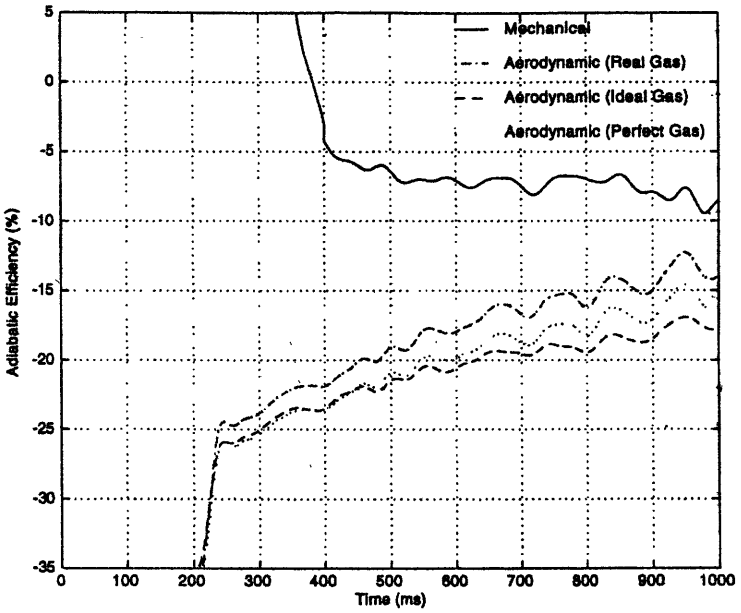

Figure B-5: Experiment 028 Aerodynamic and Mechanical Adiabatic Efficiencies

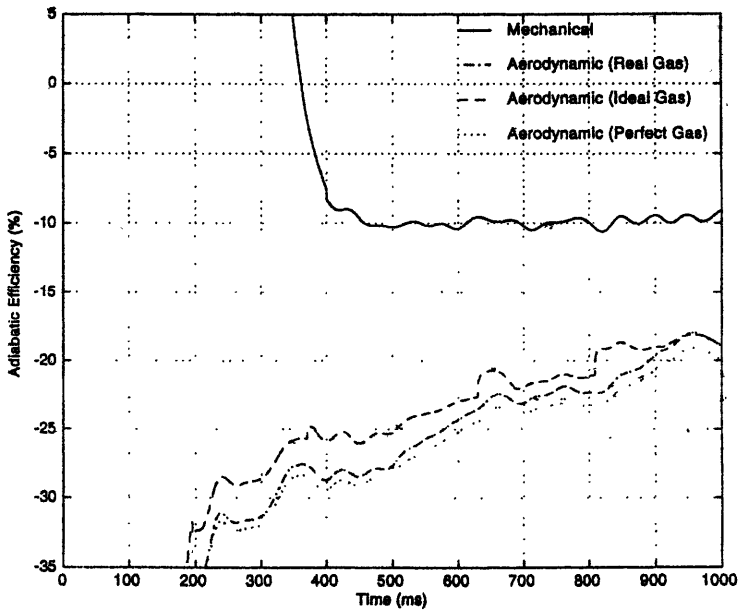

Figure B-6: Experiment 021 Aerodynamic and Mechanical Adiabatic Efficiencies

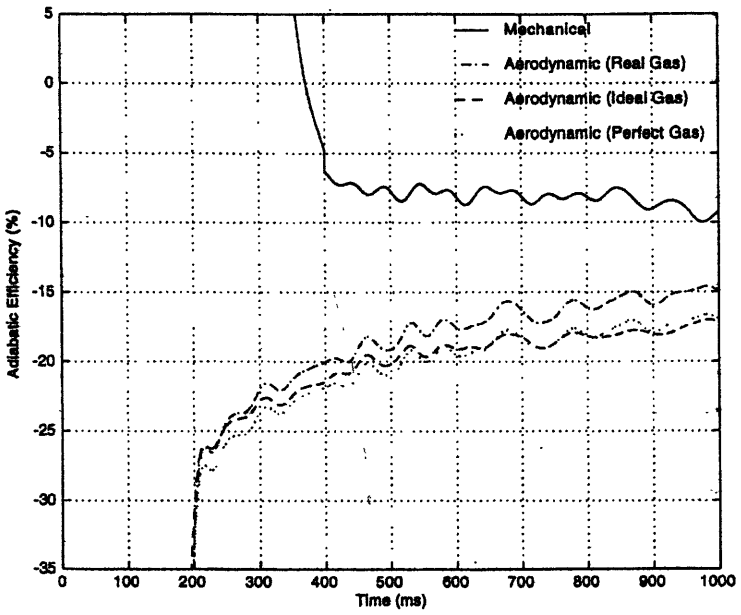

Figure B-7: Experiment 034 Aerodynamic and Mechanical Adiabatic Efficiencies

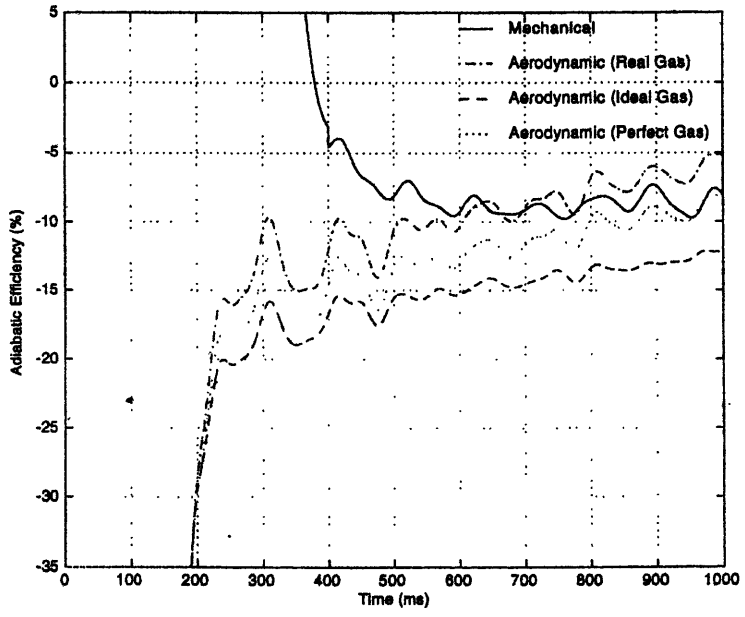

Figure B-8: Experiment 035 Aerodynamic and Mechanical Adiabatic Efficiencies

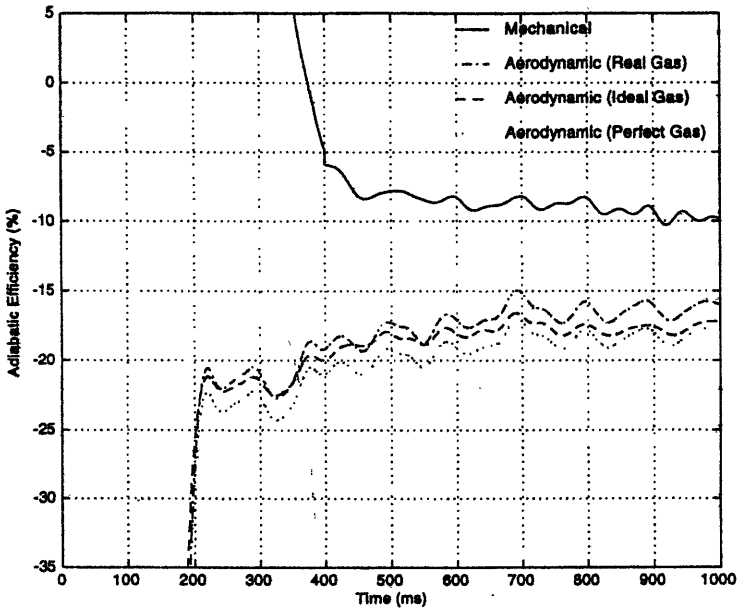

Figure B-9: Experiment 033 Aerodynamic and Mechanical Adiabatic Efficiencies

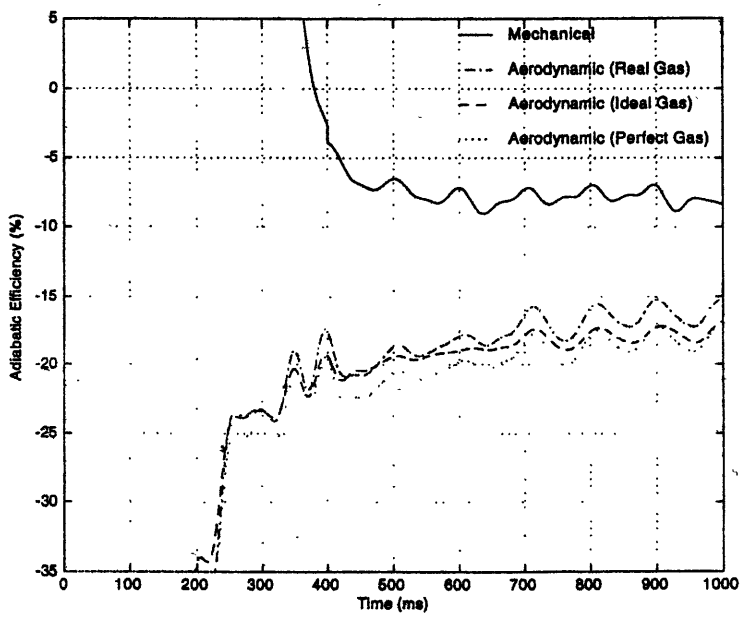

Figure B-10: Experiment 037 Aerodynamic and Mechanical Adiabatic Efficiencies

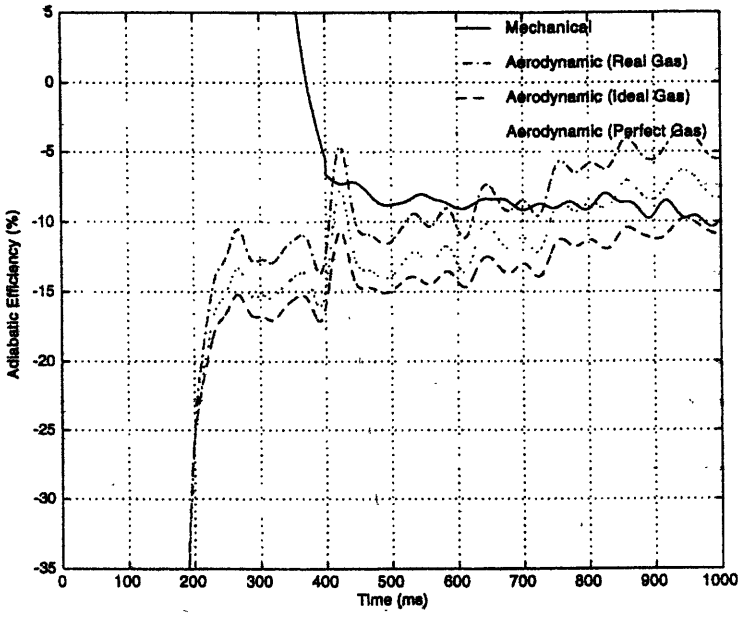

Figure B-11: Experiment 036 Aerodynamic and Mechanical Adiabatic Efficiencies

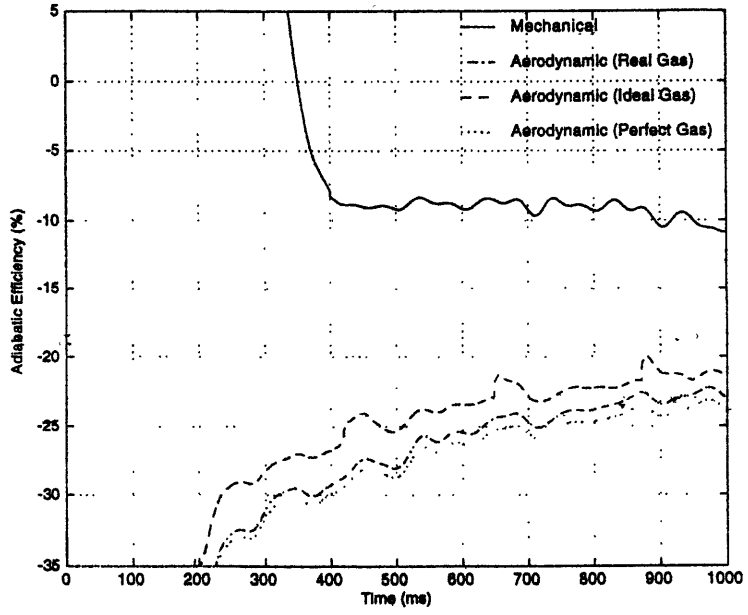

Figure B-12: Experiment 041 Aerodynamic and Mechanical Adiabatic Efficiencies

Appendix C

Description of TURBine ANalysis Computer Code

C.1 Introduction

This appendix contains information on *TURBAN*, a government owned computer code developed by the Propulsion Systems Analysis Office (PSAO) at the NASA Lewis Research Center. The text in the next section is taken from NASA-CR-198433 written by Arthur J. Glassman and can be found at http://www-psao.lerc.nasa.gov/turbo.html [16]. Additional information on *TURBAN* may be found in NASA-CR-195405, also written by Glassman [17].

C.2 *TURBine ANalysis*

"*TURBAN* is a meanline design code based on simplifying assumptions that limit the generality of the analysis but result in a very rapid calculation that needs a minimum of input. This is not the typical blade row by blade row bookkeeping of mass and energy. The stage velocity diagrams are either all similar (thereby having the same work factor) or are determined from an input stage work split. All stages have the same stator-exit

angle. Stage by stage tailoring of the velocity diagrams is not allowed. Only inlet and exit diameters are specified, and the stage mean diameters vary linearly. The loss model is a simple viscous type related to the velocity diagrams. A simple blading model provides solidities and stagger angles. Turbine coolant flows and temperatures can be specified.

TURBAN input includes flow rate, rotative speed, and power or pressure ratio. Options are provided for varying number of stages; diameter (mean or hub or tip); stator-exit angle or exit radius ratio; and reaction, loading, diagram type, and/or work split. The output presents annulus dimensions, diagram velocities and angles, blading geometries, and efficiencies" [16].

C.3 Use of *TURBine ANalysis*

For the analysis presented in Section 6.3.3, *TURBAN* was given turbine power, radial mean annulus diameters and blade dimensions and angles, and stage reaction. Predicted temperature, pressure, and Mach number distributions through the turbine stage were compared to experimental data and agreement was very reasonable. A *sample* output file, unrelated to the turbine stage considered in this work, is shown in Figure C-1.

TURBINE VELOCITY DIAGRAM ANALYSIS

0 NASA FIRST STAGE OF HIGH WORK CORE TURBINE - TM83655

	SHAFT POWER	MASS FLOW	INLET TEMP	INLET PRESS	ROT SPEED	INLET MN DIA	EXIT MN DIA	EXIT RADIUS RATIO	STATOR EX ANG	GAS CONST	HEAT CAPAC RATIO	GAS VISC	TURB LOSS COEF	AXIAL VEL SQ RATIO	T-S PRESS RATIO
0	864.0	17.22	760.0	45.0	9048.0	18.40	18.40	.0000	75.00	53 37	1.400	.16E-04	.280	1.360	.000

0 STAGES= 1 STAGE WORK FACTOR= 1.68 REYNOLDS NO.= .1449E+07 DIAGRAMS ARE INPT VU1/DVU = .8147

EXIT TIP DIAMETER = 20.11	EXIT TOT AL TEMP = 612.27	STATOR EXIT ANGLE= 75 00	FIRST STAGE MEAN SPEED = 726.42
EXIT HUB DIAMETER = 16 69	EXIT STATIC TEMP = 599.94	STAGE EXIT ANGLE =-40.32	LAST STAGE MEAN SPEED = 726.42
EXIT RADIUS RATIO = .8295	EXIT TOTAL PRESS = 19.20	ROTOR INLET ANGLE= 45.26	LAST STAGE INLET SWIRL= 995.64
INLET TIP DIAMETER= 20.11	EXIT STATIC PRESS = 17.88	ROTOR EXIT ANGLE =-74.36	LAST STAGE EXIT SWIRL = -226.46
INLET HUB DIAMETER= 16.69	T-T PRESS RATIO = 2.344	TOTAL EFFICIENCY = .900	LAST STAGE MERID VELOC= 311.15
INLET RADIUS RATIO= .8295	T-S PRESS RATIO = 2.517	STATIC EFFICIENCY= .839	EXIT MERID MACH NUMBER= .2591
LAST STG M1 ABS = .8113	LAST STG M1 REL = .2983	LAST STG M2 REL = .8347	LAST STG M2 ABS = .3205
STAGE REACTION = .471	STG TOT EFF-UNC = .900	TOTAL EFF - UNC = .900	TOTAL EFF - ROT PRIM = .900
0HUB: LAST STG M1 ABS = .9013	LAST STG M1 REL = .4099	LAST STG M2 REL = .7877	LAST STG M2 ABS = 3040
STATOR EXIT ANGLE = 76.34	ROTOR INLET ANGLE = 58.72	ROTOR EXIT ANGLE =-73 63	STAGE EXIT ANGLE = -43.11
0TIP: LAST STG M1 ABS = .7396	LAST STG M1 REL = .2269	LAST STG M2 REL = .8608	LAST STG M2 ABS = .2806
STATOR EXIT ANGLE = 73.67	ROTOR INLET ANGLE = 23.62	ROTOR EXIT ANGLE =-75.08	STAGE EXIT ANGLE = -37.83

0 STAGE 1-1 MEANLINE SLOPE = 00 DEG BASED ON MID ASPECT-RATIO BLADING

	STATOR					ROTOR					
STAGE	AXIAL CHORD (IN.)	AXIAL SOLID	ACTUAL SOLID	STAG ANGLE	NO OF VANES	AXIAL CHORD (IN.)	AXIAL SOLID	ACTUAL SOLID	STAG ANGLE	NO OF BLADES	AN**2
1	1.168	.625	1.371	62.89	31	1.168	833	.942	-27.95	41	8113E+10

Figure C-1: *TURBine ANalysis* Sample Output File

Bibliography

[1] Shapiro A. H. *The Dynamics and Thermodynamics of Compressible Fluid Flow, Volume 1.* The Ronald Press Company, New York, New York. 1954.

[2] Guenette G. R. *A Fully Scaled Short Duration Turbine Experiment.* PhD Thesis, Massachusetts Institute of Technology. 1985.

[3] Keogh R. *Shaft Efficiency Measurements of a Fully Scaled Turbine in a Short Duration Facility.* Master's Thesis, Massachusetts Institute of Technology. 1998.

[4] Cai Y. *Aerodynamic Performance Measurements in a Fully Scaled Turbine.* Master's Thesis, Massachusetts Institute of Technology. 1998.

[5] Grépin L. M. *Aerodynamic Measurement and Analysis of the Flow in an Uncooled Turbine Stage.* Master's Thesis, Massachusetts Institute of Technology. 1998.

[6] Reynolds W. C., Perkins H. C. *Engineering Thermodynamics.* Second Edition. McGraw-Hill, Inc. 1977.

[7] ASME/ANSI MFC-2M-1983. *Measurement Uncertainty for Fluid Flow in Closed Conduits.* An American National Standard, The American Society of Mechanical Engineers. 1988.

[8] Friend D. G. *Private Correspondence About NIST 14.* Fluid Mixtures Data Center, NIST Thermophysics Division 838.02, Boulder, Colorado. Summer 1997.

[9] Moran M. J., Shapiro H. N. *Fundamentals of Engineering Thermodynamics.* Second Edition. John Wiley and Sons, Inc. 1992.

[10] NIST 14. *NIST Mixture Property Database.* Standard Reference Database 14, Version 9.08. Fluid Mixtures Data Center, NIST Thermophysics Division 838.02, Boulder, Colorado. 1992.

[11] Shang T. *Influence of Inlet Temperature Distortion on Turbine Heat Transfer.* PhD Thesis, Massachusetts Institute of Technology. 1995.

[12] Epstein A. H., Guenette G. R., Ito E. *Turbine Aerodynamic Performance Measurements in Short Duration Facilities.* AIAA/ASME/SAE/ASEE 25th Joint Propulsion Conference, AIAA-89-2690. 1989.

[13] Wilson D. G. *The Design of High-Efficiency Turbomachinery and Gas Turbines.* The MIT Press, Cambridge, Massachusetts. 1984.

[14] Craig H. R. M., Cox H. J. A. *Performance Estimation of Axial Flow Turbines.* Institution of Mechanical Engineers, Proceedings, Vol. 185, pp. 407-424. 1971.

[15] Denton J. D. *Loss Mechanisms in Turbomachines.* ASME Journal of Turbomachinery, Vol. 115, pp. 621-656. 1993.

[16] Glassman A. J. *PSAO Turbomachinery Analysis, TURBine ANalysis.* NASA-CR-198433, NASA Lewis Research Center PSAO Turbomachinery Home Page, http://www-psao.lerc.nasa.gov/turbo.html.

[17] Glassman A. J. *Enhanced Capabilities and Updated Users Manual for Axial-Flow Turbine Preliminary Sizing Code TURBAN.* NASA-CR-195405. 1994.